Fracture and Impact Dynamics of Beam Lattices

Finite Element Modeling with Penalty Contact for Energy Dissipation in Architected Materials

Alberts Osis

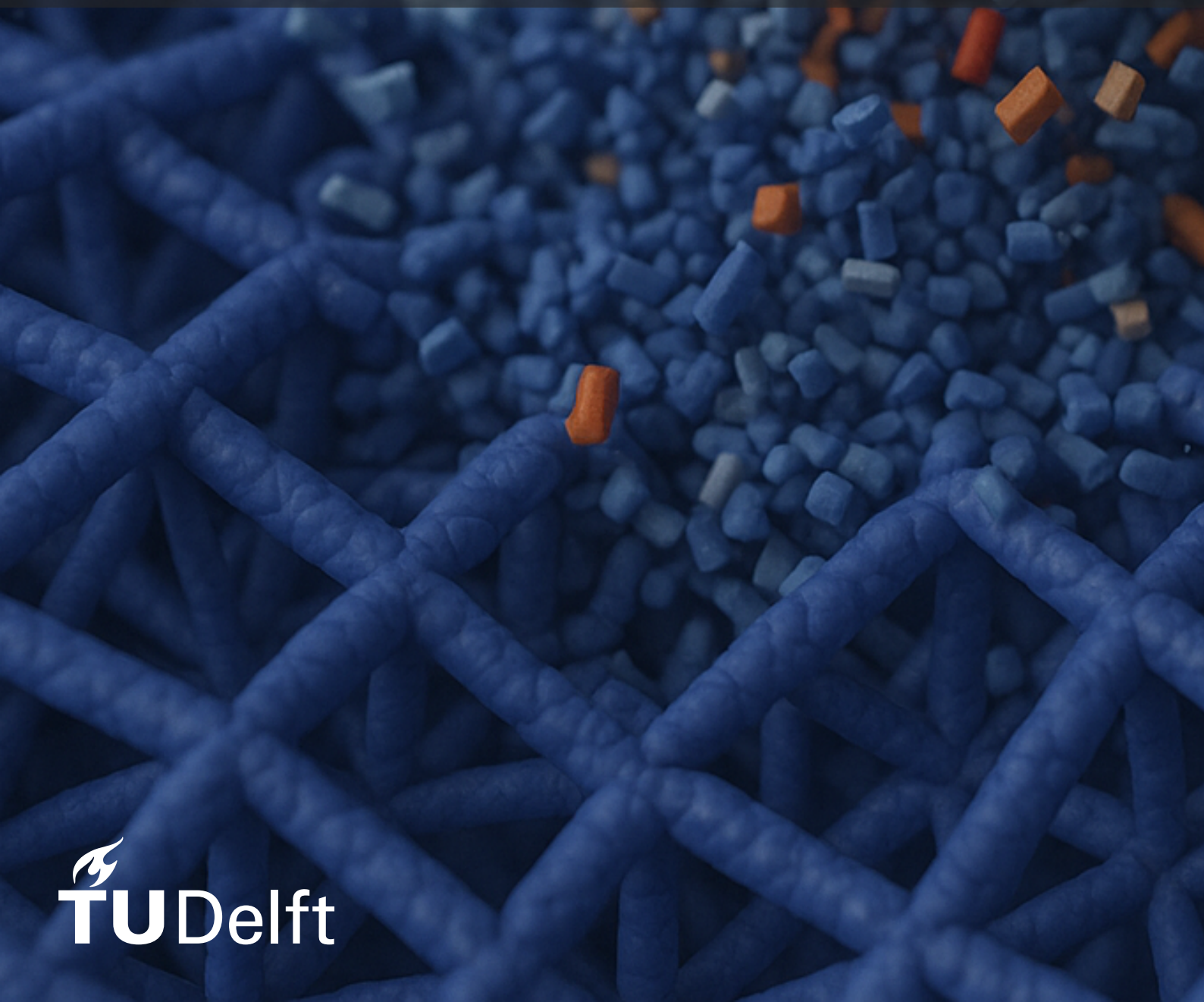

TU Delft

Fracture and Impact Dynamics of Beam Lattices

Finite Element Modeling with Penalty Contact for Energy Dissipation in Architected Materials

by

Alberts Osis

to obtain the degree of Master of Science
at the Delft University of Technology,
to be defended publicly on Friday June 13, 2025 at 14:00.

Student number:	5057531	
Project duration:	May 2024 – June 2025	
Thesis committee:	Dr. B. Giovanardi,	TU Delft, supervisor
	Dr. B. Chen,	TU Delft, chair
	Dr. P. Sundaramoorthy,	TU Delft, examiner

Cover:	AI generated image by OpenAI. (2025). Abstract close-up of a deformed metamaterial lattice. ChatGPT. https://openai.com/chatgpt
Style:	TU Delft Report Style, with modifications by Daan Zwaneveld

An electronic version of this thesis is available at `http://repository.tudelft.nl/`.

TU Delft

Executive Summary

Architected beam lattices—ultra-light truss networks fabricated by additive manufacturing—have emerged as a promising material class for protecting different structures against impact, including defending spacecraft against micro-meteoroid and orbital debris (MMOD) impacts. Their high specific strength, energy absorption and tunable mechanical properties make them ideal candidates for shielding applications. However, the complex fracture and impact dynamics of these lattices remain not fully understood, hindering their rational design and deployment in space missions.

This thesis develops and applies a discontinuous-Galerkin (DG) finite-element framework capable of predicting large-deformation contact and fracture in high-fidelity lattice structures struck by rigid projectiles at up to $350\,\mathrm{m\,s^{-1}}$. It employs Kirchoff-Love beams to efficiently model a lattice structure as a network of slender, torsion-free struts, while a cohesive zone model captures the fracture process. The impact is modelled using a penalty contact law, which enforces interaction between the impactor and the lattice by applying a force upon contact.

Current work on lattice metamaterials has regarding their energy-absorption potentially has identified three distinct impact modes: bounce-back, which is characterized by the impactor rebounding from the lattice; capture, where the impactor becomes lodged in the lattice structure; and penetration, where the impactor breaches the lattice and continues through it. These modes are influenced by the lattice topology and relative density. It is attempted in this thesis to reproduce these impact modes computationally and to identify the governing parameters that influence the transition between them. Furthermore, focus is put on understanding the energy dissipation mechanisms in lattice metamaterials under impact conditions, particularly how the lattice structure and material properties influence the energy absorption capacity.

Consequently, a research question was proposed: How can a high-fidelity computational model identify and reproduce the main physical processes involved in a metamaterial impact?

To answer the question 4 different lattice types were examined that were subjected to rigid impactors at velocities ranging from $50\,\mathrm{m\,s^{-1}}$ to $350\,\mathrm{m\,s^{-1}}$. The simulations were designed to capture the complex interplay of elastic and non-elastic collision behaviors, penetration, bounce-back, and particle capture. The results were compiled to illustrate the energy dissipation mechanisms of the lattice by examining the behavior of the impactor during impact.

In order to sufficiently model the impact of a lattice metamaterial a high-fidelity lattice had to be used. For this work meshes containing up to 72 thousand nodes were used with time step of $1.0e-9$ seconds, which allowed for a detailed representation of the lattice structure and its response to impact. The simulations were run on distributed computing hardware, enabling efficient scaling and handling of large-scale lattice structures.

As a result it was found that the computational model successfully reproduced key impact phenomena observed experimentally, including elastic and non-elastic collision behaviors, penetration, bounce-back, and particle capture, across various impact velocities. The results were partially consistent with findings from Portela [1] and Butruille [2]. The effect of the radius of the lattice struts and impact velocity on the impact mode were successfully reproduced. A key difference from experimental results found in literature being the lack of linear scaling of energy absorption with increasing impact velocities. Using these results and analyzing what results align with the literature, it was possible to draw conclusions about the energy dissipation mechanisms in lattice metamaterials and what are the key physical phenomena that need to be modelled and what are the drawbacks of the current model.

Contents

Executive Summary **i**

1 Introduction **1**
1.1 Relevance of metamaterials . . . 1
1.2 Research approach . . . 3
1.3 Modelling truss based lattice architected materials . . . 3

2 Literature Review **5**
2.1 Impact experiments of lattice based nanoarchitected materials . . . 5
2.1.1 Experimental setups for impact of nanoarchitected beam materials . . . 5
2.1.2 Dimensional analysis of nanoarchitected material impact . . . 8
2.1.3 Analysis of metamaterial impact experiments . . . 9
2.1.4 Effect of strain-rate . . . 11
2.1.5 Conclusion . . . 11
2.2 Overview of impact physics . . . 11
2.2.1 High velocity impacts . . . 12
2.2.2 Low-fidelity models for ballistic impacts . . . 13
2.2.3 Summary of impact physics . . . 16
2.3 Computational model of the impact . . . 17
2.3.1 Kirchoff-Love beam . . . 17
2.3.2 Fracture mechanics . . . 17
2.3.3 Galerkin methods . . . 18
2.3.4 Time solver . . . 19
2.4 Contact formulation . . . 20
2.4.1 General contact formulation . . . 20
2.4.2 Lagrange multiplier methods . . . 23
2.4.3 Penalty methods . . . 24
2.5 Conclusion . . . 25
2.5.1 Research gaps . . . 25

3 Methodology **27**
3.1 Overview . . . 27
3.2 Kirchoff beam formulation . . . 27
3.3 Cohesive zone method . . . 30
3.4 Computational framework for fracture in geometrically exact slender beams . . . 32
3.5 Discretization in space and time . . . 35
3.6 Penalty method for rigid contact with truss lattices . . . 37
3.7 Parallelization . . . 38
3.8 *Summit* framework . . . 38

4 Results and Discussions **40**
4.1 Simulation setup . . . 40
4.2 Impact of a rigid impactor into a truss based lattice . . . 41
4.2.1 Qualitative impact behavior . . . 41
4.2.2 Energy dissipation behavior . . . 44

5 Conclusion **50**
5.1 Summary of findings . . . 50
5.2 Recommendations for future work . . . 50

References **53**

A Appendix A **54**
A.1 Information about the setup of the impact simulations 54

List of Figures

1.1 Evolution of the number and type of objects in orbit over time [12] 2
1.2 Strength and stiffness to density ratio performance of various nanolattice materials [8] . 3

2.1 Comparison of mass normalized impact energy of various materials as function of impact velocity [1]. 6
2.2 Rebound impact mode shown in row **a**, Capture impact mode shown in row **b** and post impact micrograph images of the nanoarchitected carbon lattices used for analysis of experiments shown in **c**. [1] 6
2.3 The experimental setup used for decoupling particle impact dissipation mechanisms. Part **A** shows the manufacture of the architected plate via two-photon lithography. Part **B** shows the three types of materials used in this work: octet, monolithic and tetrakaidecahedron architecture respectively. White scale bars $100\mu m$, yellow scale bars $5\mu m$. Part **C** demonstrates the laser accelerated $30\mu m$ impactor as well as pre-impact velocity v_i and post-impact velocity v_f [2]. 8
2.4 Impact analysis involving comparing pre and post impact impactor velocities and the mass of the materials in the cylindrical crater. Parts **A** and **C** show the used properties of the lattice, impactor and impact crater. Parts **B** and **D** show the final velocity and normalized dissipated energy as functions of initial velocity. Part **E** shows the dimensionless groups Π used for dimensional analysis [2]. 9
2.5 Decoupled compaction mechanisms in microlattices. Part **A** contains energy dissipation during impact showing fracture (W_f), compaction (W_c), and inertia (W_{in}), with compaction front speed v_c and projectile velocities v_i and v_f. Parts **B** and **C** show simulated and experimental uniaxial compaction of $10 \times 10 \times 10$ octet and tetrakaidecahedron lattices. Parts **D** and **E** show corresponding stress–strain curves; solid lines show averages, dotted lines indicate standard deviations. (Scale bars: 20 μm.) [2]. 10
2.6 Parts **i** and **ii** display displacement gradients vs. radial distance in octet lattices. Part **iii** show simple shear simulations with corresponding stress–strain responses [2]. 10
2.7 Part **i** shows CAD and SEM of pillar-induced indentation into octet and tetrakaidecahedron lattices. (Scale bar: 10 μm.) Parts **ii** and **iii** display stress vs. normalized displacement for varying pillar diameters [2]. 11
2.8 Distributions of publications about impact for various velocities as compiled by [17]. . . 12
2.9 Various feature of a debris cloud of an aluminium sphere impacting a thin aluminium plate [18]. 13
2.10 Four distinct phases of the Awerbuch-Bodner model[20]. 15
2.11 Key variables of hydrodynamic penetration model [20]. 16
2.12 Unilateral contact of an elastic solid [29] 20
2.13 Solutions of a simple system governed by a variationaly inequality [29] 23
2.14 Spring system where ε is the contact penalty factor [29] 24

3.1 The impact simulation setup depicting the rigid impactor colliding with the beam lattice structure. 28
3.2 Kinematics of a geometrically exact Kirchhoff beam with circular cross-section. The beam configuration is characterized by the line of centroids $\boldsymbol{r}(s)$ and by the orthonormal *intrinsic* frame $\{\boldsymbol{g_1}(s), \boldsymbol{g_2}(s), \boldsymbol{g_3}(s)\}$. The Kirchhoff constraint enforces that $\boldsymbol{g_1}(s)$ be tangent to the line of centroids, or that $\boldsymbol{g_1}(s) = \frac{\boldsymbol{r}'(s)}{||\boldsymbol{r}'(s)||}$ [35]. 29
3.3 The fracture modes of beams: (a) tension, (b) shear, (c) torsion and (d) bending [35]. . . 31

3.4 The force-separation cohesive law defines a linear reduction of the scalar effective cohesive force f_{coh} with the scalar effective separation Δ, decreasing from a critical value f_c to zero. Irreversibility is incorporated by introducing a history variable Δ_{max}, which tracks the maximum effective separation reached. During unloading, the response follows a path back to the origin, while reloading proceeds along the same unloading trajectory. The total area under the force-separation curve corresponds to the effective fracture energy of the material, whereas the black and grey regions at any given $\Delta = \Delta_{max}$ represent the dissipated and maximum recoverable energies at the cohesive boundary. Complete fracture occurs when $\Delta \geq \Delta_c$ [35]. 32
3.5 The discontinuous Galerkin discretization of the straight, undeformed beam with duplicated internal nodes enabling discontinuities at the element interfaces s_n for $n = 1, ..., E-1$ thus allowing fractures to be formed on the interfaces [35]. 33
3.6 Implementation of the penalty contact method on a simple lattice. 37
3.7 The division of the truss lattice into subdomains for parallelization. 38
3.8 Overview of the *Summit* framework withing in the context of this work. 39

4.1 Visualized example of an impactor during an impact with octet lattice. The color of the lattice indicates the deformation of the lattice with red being the most deformed and blue being the least deformed. 41
4.2 Starting setup for all of the Lattice types with the impactor right before contact with the lattice. 41
4.3 Visualized example of penetrating behavior. The figure shows a bitruncated octahedron lattice and impactor after 300 m/s impact. The lattice is heavily deformed and debris has been dispersed in the surrounding environment. The color of the lattice indicates the deformation of the lattice with red being the most deformed and blue being the least deformed. 41
4.4 Visualized example of bounce-back behavior. The figure shows an octet lattice and impactor after 150 m/s impact. The lattice has localized damage and some debris has been dispersed in the surrounding environment. The color of the lattice indicates the deformation of the lattice with red being the most deformed and blue being the least deformed. 42
4.5 Visualized example of capture behavior. The figure shows an octet lattice and impactor after 100 m/s impact. The lattice has localized damage and some debris has been dispersed in the surrounding environment. The impactor velocity is almost zero and thus it can be considered captured by the lattice. The color of the lattice indicates the deformation of the lattice with red being the most deformed and blue being the least deformed. 42
4.6 Kinematic behavior of the impactor as functions of time at 7 different initial velocities for Lattice type 1. Plot **A** includes impactor position along z axis which is the axis of impact. The position for all velocities starts at non-zero value since the position of the impactor at the start offset by the radius of the impactor such that the impactor is in contact with the outer surface of the lattice. The plots illustrate the fact that depending on the impact velocity the impactor can exhibit different behavior - bounce back for the 3 slower impactors (which is seen as the the plots having positive slope), substantial slow down for the $200 m/s$ impactor and penetration for the remaining faster impactors. The velocity plots (plot **B**) show the value of velocity of the impactor along impact axis. The plot also demonstrates that the lower impact velocity impactors exhibit a bounce-back behavior that is illustrated as the velocity becoming negative. 42
4.7 Kinematic behavior of the impactor as functions of time at 7 different initial velocities for Lattice type 2. Plot **A** includes impactor position along z axis which is the axis of impact. Plot **B** shows the velocity of the impactor along z axis. The position for all velocities starts at non-zero value since the position of the impactor at the start offset by the radius of the impactor such that the impactor is in contact with the outer surface of the lattice. The plots illustrate the fact that depending on the impact velocity the impactor can exhibit different behavior - impactor capture behavior for the two slowest impactors, penetration for the faster impactors however no bounce-back behavior is observed. Capture is shown as the position plot **A** being horizontal and the velocity plot **B** reaching zero. 43

4.8 Kinematic behavior of the impactor as functions of time at 7 different initial velocities for Lattice type 3. Plot **A** includes impactor position along z axis which is the axis of impact. Plot **B** shows the velocity of the impactor along z axis. The position for all velocities starts at non-zero value since the position of the impactor at the start offset by the radius of the impactor such that the impactor is in contact with the outer surface of the lattice. This figure shows bounce-back of the impactor from the lattice which is seen as a minimum point in plot **A** and as negative values in plot **B**. No other impact modes could be identified for this setup, likely due to the increased thickness of the lattice. . . 43
4.9 Kinematic behavior of the impactor as functions of time at 7 different initial velocities for Lattice type 3. Plot **A** includes impactor position along z axis which is the axis of impact. Plot **B** shows the velocity of the impactor along z axis. The position for all velocities starts at non-zero value since the position of the impactor at the start offset by the radius of the impactor such that the impactor is in contact with the outer surface of the lattice. The plots illustrate the fact that depending on the impact velocity the impactor can exhibit different behavior - impactor capture behavior for the slowest impactor, penetration for the faster impactors however no bounce-back behavior is observed. Capture is shown as the position plot **A** being horizontal and the velocity plot **B** reaching zero. 44
4.10 Energy of the impactor as a function of time at 7 different initial velocities for Lattice type 1. The plots illustrate the bounce-back behavior of the lattice at lower impact velocities as an increase in the energy value of the impactor after a dip in energy values. For higher velocities impactor regains no energy as the impact shows either penetration or capture. 45
4.11 Energy of the impactor as a function of time at 7 different initial velocities for Lattice type 2. All of the impactor energy curves show a similar pattern of energy loss as the impactor penetrates the lattice. Furthermore, the 2 slowest impactors show a capture behavior of the impactor as the energy of the impactor as can be seen on the plots approaches zero. 45
4.12 Energy of the impactor as a function of time at 7 different initial velocities for Lattice type 3. For this Lattice type all of the impacts show bounce-back behavior and the magnitude of energy loss is illustrated in this plot as the difference between starting energy and the energy at the end of the impact. 46
4.13 Energy of the impactor as a function of time at 7 different initial velocities for Lattice type 4. All of the impactor energy curves show a similar pattern of energy loss as the impactor penetrates the lattice. 46
4.14 Comparison of final velocities of the impactor at 7 different velocities for the 4 lattice types. The plot shows the final velocity of the impactor as a function of initial velocity. A diagonal line shows perfectly elastic behavior with the final velocity being equal to the initial velocity and dashed line shows conditions when initial velocity is equal to final velocity. The four Lattice types show distinct behavior. At lower velocities the plots show show any trends less clearly for all of the Lattice types. As the velocities increase all of the plots show more linear trends with Lattice types 1, 2 and 4 approaching the dashed line for higher impact velocities. This effect can be described by the fact that the energy of the impactor increases with higher velocity at a much greater rate than the ability of the lattice to dissipate the energy. Lattice type 3 roughly follows the full diagonal line that describes elastic impact for lower velocities but for higher velocities the impactor bounces back at roughly the same velocity. Furthermore, it can be seen in the plot that Lattice type 2 is closer to the dashed line than Lattice types 1 and 3 thus indicating lower ability to absorb energy of Lattice type 2. 47
4.15 Comparison of energy loss of the impactor at 7 different velocities for various Lattice types. Plot **A** shows the energy loss of the impactor as a function of initial velocity. It can be seen that with increasing initial velocity the amount of energy loss is increased. Plot **B** shows the energy loss relative to initial energy as a function of initial velocity. This plot illustrates that there exists an energy loss maximum at medium velocities. Plot **C** shows the energy loss in Joules normalized by the relative densities of each of the lattices. . . . 48

List of Tables

4.1 Lattice properties of the 4 Lattice types used in the simulation. The two properties that were changed were the Lattice type and strut radius. Additionally, relative density is calculated and provided in the table. 40

A.1 Parameters describing the setup of the impact simulations. Contact penalty parameter was 10 for lattice types 1, 2 and 4 but it was increased to 100 for lattice type 3 due to its substantial higher stiffness. 54

1
Introduction

1.1. Relevance of metamaterials

Material science plays a pivotal role in engineering, as it provides the foundations for the design and optimization of ever-evolving demands of modern applications. By understanding the relationship between material's structure, properties, processing methods, and performance, engineers can develop innovative solutions to complex challenges across diverse industries. One of the most exciting developments in material science in recent years is the emergence of metamaterials. Metamaterials in the most general sense are synthetic materials with desired optical, electrical, acoustic or mechanical properties that are rarely observable in natural materials. They may be used for optical devices due to their refractive properties [3], electrical shielding by the virtue of their unique geometry [4] or mechanical applications [1, 5–7].

With the emergence of new and improved manufacturing technologies it is possible to arrange the structure of materials in ways that were not possible before - architected cellular materials. These materials consist of a truss lattice structure potentially made at any scales ranging from meter to nanometer per cell [1, 2]. The microstructure of the materials enable mechanical properties that could show potential in the aerospace industry . In fact, these metamaterials can be designed for high specific strength, high stiffness [8] or some exotic properties such as auxetic behaviour (negative Poisson ratio) [6].

One of the key drivers of material properties in the macro scale is the condition of the material in nanoscale. This has motivated the development of architected cellular materials which have a cellular structure in the nanoscale. These materials are called called nanoarchitected materials or (nano)lattice metamaterials. Enabled by development in manufacturing technologies such as IP-Dip photoresist or lithography based technologies that allow to create metal features at the nanometer scale [9], research of potential properties and applications is actively being performed. Materials have been developed that high stiffness-to-weight ratio, strength-to-weight ratio and extreme resilience [1, 2, 7].

Truss based cellular metamaterials in aerospace

Innovation in material manufacturing technologies has been a key driver of human progress throughout history. One of the key recent developments have been widespread development of various additive manufacturing technologies, which have enabled the production of complex geometries that were previously impossible to manufacture [8–11]. This applies to a wide range of geometries in various scales, from microscale to macroscale. An exciting type of material that is consequently proliferated is the so-called metamaterials or nano-architected materials. These materials through their unique microscopic geometries can exhibit increased mechanical properties such as specific stiffness and strength and even exotic properties that are not found in nature, such as negative Poisson's ratio, negative thermal expansion, or negative stiffness. This allows for the materials to be used in a wide range of applications, from aerospace to medical devices. In this research project, the focus will be on a type of metamaterials that consists of architected truss based cellular materials and their application as impact absorbing materials in aerospace.

A key challenge that needs to be addressed in the aerospace domain is the increased ever-presence of space debris. Micrometeroids and orbital debris or Micrometeroids and orbital debris (MMOD) created as a result of human activity in Space pose a risk to human life in space and has the potential to disrupt critical services on Earth. There are currently over 130 million pieces of debris smaller than 1 cm, 1.1 million pieces between 1-10 cm, and 40.5 thousand pieces larger than 10 cm in orbit around Earth [12]. Not only it is a great number of objects flying in the orbit a speeds of multiple kilometers per second, but the number of objects is also increasing Figure 1.1. This poses a significant risk to the safety of astronauts and the integrity of spacecraft.

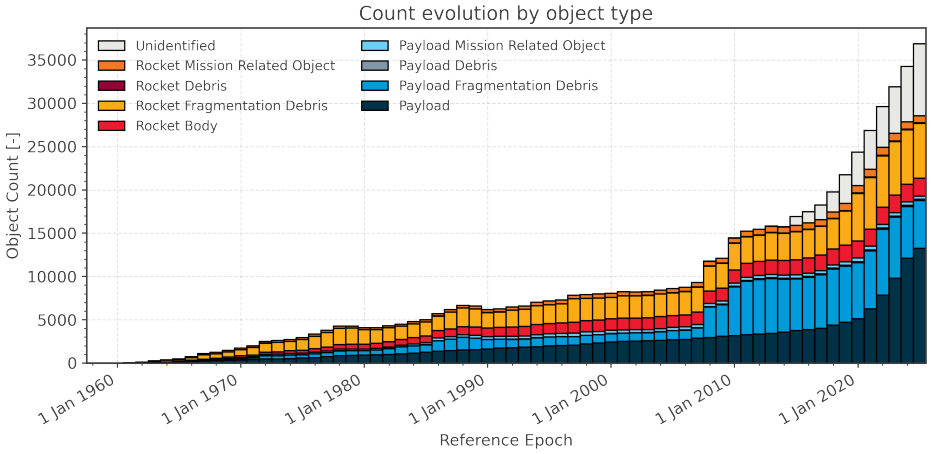

Figure 1.1: Evolution of the number and type of objects in orbit over time [12]

One of the ways the danger posed by MMOD can be mitigated is by designing spacecraft that are more resilient to impacts. This can be achieved by designing spacecraft that are able to absorb the energy of the impact and prevent the debris from penetrating the spacecraft [13].

Truss based cellular metamaterials are able to absorb a large amount of energy at low weight making them ideal for use in spacecraft [2, 7]. This is enabled by combining various physical phenomena. Firstly, the microscale geometry of the material allows enables the size effect to come into play, which increases the strength of the material [14, 15]. Secondly, the truss based cellular structure allows for the material to maintain low density without the added disadvantages of other lightweight materials such as stochastic foams [7, 16]. Thirdly, the low density enables a new domain in the Ashby material plot (Figure 1.2) meaning new designs can be created that can absorb increased amount of energy before failing when compared to other materials [7]. These factors enable material properties that have the potential to have great impact resistance for their weight.

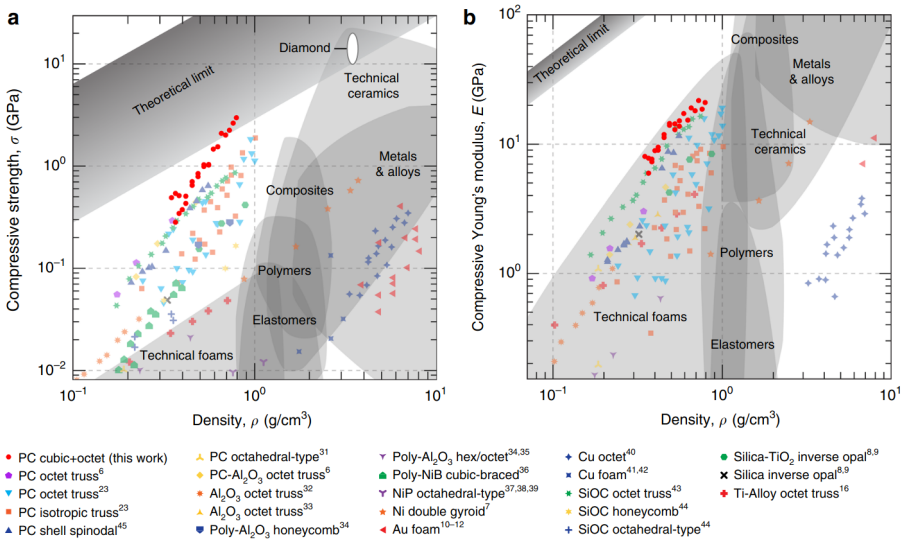

Figure 1.2: Strength and stiffness to density ratio performance of various nanolattice materials [8]

1.2. Research approach

Currently, there has been both experimental and computational analysis of impact of truss based metamaterials. Key efforts are being made to develop tools and methods that would allow to understand the underlying physical processes involved in the impact. The research attempts to gain insight into how the material behaves during and after the impact by performing work that decouples both the material properties from each other, as well as the various physical processes. This would allow to make connections between and gauge the importance of each of the variables involved in designing metamaterials and understanding the impact process itself.

This thesis sets out to evaluate the current state of the art in computational modelling of truss based metamaterials and to identify the key challenges and shortcomings of modelling the impact process with a relatively simple and yet high fidelity model. The research question is thus formulated as follows:

Research question

How can a high-fidelity computational model identify and reproduce the main physical processes involved in a metamaterial impact?

This research question is broken down into the following sub-questions:

- Can the truss lattice beam computational model be used to reproduce key trends and processes observed in experimental work, such as: elastic/non-elastic impact and dependance of energy absorption on impactor velocity, mesh density, mesh type and other parameters?
- What are the shortcomings of the computational model caused by the simplifications of the computational model, such as lack of plasticity, omission of strain rate effects and use of beam elements for the model?

1.3. Modelling truss based lattice architected materials

This thesis employs a robust computational methodology designed to explore and elucidate the primary physical processes governing the impact response and energy dissipation mechanisms in lattice-based metamaterials. The core modeling framework integrates several advanced computational techniques to accurately simulate dynamic interactions, large deformations, and fracture processes occurring during high-velocity impacts with the ultimate aim to replicating experimental work as shown by Portela and Butruille [1, 2].

The structural response of the lattice metamaterials is captured using geometrically exact Kirchhoff-Love beam elements, ideal for modeling slender beam structures prevalent in truss lattices. This beam theory assumes negligible shear deformation, significantly reducing computational complexity while retaining accuracy in describing bending-dominated behaviors, essential for capturing realistic deformation patterns under impact conditions.

To effectively model fracture processes, this work utilizes a Cohesive zone model (CZM) formulated through stress resultant cohesive laws, which differ from traditional traction-separation formulations. This approach allows for detailed characterization of crack initiation and propagation, providing insights into energy dissipation mechanisms associated with fracture phenomena.

The numerical solution of the governing equations is carried out using the Discontinuous Galerkin (DG) method, renowned for its capacity to handle discontinuities and steep gradients characteristic of dynamic fracture simulations. The DG approach offers superior accuracy and flexibility, particularly beneficial when integrated with cohesive zone fracture modeling, ensuring simulation of evolving cracks and dynamic deformation patterns.

Contact interactions between the impacting bodies and the lattice structure are managed through a penalty-based contact formulation, chosen for its computational efficiency and robustness. This method facilitates the enforcement of contact constraints without significantly increasing computational demands, making it suitable for extensive parametric studies.

Finally, the results are evaluated by examining how the impactor behaves during impact by analyzing it velocity and energy. Furthermore, the effect of impactor velocity and lattice parameters, such as lattice density and type are examined. The results are compared to experimental work to answer the research question.

2

Literature Review

This chapter aims to present the current understanding of the scientific principles and context relevant to the research.

2.1. Impact experiments of lattice based nanoarchitected materials

Current understanding of lattice based architected materials shows extensive understanding of static loading and elastic-wave propagation. However, the literature on dynamic loading and impact response is limited, especially when large deformations and high rates of strain have to be considered. Some of the key advancements with regards to impact phenomena made are presented in [1] [2]. The papers focus on identifying and understanding the key effects that take place during impact of lattice based architected materials.

2.1.1. Experimental setups for impact of nanoarchitected beam materials

In a research work looking into supersonic impact resilience of nanoarchitected materials [1] a set of experiments have been performed wherein various samples of nanoarchitected carbon lattices were subjected to impact by SiO_2 projected at speeds ranging from $30m/s$ to $1.2km/s$. The experiments also varied the relative density ($\bar{\rho}$) of the lattice by changing the thickness of the beams used in the lattice. Furthermore another set of baseline calibration experiments were conducted on a thick Si substrate. Consequently there were 3 sets of impact media used: Si impact calibration substrate and 2 carbon nanolattice samples with relative densities of $\bar{\rho} \approx 14\%$ and $\bar{\rho} \approx 23\%$. The research had two main focus points. Firstly, attempting to apply planetary impact methodology on impact of nanoarchitected materials that allows to create predictive tools for crater formation using dimensional analysis. Secondly, on obtaining experimental data that can be used for evaluating impact properties of lattice based nanoarchitected materials by comparing impact energetics of the samples and comparing them to other common reference materials used for impact protection, such as Kevlar and Spectra.

The paper shows that 3D nanoarchitected materials can exhibit not only great static properties but also extreme energy dissipation under supersonic microparticle impact, as shown in Figure 2.1. Namely, the material was experimentally shown to have approximately 70% greater specific energy dissipation when compared to Kevlar composites and nanoscale polystyrene films for the same specific energy impact energies. Furthermore, the paper experimentally showed qualitative modes of impact - elastic impact, particle capture, full penetration and capture dominated modes, and how combinations of relative density of the material and impactor velocity affects which mode is present. At low velocities (below approximately $50m/s$) both materials showed fully elastic impact behavior. For the less dense lattice ($\bar{\rho} \approx 14\%$) the dominant impact mode was bounce-back for lower impact velocities (below $490m/s$) and penetration impact mode for higher velocities (above $490m/s$). For the lattice with higher density ($\bar{\rho} \approx 23\%$) also bounce-back was the dominant mode for lower velocities (below $515m/s$) and impactor capture was present for higher velocities (above $515m/s$).

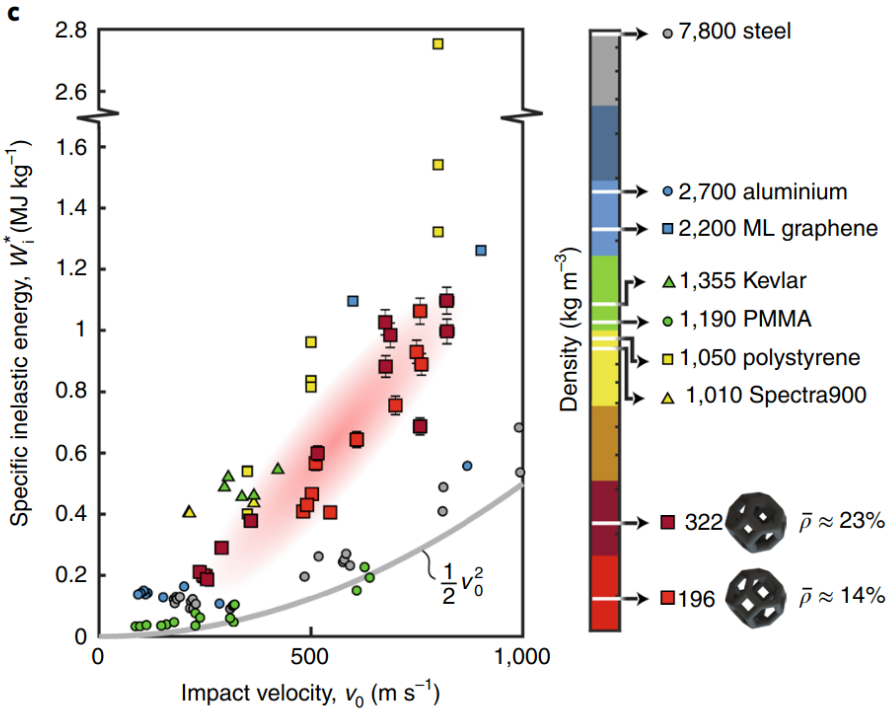

Figure 2.1: Comparison of mass normalized impact energy of various materials as function of impact velocity [1].

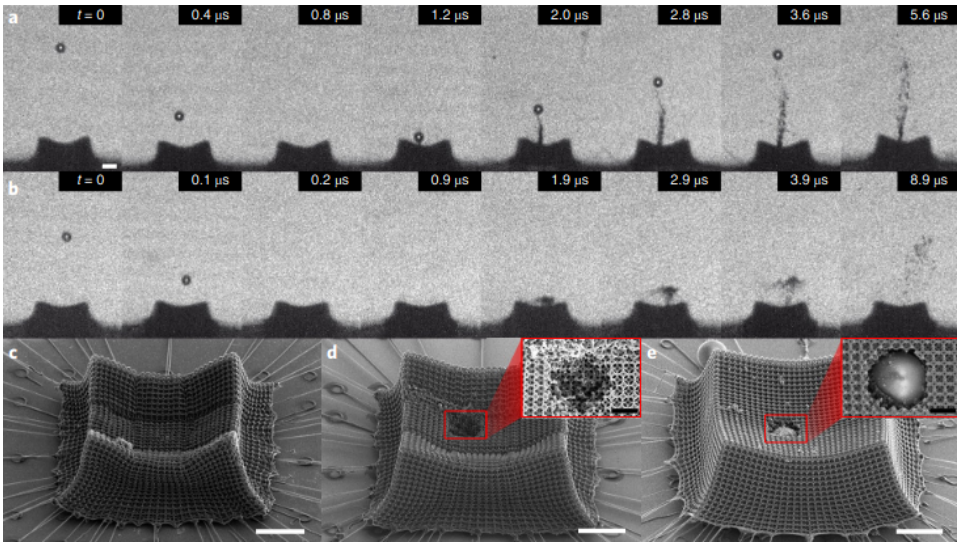

Figure 2.2: Rebound impact mode shown in row **a**, Capture impact mode shown in row **b** and post impact micrograph images of the nanoarchitected carbon lattices used for analysis of experiments shown in **c**. [1]

An effort to model the physics of impact of architected materials more in-depth was made in a follow up research that attempts to decouple impact dissipation mechanisms ([2]). Combining impact experiments, quasi-static experiments and high-fidelity simulation have generated insights into two coupled mechanisms of energy dissipation: material compaction and particle induced fracture. A set of dynamic and quasi-static experiments and finite element simulations were performed in an attempt to identify the roles of each of the energy dissipation mechanisms and different failure types in each of the lattice architectures. Additionally, an experimental framework wherein two types (octet and tetrakaidecahedron) suspended lattice samples and a monolithic plate sample(Figure 2.3) were impacted by microparticles with velocities of up to $850 m/s$ was developed as a key part of this research.

Their experimental findings demonstrate that the incorporation of an architecture lattice into materials leads to at least a 47% increase in mass-normalized energy dissipation compared to their monolithic polymer counterparts.

The paper presents an improved (Figure 2.3)(in comparison to [1]) experimental model that allows to isolate boundary effects from the material response. This is achieved by modifying the shape of the experimental setup, such that there are no interactions with the substrate or with the elastic precursor waves reflecting from the support. The experimental geometry that was used for this was manufactured using two-photon lithography out of IP-dip photoresist. The interactions with the substrate are removed by supporting the lattice from the sides instead of from the bottom (such as in Figure 2.2). Additionally, the effect of elastic precursor waves is minimized by making the test sample sufficiently large such that the time for the waves to travel to the edge of the sample and back is longer than the duration of the impact. Furthermore, the research compares mass-normalized energy dissipation properties of two morphologies - octet and tetrakaidecahedron architected materials. Both of these are fabricated to have relative density of $33 \pm 1.2\%$ and unit cell size of $6.7 \pm 0.1 \mu m$. It should also be noted that due to the manufacturing methods the lattice-beams had minor ellipticity of their cross-sections with the average major-to-minor axis ratio of 1.3. Similarly, to the experimental setup used in [1] an additional type of specimen was produced for baseline comparison - a monolithic plate of the same material with the thickness of $7.6 \pm 1.8 \mu m$. The resulting lattice designs consisted of $32 \times 26 \times 5$ tessellations of unit cells consequently having a size of $214 \times 174 \times 33.5 \mu m$.

As a part of impact experiments SiO_2 spheres with diameter of $33 \pm 2 \mu m$ where accelerated towards the center of the samples with impact speeds ranging from 300 to $850 m/s$. The impact event was measured using an ultra-high-speed camera and a microscope objective. For the post-impact measurement of the sample a scanning electron microscope was used. Consequently, the measurement were used to calculate the energy dissipation of the impact event using the formula Equation 2.1. Furthermore, by using lattice and crater parameters dissipated energy can be used to calculate dissipated energy dissipated per unit mass as seen in equation Equation 2.2 where $m_{cylinder}$ is the mass of the material displaced by the crater, ρ is the effective density of the crater, A_{crater} is the cross-sectional area of the crater cylinder and t is the thickness of the sample/cylinder. This allows to evaluate the energy efficiency of the impact event and compare the energy dissipation properties of the materials for given conditions. Additionally, it is found that the craters formed by impact in the lattice materials are well defined 1D cylindrical shape as opposed to the radial cracking and gouging of monolithic materials. This cylindrical shape assumption is then used for to design further experiments, numerical simulations and calculations including Equation 2.2.

$$W_{dis} = 1/2 m_{sphere} \left(v_i^2 - v_f^2 \right) \tag{2.1}$$

$$\bar{W} = \frac{W_{dis}}{m_{cylinder}} = \frac{W_{dis}}{\rho A_{crater} t} \tag{2.2}$$

In [2] by evaluating the impactor velocities before and after impact it is found that the nanoarchitected lattice materials have higher mass normalized energy dissipation while the monolithic polymer dissipates the most absolute energy ($6.00 \mu J$) at impact velocity of $820 m/s$. Of the two lattice architectures octet is identified to have the highest with the maximum value of $0.47 MJ/kg$ at impact velocity of $715 m/s$. Thus octet architected materials are identified as having superior energy dissipation properties compared to tetrakaidecahedron architected materials.

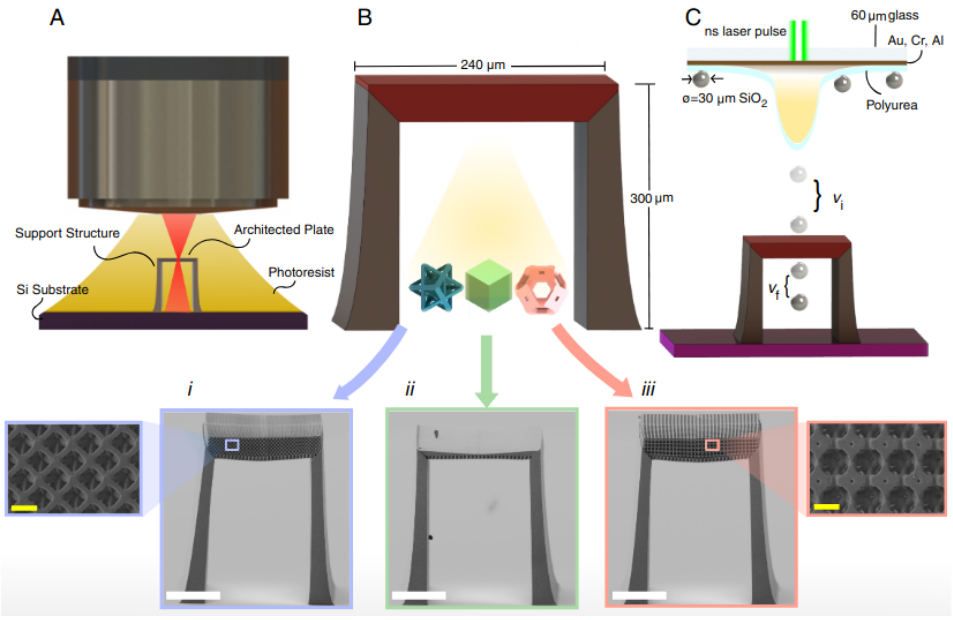

Figure 2.3: The experimental setup used for decoupling particle impact dissipation mechanisms. Part **A** shows the manufacture of the architected plate via two-photon lithography. Part **B** shows the three types of materials used in this work: octet, monolithic and tetrakaidecahedron architecture respectively. White scale bars $100\mu m$, yellow scale bars $5\mu m$. Part **C** demonstrates the laser accelerated $30\mu m$ impactor as well as pre-impact velocity v_i and post-impact velocity v_f [2].

2.1.2. Dimensional analysis of nanoarchitected material impact

Another effort made in [2] was dimensional analysis of the experiments to predict the impact response based on material parameters and impact conditions. The dimensional analysis similarly to that done in [1] is inspired by planetary impact. The methodology follows the Buckingham-Pi theorem to reduce the number of independent variables governing the problem into a set of dimensionless groups. The study considers parameters key to finite plate suspended lattice impact, such as impactor velocity (V_i), post-impact velocity (V_f), impactor density (ρ_i), target material yield strength (ς_y), relative density of the lattice ($r\bar{h}o$), and plate thickness (t)(Equation 2.3). These variables are reduced into five dimensionless groups Equation 2.4:

$$\frac{v_f^2}{\sigma_y} = f\left(\frac{v_i^2}{\sigma_y}, \frac{r}{t}\frac{\rho_{\text{sphere}}}{\rho}\bar{\rho}, \frac{\rho_{\text{sphere}}}{\rho}, \bar{\rho}\right) \tag{2.3}$$

$$\Pi_{v_f} = f\left(\Pi_{v_i}, \Pi_m, \Pi_\rho, r\bar{h}o\right) \tag{2.4}$$

These terms can be arranged to produce a relation that allows to predict predict the post-impact velocity as as function of initial velocity of the impactor, impactor parameters and plate parameters with first order accuracy. The terms are arrange in a power relation with free parameters α and β as shown in Equation 2.5. By linearly fitting the variables to the experimental data the values found are $\alpha = 1.0$ and $\beta = 0.7$ with both values being very similar for both octet and tetrakaidecahedron plates but considerably different for the monolithic plate. The resulting relation is graphed in Figure 2.4. From the dimensional analysis it is then concluded, exponent fit of α indicats that the relation between the energy of the impactor before and after the impact follows an approximately linear relation as long the impact velocity is above the plates ballistic limit and below hypervelocity regime. Furthermore, the fit of β provides understanding of the effect of the size of the impactor - for impactor much larger than the thickness of the lattice energy dissipation is dominated by momentum transfer to debris. While impactors much smaller than the thickness the dominant dissipation mechanism is the energetic cost of creating the cylindrical fracture surface. Finally, it can be noted that it is found that the post impact velocity increases with increasing impactor radius.

$$\Pi_{v_f} = \Pi_{v_i}^{\alpha}\Pi_m^{\beta} \tag{2.5}$$

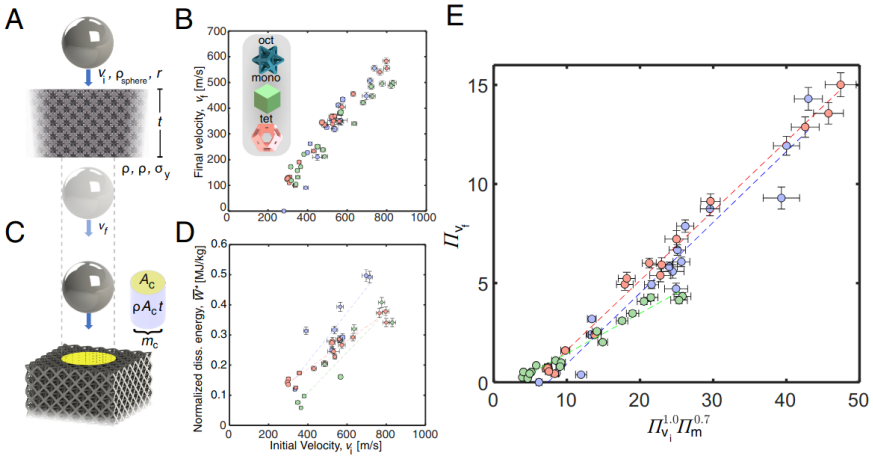

Figure 2.4: Impact analysis involving comparing pre and post impact impactor velocities and the mass of the materials in the cylindrical crater. Parts **A** and **C** show the used properties of the lattice, impactor and impact crater. Parts **B** and **D** show the final velocity and normalized dissipated energy as functions of initial velocity. Part **E** shows the dimensionless groups Π used for dimensional analysis [2].

2.1.3. Analysis of metamaterial impact experiments

In order to attempt to gain greater insight into impact dissipation mechanisms and to understand under what conditions each of the mechanisms is dominant a set of quasi-static and dynamic experiments were performed as well as a finite element simulation was employed. In [2] three main contributions to energy dissipation are assumed (Equation 2.6): dynamic compaction W_{comp}, kinetic energy of the ejecta W_{in} and fracture energy W_f. It is further assumed that "kinetic energy imparted to ejecta in our microlattices should be approximately the same for impact events of equivalent particle size, through-plate mass, and velocity"[2] thus leaving compaction and fracture as the key contributors to be examined.

$$W_{tot} = W_{comp} + W_{frac} + W_{inert} \tag{2.6}$$

An experimental setup was made where a nanonidenter compressed $10x10x10$ cell speciments of both architectures and measured the point of effective densification, effective Young's modulus and yield strength thus being able to obtain the integral of the stress-strain curve or in other words the compression energy Figure 2.5. Remarkably, it was found that the mass normalized energy disspation of the tetrakaidecahedron was higher than that of the octet architecture which is opposite to the trend that was found during the impact performance experiments. To help gain better understanding of the unexpected results a high fidelity finite element model was employed that incorporated on-linear strain hardening, beam contact, and fracture. The finite element model largely managed to capture the higher compressive energy behaviour of the tetrakaidecahedron lattice as can be seen in the graphs in Figure 2.5.

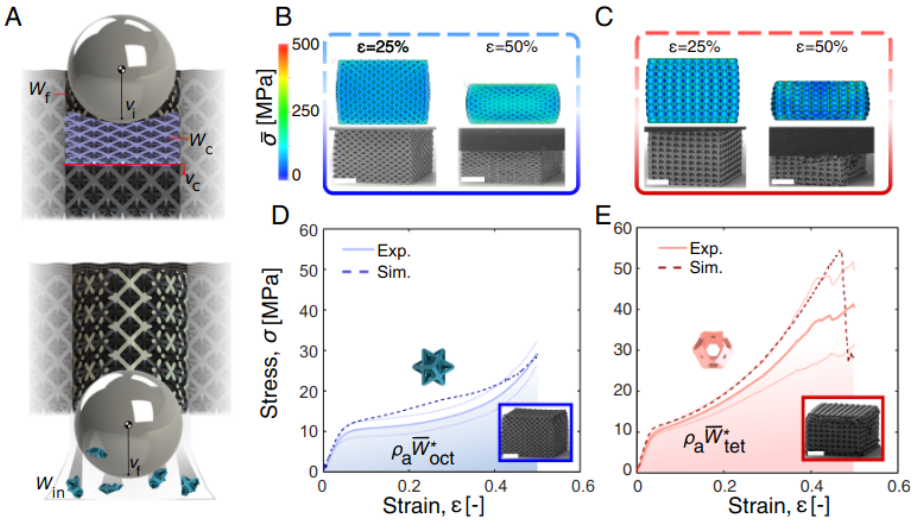

Figure 2.5: Decoupled compaction mechanisms in microlattices. Part **A** contains energy dissipation during impact showing fracture (W_f), compaction (W_c), and inertia (W_{in}), with compaction front speed v_c and projectile velocities v_i and v_f. Parts **B** and **C** show simulated and experimental uniaxial compaction of $10 \times 10 \times 10$ octet and tetrakaidecahedron lattices. Parts **D** and **E** show corresponding stress–strain curves; solid lines show averages, dotted lines indicate standard deviations. (Scale bars: 20 μm.) [2].

To capture the fracture behavior of the architected materials, experiments were performed that consisted of a cylinder being quasi-statically inserted into the material as illustrated in Figure 2.7. The well defined area of the fracture and the specimen including the cross-sectional area of the fracture, depth of the indentation, thickness of the specimen and the stress curves allowed to easily calculate the mass normalized energy dissipation. While the octet showed noticeably lower energy dissipation in the octet experiments both architectures showed similar energy dissipation in this indentation experiment pointing towards a greater fracture contribution in the octet architecture compared to tetrakaidecahedron architecture. This observation was further analyzed using finite element model and it was found that the mass normalized dissipated energy from experiments showed excellent agreement with simulation data. Additionally, it was noted that that the unit cell close to the fracture surface deform mainly in shear mode as shown in *i* part of Figure 2.6. Thus more finite element models were setup with a single unit cell in simple shear, as shown in *ii* and *iii* part of Figure 2.6 that showed great shear stress and strain components in the elements. It was also found that octet lattices have greater mass normalized shear energetic cost of $36.9kJ/kg$ than tetrakaidecahedron architectures with $21.0kJ/kg$. This higher octet energy support the findings in the particle impact experiments.

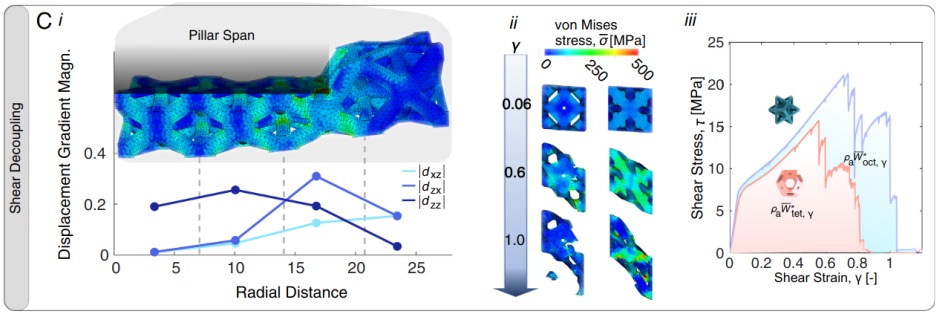

Figure 2.6: Parts **i** and **ii** display displacement gradients vs. radial distance in octet lattices. Part **iii** show simple shear simulations with corresponding stress–strain responses [2].

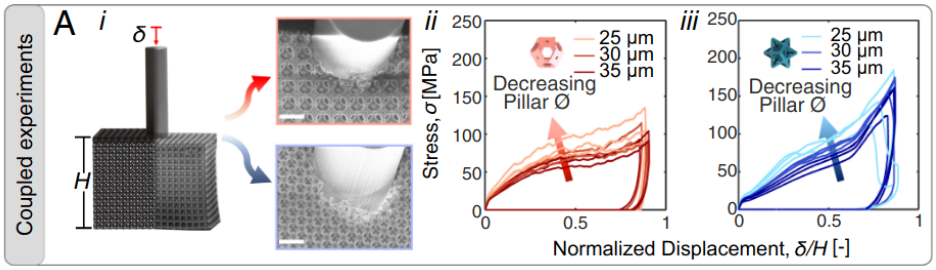

Figure 2.7: Part **i** shows CAD and SEM of pillar-induced indentation into octet and tetrakaidecahedron lattices. (Scale bar: 10 μm.) Parts **ii** and **iii** display stress vs. normalized displacement for varying pillar diameters [2].

2.1.4. Effect of strain-rate

Finally, work was performed to analyze the strain-rate effect on the energy dissipation properties of the architected materials. Energy dissipation mechanisms across different strain rates were investigated through a series of uniaxial compaction and pillar indentation experiments and simulations. These experiments, conducted at strain rates of 10^{-1} and 10^{1} s^{-1}, revealed dynamic stiffening effects and consistent mass-normalized energy dissipation metrics with quasi-static experiments. At higher strain rates, explicit simulations showed the development of compaction shocks and a significant increase in energy dissipation for velocities beyond 200 m/s. For the indentation simulation the cylindrical crater remained well defined with a compaction zone underneath for all velocities. In the simulation the octet architecture exhibited a greater relative increase in energy dissipation compared to the tetrakaidecahedron architecture, consistent with observations from quasi-static experiments.

2.1.5. Conclusion

In conclusion the research [1] demonstrates that nanoarchitected materials exhibit significant energy dissipation under supersonic microparticle impact, outperforming traditional materials like Kevlar. Additionally, research [2] further investigates the impact dissipation mechanisms, identifying material compaction and particle-induced fracture as key contributors. The findings show that octet lattice architectures have superior energy dissipation properties compared to tetrakaidecahedron architectures. Additionally, dimensional analysis and finite element simulations provide insights into the impact response and energy dissipation mechanisms, emphasizing the importance of lattice architecture in enhancing material performance under high-velocity impacts.

2.2. Overview of impact physics

Since one of the motivating factors for the research is the impact of microparticles on nanoarchitected materials, it is important to understand the physics of impact. This section aims to provide an overview of the key aspects of impact physics that are relevant to the research, such as looking into one of the key potential applications of metamaterials of defence against space debris or other ballistic applications and understanding the key physical phenomena of impact.

In figure Figure 2.8 the distribution of publications about impact for some velocity ranges is given [17]. The velocity distribution indicates that majority of work is done for speed above $\approx 1km/s$ that generally known as hypervelocity impacts. Although it must be noted that the traditional classification based solely on velocity fails to account for the influence of material properties and their varying responses. The literature presents several alternative criteria that incorporate material characteristics, such as strain rate, the "Bulk Mach number", and the pressure criterion. However, these criteria either rely on quantities that are difficult to measure in empirical setups (e.g., strain rate) thus direct measurement of impact outcomes at hypervelocity is highly challenging. Consequently, experimental characterization of hypervelocity impacts typically relies on high-speed cameras, witness plates, and post-mortem analyses [18].

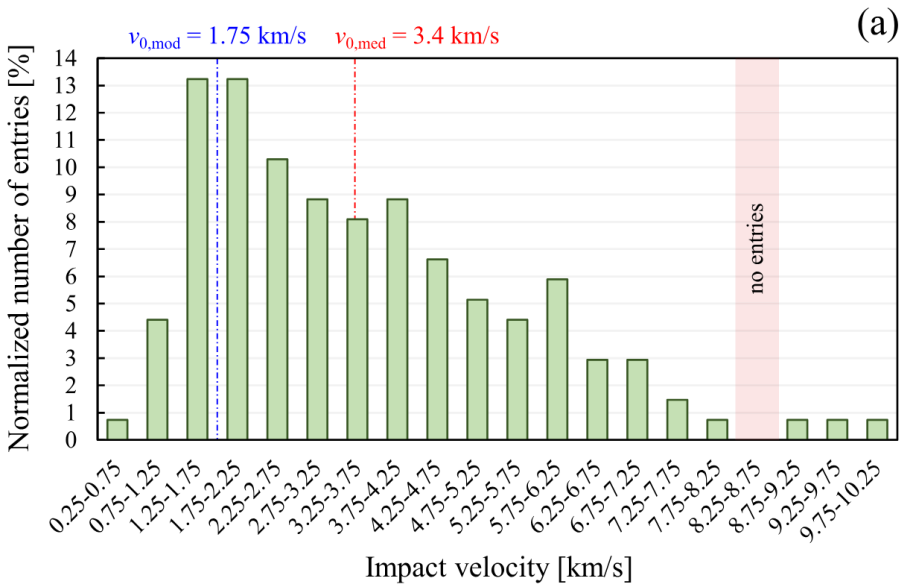

Figure 2.8: Distributions of publications about impact for various velocities as compiled by [17].

2.2.1. High velocity impacts

Hypervelocity impacts in orbit

High-velocity impact physics is characterized by extreme pressures, strain rates, and energy dissipation mechanisms that significantly alter material behavior. When a projectile impacts a target at speeds exceeding 1 km/s, the interaction can no longer be described by conventional elastic or plastic deformation theories [19]. Instead, it requires hydrodynamic considerations where materials behave like compressible fluids under impulsive loadings. The initial phase of impact generates a sequence of shock waves that travel through both the projectile and the target. These waves induce rapid pressure increases, leading to phase changes such as melting and vaporization. The hydrodynamic stress distribution governs how materials flow, fragment, and disperse, often leading to extensive damage beyond the initial impact site.

Hydronamic model

A crucial phenomenon in high-velocity impacts is the generation and propagation of shock waves. The impact event initially produces an elastic wave traveling at the speed of sound in the material. However, once the stress surpasses the Hugoniot elastic limit ($\sigma_{hel} \approx \frac{2}{3}\sigma_y$), plastic deformation occurs, generating plastic waves that travel at increasing speeds with higher strain rates.If the impact energy is high enough, the plastic wave overtakes the elastic one, forming a steep-fronted shock wave that creates discontinuities in material properties. These waves can reflect and refract at material interfaces, leading to destructive interactions that enhance damage through mechanisms such as spallation, in which tensile stress causes material separation and fragmentation. This creates the necessity for a hydrodynamic model at higher impact speeds. This means that the models are no longer significantly affected by material strength but instead by material densities and pressure-volume relationships.

Hydronamic remain indispensable for simulating high-velocity impacts, yet they still face several inherent limitations. Their results are highly sensitive to the choice of material equation-of-state, strength, and damage models, many of which are poorly constrained at the extreme pressures, temperatures, and strain rates encountered during an impact. Numerical diffusion and limited mesh resolution can smear shock fronts and underestimate peak pressures, while artificial viscosity—necessary for shock stabilization—tends to damp fine-scale features such as jetting or spall. Most codes also struggle to couple disparate physical regimes (e.g., solid mechanics, melt flow, and vapor phase) within a single run, requiring ad-hoc hand-offs that introduce additional uncertainty. Finally, the computational cost of 3-D, high-resolution simulations often forces researchers to simplify target geometry

or rely on axisymmetric assumptions, limiting fidelity when studying oblique or heterogeneous impacts.

Plastic and shock heating
Thermo-mechanical coupling plays a critical role in high-velocity impacts, particularly in the transition from plastic to shock-dominated regimes. Two primary heating mechanisms arise: plastic heating (Equation 2.7), where kinetic energy dissipates as heat due to plastic deformation which plays more important role at lower speeds, and shock heating, where compression raises the internal energy of the material that is more important at higher speeds. At extreme velocities, melting and vaporization become dominant, with a significant portion of the debris cloud consisting of molten or vaporized material. The interplay between mechanical and thermal effects influences material response, with phenomena such as strain rate-dependent softening and thermal-induced failure occurring at different stages of impact [17].

In Equation 2.7 the relation for plastic heating is given. ΔT is local temperature increment due to plastic work to computed in a simulation. ΔW_{pl} is the plastic work done on the material, ρ is the material density and c_v is the specific heat capacity at constant volume. The coefficient β_{tq}

$$\Delta T = \beta_{tq} \frac{\Delta W_{pl}}{\rho c_v} \tag{2.7}$$

Fragmentation and debris
Fragmentation and debris cloud formation are key aspects of high-velocity impact physics, particularly in thin-walled structures such as satellites and space debris shielding. The impactor and target undergo extensive fragmentation, with debris cloud morphology depending on parameters such as impactor velocity, material properties, and geometric constraints. The debris cloud consists of distinct regions: an ejecta veil of backward-moving material, an expanding bubble of plate debris, and a structured core of projectile fragments as shown in Figure 2.9. Understanding debris cloud evolution is essential for designing protective structures and mitigating the risks associated with hypervelocity impacts in aerospace applications.

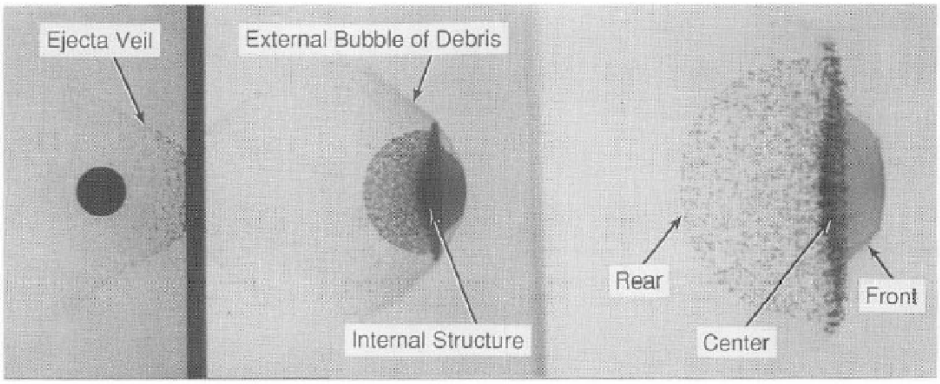

Figure 2.9: Various feature of a debris cloud of an aluminium sphere impacting a thin aluminium plate [18].

2.2.2. Low-fidelity models for ballistic impacts

Engineering models for ballistic impact provide simplified yet effective descriptions of the penetration and perforation processes, offering a balance between computational efficiency and physical accuracy. These models are often used in situations where full-scale numerical simulations are too computationally expensive or where experimental data is limited. They typically focus on energy balance, momentum transfer, and material deformation mechanisms to predict projectile penetration, target failure, and residual velocities [20].

One of the earliest and most fundamental engineering models applies to thin target plates impacted by rigid projectiles. These models, such as those developed by Bethe and Taylor, consider the plastic work done to expand a hole in a ductile plate. Other approaches, like those by Recht and Ipson (Equation 2.8), use energy and momentum conservation principles to estimate velocity loss and define a ballistic limit velocity—the minimum speed required for a projectile to perforate a target. While these models provide reasonable accuracy for specific material and impact conditions, they are often limited in their ability to capture complex failure mechanisms like plugging or petalling [20].

The equation below allows to express residual velocity V_r as a function of the initial impact velocity V_0, the ballistic limit velocity V_L (the minimum velocity for perforation or the maximum impact velocity for which the residual velocity is zero), the mass of the cylindrical or conical pluc M_{tb} and the mass of the projectile M:

$$V_r = \left(\frac{M}{M + M_{tb}} \right) \left(V_0^2 - V_L^2 \right)^{1/2} . \tag{2.8}$$

For moderately thick plates, more sophisticated models, such as the Awerbuch-Bodner model (Figure 2.10), incorporate multiple deformation stages. This model describes perforation as a three-step process: (1) initial penetration with compressive and inertial resistance, (2) a shearing phase where material begins to yield, and (3) plug ejection as a distinct mass of target material separates from the plate. The Ravid-Bodner model extends this approach by incorporating two-dimensional effects and considering additional factors such as bulging and rear-surface deformation. These refinements help capture a broader range of projectile-target interactions, making the models applicable to a wider variety of impact scenarios [20]. In this case equation of motion can be written as:

$$\frac{d}{dt}(mv) = -\left(F_i + F_c + F_s\right), \tag{2.9}$$

or with the assumption of one-dimensional and plastic zone of target material in front of the projectile moving with the same velocity as the projectile:

$$\rho_{\mathrm{t}} A v^2 + \left(m_0 + \rho_{\mathrm{t}} A z\right) v \frac{\mathrm{d}v}{\mathrm{d}z} = -\left(F_{\mathrm{i}} + F_{\mathrm{c}} + F_{\mathrm{s}}\right), \tag{2.10}$$

where F_i is the inertial resisting force, F_c is the compressive resisting force, F_s is the shear force, m_0 is the projectile mass, ρ_t is the target density, A is the cross-sectional area of the projectile, v is the velocity of the projectile, and z is the penetration depth.

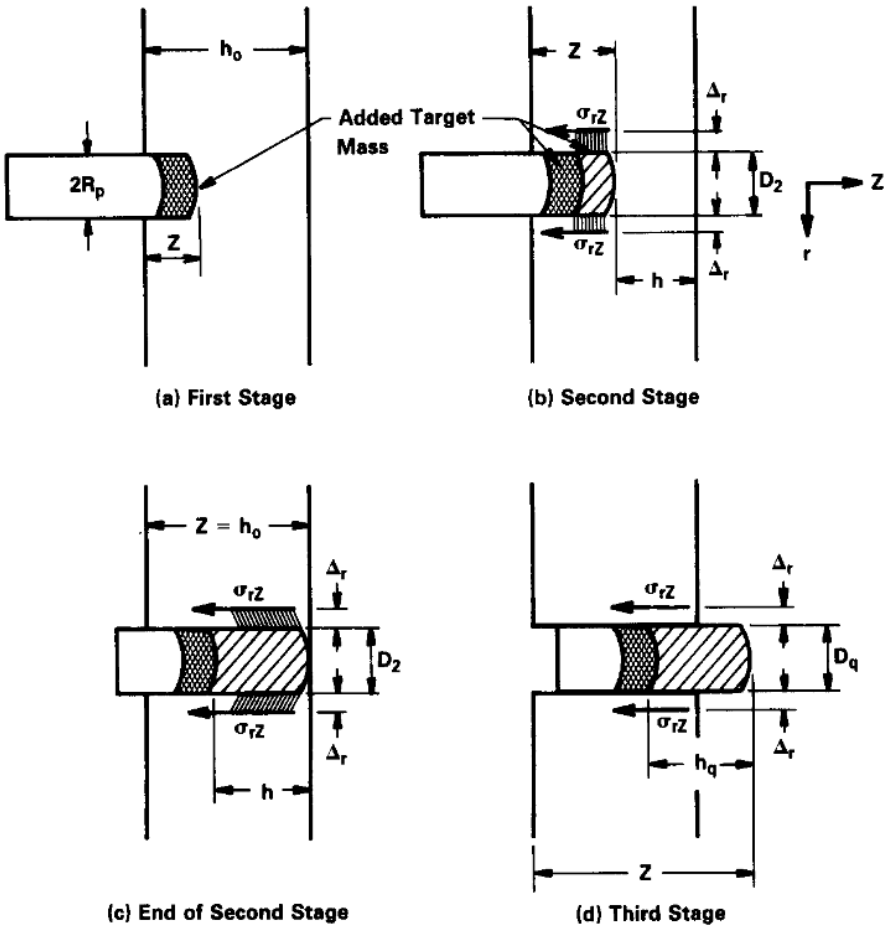

Figure 2.10: Four distinct phases of the Awerbuch-Bodner model[20].

At higher velocities (above $\approx 1km/s$), impact behavior shifts towards hydrodynamic effects, where both projectile and target materials behave more like fluids. The Alekseevskii-Tate model modifies classical Bernoulli equations (Equation 2.11) to include projectile and target strength effects, providing insights into penetration efficiency and material erosion. These hydrodynamic models are particularly useful for understanding hypervelocity impacts, where material strength plays a secondary role compared to inertial and shock-wave effects and are used as standrad reference for velocities above $1km/s$ [20].

The modified Bernoulli equation (Equation 2.11) uses the properties of both the projectile and target to find various velocity terms as shown in Figure 2.11. T is the strength of the target usually about three times the uniaxial ultimate stress of the material. Y is the strength of the projectile while ρ_t and ρ_p are the target and projectile densities and v is the speed of the rear of the projectile and u is the penetration speed. Consequently the differential equation describing the force acting on the projectile is given in Equation 2.12.

$$\frac{1}{2}\rho_{\mathrm{t}}u^2 + T = \frac{1}{2}\rho_{\mathrm{p}}(v-u)^2 + Y \tag{2.11}$$

$$\rho_{\mathrm{p}} l \frac{\mathrm{d}y}{\mathrm{d}t} = -Y \tag{2.12}$$

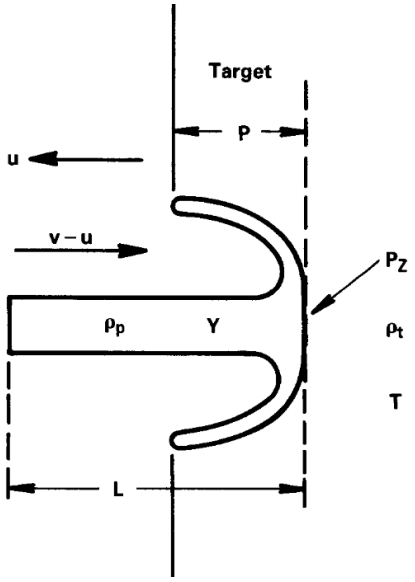

Figure 2.11: Key variables of hydrodynamic penetration model [20].

A constant challenge for engineering models is to unify low- and high-velocity impact mechanics by incorporating strain rate effects, thermal softening, and hydrodynamic penetration principles. Two-dimensional models, such as the Ravid-Bodner formulation, attempt to account for more complex material flow and failure modes, reducing the reliance on empirical corrections. While these models continue to evolve, they remain a powerful tool for predicting impact outcomes efficiently, particularly in applications where detailed numerical simulations are impractical [20].

Overall, engineering models for ballistic impact provide a structured and computationally efficient approach to understanding penetration mechanics. Though they are often based on simplifying assumptions and require empirical factors, their ability to offer quick and reasonably accurate predictions and to demonstrate what are the key effects to account in various impact conditions make them useful both in design applications and in order to gain understanding of the underlying physics.

2.2.3. Summary of impact physics

The key phenomena involved in an impact event depend on the velocity range and the material properties of the projectile and target. Consequently, the modelling methods also depend on the properties. In low-velocity impacts, elastic and plastic deformation dominate, while at high velocities, hydrodynamic effects and shock waves become significant. The transition between these regimes can involve even further complications since in that case both consideration of low and high velocity impact phenomena have to be accounted for.

Energy dissipation mechanisms

In summary, these are the main energy dissipation mechanisms during impact:

- **Plastic deformation:** Under low-to-medium velocity impacts, plastic deformation is typically the primary energy dissipation mechanism. It involves permanent deformation and strain hardening of the material, absorbing kinetic energy from the impacting body. This mechanism is particularly relevant for ductile truss lattice metamaterials where yielding is significant.
- **Fracture:** Fracture mechanisms become dominant at moderate-to-high impact velocities (since in that case the impactor has enough energy to fracture the material) or in brittle material systems. Energy dissipation occurs through the creation of new surfaces, crack propagation, and fragmentation. In lattice metamaterials, fracture energy absorption strongly depends on structural geometry, lattice connectivity, and inherent material toughness.

- **Shock waves:** At high-impact velocities, shock waves are significant and can significantly affect energy dissipation processes. They manifest as rapidly propagating discontinuities in stress, density, and velocity within the material, resulting in local heating and high strain-rate deformation. In truss lattice metamaterials, the geometry can influence shock wave propagation and attenuation.
- **Melting and vaporization:** These thermal mechanisms become relevant at extremely high-impact velocities (hypervelocity impacts), typically seen in ballistic and aerospace applications. Significant kinetic energy converts into heat, raising local temperatures sufficiently to cause melting or even vaporization of the material.
- **Kinetic energy transfer:** While not an energy dissipation mechanism per se, the redistribution and transfer of kinetic energy within the structure and between target and projectile play critical roles at all impact velocities. At lower velocities, kinetic energy is gradually dispersed throughout the lattice structure, while at higher velocities, momentum transfer can result in material ejection, fragmentation, and secondary impacts that require further modelling and consideration. "'

2.3. Computational model of the impact

This section outlines the various components of the computational model used to simulate the impact of lattice metamaterials. It aims to provide context to the models used. More detailed mathematical formulations of the models as used in the simulations are provided in the methodology section.

2.3.1. Kirchoff-Love beam

Truss-based lattice structures can effectively modeled using beam elements due to their simplicity, computational efficiency, and ability to accurately capture the primary load-bearing behavior of slender structural components. Beam formulations significantly reduce computational resources compared to solid elements, making them potentially suitable for modeling complex lattice structures under dynamic loading conditions, such as impacts.

The Kirchhoff-Love beam formulation is a classical theory that is predicated on the assumptions that cross-sectional planes remain plane and perpendicular to the neutral axis after deformation, effectively eliminating shear deformation effects. As a result, Kirchhoff-Love beams accurately describe bending-dominated behavior for slender beams where shear deformation is negligible [21]. This is a key limitation of Kirchoff-Love beams as it means that in case the slenderness of the beam is too low, other beam formulations, such as Timoshenko, are preferred.

Key properties of Kirchhoff-Love beams include their geometrical exactness, which allows for modeling large rotations and displacements without losing accuracy or consistency with physical principles [21]. This geometrically exact nature makes Kirchhoff-Love beam theory particularly suitable for capturing highly nonlinear behaviors exhibited by lattice metamaterials during impact, where large deformations are expected.

In summary, Kirchhoff-Love beams provide an efficient and accurate approach for modeling slender lattice structures under dynamic impact loads, particularly in the context of architected materials where bending and stretching dominate structural response [22]. Despite their limitations concerning shear deformation, their computational efficiency and accuracy make them an essential component of the finite element modeling framework used to investigate fracture and impact dynamics in lattice metamaterials. A more detailed mathematical description of the Kirchoff-Love beam formulation is presented in Section 3.2

2.3.2. Fracture mechanics

Accurate modeling of fracture phenomena is essential in simulations involving the impact of lattice metamaterials, as fracture processes significantly contribute to energy dissipation and affect the structural integrity of the material under dynamic loading conditions. The ability to predict crack initiation, propagation, and the associated energy release is vital for designing resilient architected materials

capable of absorbing and dissipating impact energies effectively.

The Cohesive Zone Model (CZM) is a widely adopted numerical approach to modeling fracture, which captures the process of crack formation and propagation through a predefined cohesive zone ahead of the crack tip. Within this cohesive zone, material separation is governed by cohesive laws—typically expressed as traction-separation relationships—that describe the progressive degradation of material stiffness until fracture occurs [23]. CZM effectively bridges continuum mechanics and classical fracture mechanics, allowing for seamless integration within finite element frameworks.

Key properties of CZM include the explicit definition of a cohesive law, typically involving parameters such as cohesive strength, fracture energy, and characteristic length scales, which can be directly calibrated from experimental data. Admittedly, this dependance of experimental data can be a substantial obstacle as obtaining data for accurate results requires extensive experimental work. Additionally, the model can handle complex fracture phenomena, including mixed-mode loading conditions, and is particularly advantageous in modeling ductile fracture or delamination processes commonly observed in lattice metamaterials during impacts [23].

The primary advantages of the CZM approach lie in its ability to simulate fracture initiation and propagation without pre-existing cracks explicitly defined in the geometry, as well as its flexibility in handling nonlinear and mixed-mode fracture conditions [23]. Moreover, CZM can be integrate with discontinuous numerical methods like the Discontinuous Galerkin approach, enabling efficient modeling of evolving cracks and multiple fractures in dynamic simulations.

Alternative fracture modeling approaches include classical linear elastic fracture mechanics, extended finite element methods, and peridynamics [23]. However, this work adopts a Cohesive Zone Model CZM framework due to this method already having been implemented for this purpose in the *Summit* framework. Specifically, it utilizes a variant of CZM in which the cohesive laws are formulated in terms of stress resultants, rather than the conventional traction–separation relationships [24, 25]. A detailed description of the CZM implementation used in this work can be found in Section Section 3.3.

2.3.3. Galerkin methods

The Discontinuous Galerkin (DG) method is a powerful numerical technique used for solving partial differential equations, notably those involving high gradients, discontinuities, and evolving interfaces—characteristics prevalent in dynamic impact simulations and fracture mechanics. Unlike traditional continuous Galerkin methods, DG allows for discontinuities between elements, enabling accurate modeling of problems involving crack propagation, wave propagation, and localized failure phenomena [26].

At its core, DG discretizes the computational domain into elements where solutions are approximated independently, with continuity enforced weakly through flux terms at element interfaces. This approach provides significant flexibility in handling complex boundary conditions and interface phenomena, essential in accurately simulating impacts involving lattice metamaterials where fractures and large deformations are anticipated.

Key properties of the DG method include its high-order accuracy, locality of approximation, and inherent ability to parallelize computations effectively. The method supports high-order polynomial approximations within each element, facilitating precise capture of intricate stress and deformation fields during impact. Moreover, the locality of DG computations simplifies adaptive mesh refinement, particularly beneficial in dynamically evolving fracture simulations.

Advantages of the DG method prominently include its robustness in handling discontinuities without the need for additional interface tracking mechanisms, as well as its superior accuracy for problems with sharp gradients or shocks. When coupled with cohesive zone models (CZM), DG effectively captures fracture initiation and propagation with excellent numerical stability. Its inherent parallelizability also enables efficient computational scalability for large-scale simulations typical in lattice structure impacts.

However, the DG method's primary disadvantage lies in its relatively higher computational cost due to increased degrees of freedom compared to continuous methods, resulting from the duplicated nodes at element interfaces. This computational overhead can be substantial, especially in large three-dimensional simulations. Additionally, implementing boundary conditions and interface flux computations accurately requires careful numerical treatment, which can increase model complexity.

In summary, the Discontinuous Galerkin method provides an advantageous balance of accuracy, robustness, and flexibility for modeling the complex phenomena associated with dynamic impact and fracture of lattice-based metamaterials. A more detailed mathematical formulation of the Discontinuous Galerkin discretization as used in this work is presented in Section 3.4.

2.3.4. Time solver

Since the model will be used to simulate impacts, the problem is not static and a time dependent solver is needed. There exist two types of time solvers: implicit and explicit. Due to the fact that other necessary features of the *Summit* framework, in which this work is being performed, have been developed for an lumpd mass explicit Newmark solver, the explicit time solver is used for this work. This subsection aims to outline what is the used time solver and how does it compare to other time solvers. More detailed explanation of the explicit time solver and the Newmark method is given in Section 3.5.

The key difference between explicit and implicit solvers by examining basic dicretization of a derivative of function $u(t)$ [27]:

$$\frac{du}{dt}(t) \approx \frac{u(t+\Delta t) - u(t)}{\Delta t}, \tag{2.13}$$

with Δt as a small, positive parameter representing the time step. Consequently there are (at least) 2 ways to rewrite the above equation to obtain a discrete sequence of $u_n \approx u(n\Delta t)$ -
explicit:

$$u_n = u_{n-1} + \Delta t f\left(u_{n-1}, t_{n-1}\right), \tag{2.14}$$

and implicit:

$$u_n = u_{n-1} + \Delta t f\left(u_n, t_n\right). \tag{2.15}$$

The formulation in Equation 2.14 is called the explicit Euler method and Equation 2.15 is called the implicit Euler method. Since the implcit form does not allow to express u_n in terms of u_{n-1}, the implicit method requires solving a system of equations at each time step. This is in contrast to the explicit method, which allows for direct computation of u_n from u_{n-1} and the function f. Thus, the explicit method is generally simpler and computationally less expensive per time step than the implicit method. While this, example considers only the simplified case of the Euler method, similar distinctions can be made for other solvers [27].

The choice of a time intgeration method can influence system dynamics, stability of the solution, computational speed and the robustenss of solver. Explicit time integration methods are widely used in computational mechanics, particularly for dynamic problems involving large deformations, nonlinear material behavior, and contact interactions but unlike many implicit schemes explicit schemes are not unconditionally stable. On the other hand, implicit time integration methods are often preffered for stiff problems where an explicit method would require very small time steps to maintain stability.

The Euler schemes are first order scheme. By using a higher order approximation of the derivative higher order solvers have been developed. These allow to achieve higher accuracy than lower order schemes at the cost of more computational effort, more complex implementation and possible issues with discontinuities and boundaries. Generally, it is agreed that despite the drawbacks, higher order schemes are more efficient [28]. The Newmark solver used in this work is a second order scheme.

Lastly, it should be mentioned that there exist fixed vs variable step time solvers. In cases where the problem is highly dynamic it might be beneficial to adjust the time step size during the simulation. This

is especially useful in cases where the solution is expected to change rapidly in some regions of the domain but not in others. In such cases, a variable time step solver can adaptively refine the time step size based on the local behavior of the solution, allowing for more efficient computations. While this feature can be very beneficial it is difficult to implement and it is not used in this work.

2.4. Contact formulation

In this section a general contact formulation is presented along with two most commons implementations of contact condition: Lagrange multiplier method and penalty method, as based on the work of Wriggers [29]. Furthermore, the contact methods are compared for their advantages and disadvantages.

2.4.1. General contact formulation

To intorduce contact problem a general contact formulatio is presented as explained by Wriggers [29]. Here a solid with a rigid surface is considered in three-dimensional linear elasticity. In this problem, as shown in Figure 2.12, the motion of a solid body is constrained by a rigid surface and thus it is called a unilateral contact problem.

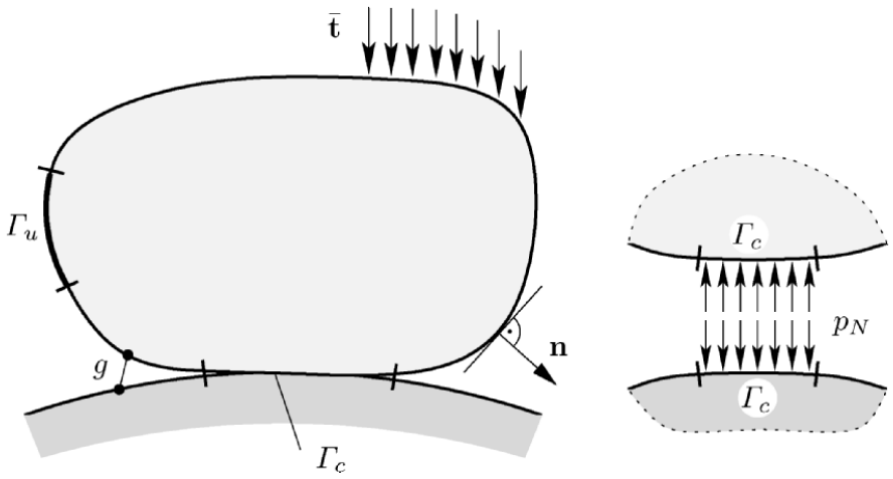

Figure 2.12: Unilateral contact of an elastic solid [29]

Here, $\bar{\boldsymbol{t}}$ represents a distributed traction acting on the body B, while $\boldsymbol{n}$ is a unit vector normal to the surface of the body. The boundary Γ_u corresponds to the region where Dirichlet boundary conditions are applied. The function g, known as the gap function, defines the contact separation, while Γ_c represents the contact boundary, and p_N denotes the contact pressure. Additional parameters not depicted in Figure 2.12 include the displacement field $\boldsymbol{u}$, the stress tensor $\boldsymbol{\sigma}$, the boundary Γ_σ, and the distributed force vector $\bar{\boldsymbol{f}}$. Based on these quantities, the linear elastic equilibrium equation can be expressed [29] as:

$$\operatorname{div} \sigma = \bar{f}. \tag{2.16}$$

By assuming a linear strain field, Green-Lagrange strain tensor displacement gradient is used where stain is:

$$\boldsymbol{\epsilon} = \frac{1}{2}\left(\nabla \boldsymbol{u} + \nabla \boldsymbol{u}^T\right). \tag{2.17}$$

The constitutive relation is given by Hooke's linear law with $\mathbb{C}$ as the linear constitutive tensor:

$$\sigma = \mathbb{C}\epsilon. \tag{2.18}$$

Next, the Dirichlet and Neumann boundary conditions as well as the contact conditions can be summarized as:

$$\begin{aligned} \boldsymbol{u} &= \mathbf{0} && \text{on } \Gamma_u \\ \boldsymbol{\sigma n} &= \bar{\boldsymbol{t}} && \text{on } \Gamma_\sigma \\ u_N - g &\leq 0 && \text{on } \Gamma_c \\ p_N &\leq 0 && \text{on } \Gamma_c \\ \left(u_N - g\right) p_N &= 0 && \text{on } \Gamma_c. \end{aligned} \tag{2.19}$$

In Equation 2.19 line one describes the non-penetration condition, line two the non-positive normal stress condition, and lines three through five collectively form the complementarity conditions, originally defined in the Signorini's problem [30, 31]. Let $\boldsymbol{u}$ be the solution to Signorini's problem, and let V denote the space of vector-valued, real functions defined on B. The weak form is then stated as follows: find $\boldsymbol{u} \in V$ such that for all $\boldsymbol{v} \in V$ the following is true [29]:

$$\int_V \sigma \cdot \boldsymbol{\epsilon}(\boldsymbol{u} - \boldsymbol{v}) \mathrm{d}V = \int_V \bar{f} \cdot (\boldsymbol{u} - \boldsymbol{v}) \mathrm{d}V + \int_{\Gamma_\sigma} \bar{\boldsymbol{t}} \cdot (\boldsymbol{u} - \boldsymbol{v}) \mathrm{d}\Gamma + \int_{\Gamma_c} p_N(\boldsymbol{u}) \left(u_N - v_N\right) \mathrm{d}\Gamma. \tag{2.20}$$

In Equation 2.20 mathematical notation is used to express the virtual work principle. Namely, he virtual work produced by the stresses times the virtual strains is equal to the sum of the virtual work of the body forces and external loads. Stress $\sigma(u)$ is a function of displacement as defined in Equation 2.18. Rewrting the expression for virtual work in Equation 2.20 by applying conditions given in Equation 2.19 yields condition that the Signorini problem must satisfy:

$$\int_V \sigma \cdot \epsilon(u - v) \mathrm{d}V \geq \int_V \bar{f} \cdot (\boldsymbol{u} - \boldsymbol{v}) \mathrm{d}V + \int_{\Gamma_\sigma} \bar{\boldsymbol{t}} \cdot (\boldsymbol{u} - \boldsymbol{v}) \mathrm{d}\Gamma. \tag{2.21}$$

Subsequently, solutions to the Singori problem are governed by a variational inequality. This results in a nonlinear problem even in the static and linearly elastic regime. Furthermore, the inclusion of friction would further complicate the problem by introducing inequality constraints also in the normal direction and distinct constitutive behavior in the tangential direction at the contact interface. These complexities would pose additional similar mathematical challenges related to the existence and uniqueness of solutions in frictional contact problems.

The problem then is is often reformulated in mathematical and theoretical work as contact between two deformable bodies. The analysis then yields an equation with the same structure as Equation 2.21 except for the change of the of the domain: $B = \bigcup_{\gamma=1}^{2} B^\gamma$ is the union of both domains of the contacting bodies. The variational inequality then can be rewritten:

$$a(\mathbf{u}, \mathbf{v} - \mathbf{u}) \geq f(\mathbf{v} - \mathbf{u}), \tag{2.22}$$

where

$$a(\mathbf{u}, \mathbf{v}) = \int_B \varepsilon(\mathbf{u}) : \mathbb{C} : \varepsilon(\mathbf{v}) dV, \tag{2.23}$$

$$f(\mathbf{v}) = \int_B \overline{\mathbf{b}} \cdot \mathbf{v} dV + \int_{\Gamma_\sigma} \bar{\mathbf{t}} \cdot \mathbf{v} d\Gamma \tag{2.24}$$

The problem is then written as: find $\mathbf{u} \in \mathbf{K}$ such that Equation 2.22 is true for all $\mathbf{v} \in \mathbf{K}$ with

$$\mathbf{K} = \left\{ \mathbf{v} \in \mathbf{V} \mid \left(\mathbf{v}^2 - \overline{\mathbf{v}}^1\right) \cdot \overline{\mathbf{n}}^1 + g_0 \geq 0 \text{ on } \Gamma_c \right\}, \tag{2.25}$$

where $\mathbf{V}$ is the space of test functions.

Combining the equations given above into a boundary condition problem for frictionless static contact requires formulating local momentum equation for each body B^γ, $(\gamma = 1, 2)$ in contact:

$$\mathrm{DIV}\, \mathbf{P}^\gamma + \bar{\mathbf{f}}^\gamma = \mathbf{0}, \tag{2.26}$$

where $\mathbf{P}^\gamma$ is the first Piola-Kirchhoff stress tensor and $\bar{\mathbf{f}}^\gamma = \rho_0^\gamma \bar{\mathbf{b}}^\gamma$ are the body forces, with the inertia terms neglected. The boundary conditions of the prescribed quatities of the deformation $\bar{\varphi}^\gamma$ and stress fields $\bar{\mathbf{t}}^\gamma$ is formulated as:

$$\varphi^\gamma = \bar{\varphi}^\gamma \quad \text{on} \quad \Gamma_\varphi^\gamma, \tag{2.27}$$

$$\mathbf{t}^\gamma = \bar{\mathbf{t}}^\gamma \quad \text{on} \quad \Gamma_\sigma^\gamma, \tag{2.28}$$

Thus the Kuhn-Tucker-Karush condition for contact can be formulated wherein the boundary conditions above are used with no adhesion stress applied:

$$g_N \geq 0 \quad p_N \leq 0 \quad g_N p_N = 0 \quad \text{on} \quad \Gamma_c. \tag{2.29}$$

Applying Neo-Hookian model for hyperelasticity, where $\boldsymbol{\tau} = \mathbf{P}\mathbf{F}^T$ is the Piola-Kirchoff stress, where $\mathbf{F}$ is the deformation gradient. Consequently, for the two bodies ($\gamma = 1, 2$) the numerical solution of the nonlinear boundary value problem described above (Equation 2.21) can be obtained by the finite element method the general form of which can be written as:

$$\sum_{\gamma=1}^{2} \int_{B^\gamma} \boldsymbol{\tau}^\gamma \cdot \operatorname{grad}\left(\boldsymbol{\eta}^\gamma - \boldsymbol{\varphi}^\gamma\right) dV \geq \sum_{\gamma=1}^{2} \int_{B^\gamma} \bar{\mathbf{f}}^\gamma \cdot \left(\boldsymbol{\eta}^\gamma - \boldsymbol{\varphi}^\gamma\right) dV - \int_{\Gamma_\sigma^\gamma} \bar{\mathbf{t}}^\gamma \cdot \left(\boldsymbol{\eta}^\gamma - \boldsymbol{\varphi}^\gamma\right) dA \tag{2.30}$$

The integration is performed over the volume of the bodies B^γ and the surface Γ_σ^γ. The stress tensor and the gradient operator "grad" are evaluated with respect to the current coordinates. Additionally, the surface traction $\bar{\mathbf{t}}^\gamma$ is applied on the boundary of B^γ and the body force $\bar{\mathbf{f}}^\gamma$ is applied on the volume of B^γ. The Kirchoff stress $\boldsymbol{\tau}^\gamma$ was defined above. The solution to be found can then be defined as the deformation $\left(\varphi^1, \varphi^2\right) \in \mathbf{K}$ such that Equation 2.30 is satisfied for all $\left(\eta^1, \eta^2\right) \in \mathbf{K}$:

$$\mathbf{K} = \left\{ \left(\boldsymbol{\eta}^1, \boldsymbol{\eta}^2\right) \in \mathbf{V} \mid \left[\boldsymbol{\eta}^2 - \hat{\boldsymbol{\eta}}^1\left(\bar{\xi}^1, \overline{\xi^2}\right)\right] \cdot \bar{\mathbf{n}}_1 \geq 0 \right\} \tag{2.31}$$

This formulation above holds for arbitrary constitutive equations but if the problem can described within a hyperelastic framework, the frictionless contact problem can be written as an optimization problem:

$$\Pi = \sum_{\gamma=1}^{2} \Pi^\gamma \longrightarrow MIN \tag{2.32}$$

The energy function Π^γ for one body is given by:

$$\Pi^\gamma = \int_{B^\gamma} W^\gamma(\mathbf{C}) dV - \int_{B^\gamma} \bar{\mathbf{f}}^\gamma \cdot \varphi^\gamma dV - \int_{\Gamma_\sigma^\gamma} \bar{\mathbf{t}}^\gamma \cdot \varphi^\gamma dA, \tag{2.33}$$

where $W^\gamma(\mathbf{C})$ is the strain energy function of the body.

Turning to the enforcement of contact constraints, several approaches exist for applying these constraints in a variational form. The primary methods used in the finite element method (FEM) are the Lagrange multiplier and penalty methods. The Lagrange multiplier approach introduces additional variables to enforce contact constraints exactly by incorporating them into the system of equations, thereby preventing penetration between contacting surfaces in a strict sense. Alternatively, the penalty method enforces contact constraints approximately by introducing a penalty term into the system's potential energy. This term generates a force proportional to the penetration depth, discouraging interpenetration while allowing for controlled constraint violation. In general, the Lagrange multiplier method provides superior accuracy for resolving contact problems but incurs a high computational cost due to the introduction of additional primal variables. In contrast, the penalty method offers greater computational efficiency but, due to its approximate nature, may lead to inaccuracies and instability [32].

In general the inequality to be solved with different contact conditions can be found by rewritting Equation 2.30 as:

$$\sum_{\gamma=1}^{2}\left\{\int_{B^\gamma}\boldsymbol{\tau}^\gamma\cdot\operatorname{grad}\boldsymbol{\eta}^\gamma dV-\int_{B^\gamma}\bar{\mathbf{f}}^\gamma\cdot\boldsymbol{\eta}^\gamma dV-\int_{\Gamma_\sigma{}^\gamma}\bar{\mathbf{t}}^\gamma\cdot\boldsymbol{\eta}^\gamma dA\right\}+C_c=0, \tag{2.34}$$

where C_c is the contact condition.

2.4.2. Lagrange multiplier methods

The method introduces additional variables, called Lagrange multipliers, to incorporate the constraints into the optimization problem. These multipliers can be interpreted as the contact forces acting between the bodies. By solving a system of equations that includes the original function, the constraints, and the Lagrange multipliers, the deformation of the bodies and the contact forces are simultaneously found.

The Lagrange multiplier method technique adds Lagrange multipliers as additional constraints to the weak form of the problem. The contact contribution Π_c is then formulated as:

$$\Pi_c^{LM}=\int_{\Gamma_c}\left(\lambda_N g_N+\boldsymbol{\lambda}_T\cdot\mathbf{g}_T\right)dA, \tag{2.35}$$

where $\boldsymbol{\lambda}_N$ and $\boldsymbol{\lambda}_T$ are the normal and tangential Lagrange multipliers, whereas $\mathbf{g}_N$ and $\mathbf{g}_T$ are the normal and tangential gap functions. The variation of Π_c is taken to obtain contact constraint formulation C_c^{LM} as used in Equation 2.34:

$$C_c^{LM}=\int_{\Gamma_c}\left(\lambda_N\delta g_N+\boldsymbol{\lambda}_T\cdot\delta\mathbf{g}_T\right)dA+\int_{\Gamma_c}\left(\delta\lambda_N g_N+\delta\boldsymbol{\lambda}_T\cdot\mathbf{g}_T\right)dA \tag{2.36}$$

In the expression above the first term corresponds to virtual work of the Lagrange multipliers along the variation of the gap functions. The second term corresponds to the enforcement of the constraints.

The additional contact contribution terms Π_c or C_c^{LM} can then be used to obtain a solution of the finite elements problem as shown in Figure 2.13. In this simple case the Π_{min} represents the minimum of the potential energy of the system which would be the solution of the system without contact. However in case of a contact problem the gap functions g creates a new space of admissible solutions as illustrated by Π_{min}^c in Figure 2.13.

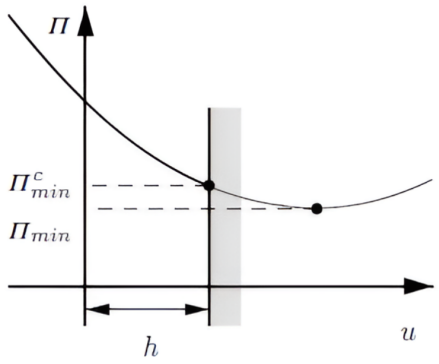

Figure 2.13: Solutions of a simple system governed by a variationaly inequality [29]

One of the key advantages of the Lagrange multiplier method is that it enforces the non-penetration condition exactly, unlike penalty methods which rely on approximations. This leads to more accurate solutions, especially in situations where high precision is required. However, the Lagrange multiplier method also increases the complexity of the problem, as it introduces additional unknowns that need to be solved - the Lagrange multipiers. This can lead to higher computational costs compared to penalty methods. This in addition to the higher implementation complexity when compared to Contact Penalty method especially with regards to parallelization [33] creates a need to examine other methods.

2.4.3. Penalty methods

The penalty method attempts to approximate the results found by the Lagrange method by permitting penetration between the bodies and introducing a penalty force to discourage it. The penalty force is dependent on a contact penalty factor ϵ and to degree of violation of contact conditions. This results in a solution that is easy to implement and with lower computational cost than the Lagrange multiplier method and thus it is the most widely used method [29].
Similarily to the Lagrange multiplier method, within penalty contact framework the constrain condition (Equation 2.34) can be formulated as follows:

$$\Pi_c^P = \frac{1}{2}\int_{\Gamma_c} \left(\epsilon_N \left(g_N^-\right)^2 + \epsilon_T \mathbf{g}_T \cdot \mathbf{g}_T\right) dA, \quad \epsilon_N, \epsilon_T > 0, \tag{2.37}$$

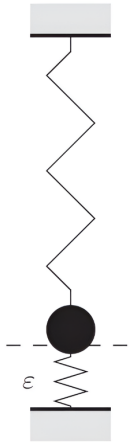

Figure 2.14: Spring system where ε is the contact penalty factor [29]

where ϵ_N and ϵ_T are the normal and tangential penalty parameters. This formulation allows the implementation of the penalty method in the finite element method in a variational context. However, it must be noted that the penalty method can be applied directly as a forcing term in the based solely on the displacement field $\boldsymbol{f} = \epsilon c(u)$ which can also be written as an energy term $\frac{1}{2}\epsilon\left[c(u)\right]^2$. To closer examine some properties of the penalty contact approach consider a simpler spring system as shown in Figure 2.14 energy of which can be written as:

$$\Pi(u) = \frac{1}{2}ku^2 - mgu + \frac{1}{2}\epsilon[c(u)]^2 \quad \text{with } \epsilon > 0. \tag{2.38}$$

The variation of the energy equation yields:

$$ku\delta u - mg\delta u - \epsilon c(u)\delta u = 0. \tag{2.39}$$

Finding the solution of this problem and rewriting it for the penetration $c(u)$ yields:

$$c(u) = h - u = \frac{kh - mg}{k + \epsilon}, \tag{2.40}$$

and the reaction force R_N as:

$$R_N = \lambda = \epsilon c(u) = \frac{\epsilon}{k + \epsilon}(kh - mg). \tag{2.41}$$

Since $mg \geq kh$ in the presence of contact, Equation 2.40 implies that the point mass penetrates the rigid support, which is physically equivalent to a compression of the spring, as illustrated in Figure 2.14. It can be seen from Equation 2.40 that the extent of penetration depends on the penalty parameter. Furthermore, the constraint equation is satisfied only in the limit as $\epsilon \to \infty$, leading to $c(u) \to 0$. Consequently, within the penalty method, two limiting cases can be identified:

1. Case when $\epsilon \to \infty$ that approaches the correct solution but the reaction force R_N approaches infinity thus resulting in unstable numerical solutions.
2. Case when $\epsilon \to 0$ that results in a solution that leads to penetration that is not physically correct.

Consequently, an issue arrises with the choice of the value of the penalty parameter ϵ which involves balancing the trade-off between the accuracy of the solution and the stability of the numerical solution. The method is further comlplicated by the fact suitable values for the penalty parameter depend on the specific problem and often require a posteriori analysis.

2.5. Conclusion

To summarize the literature review, key finding and their role within the context of this work are presented:

- **Lattice metamaterials:** Lattice-based metamaterials, particularly nanoarchitected lattices, have demonstrated remarkable mechanical properties, including high stiffness-to-weight and strength-to-weight ratios, which are advantageous in aerospace applications [1, 2, 7]. Such materials, characterized by structured truss lattice geometries, exhibit unique mechanical responses due to their cellular architecture. The mechanical behavior of these materials is significantly influenced by their relative density and geometry, impacting their capability to absorb and dissipate energy efficiently under dynamic loading conditions. Recent advances in additive manufacturing technologies, such as two-photon lithography, have enabled precise fabrication at micro- and nano-scales, expanding the application possibilities of these architected materials [9].
- **Impact dynamics:** Understanding impact dynamics is crucial for evaluating and optimizing the performance of lattice metamaterials under dynamic loading. Studies have distinguished between various impact regimes, including elastic impacts, particle capture, penetration, and bounce-back [1, 2]. Experimental analyses indicate that nanoarchitected lattices outperform traditional materials like Kevlar in terms of specific energy dissipation, particularly under high-velocity impacts [1]. Dynamic loading introduces additional complexities such as strain-rate dependency and the development of compaction waves, significantly influencing energy absorption and material response [19].
- **Beam/fracture formulations:** Finite element modeling of metamaterial impact here employs geometrically exact Kirchhoff-Love beam formulations, capturing large deformations without shear effects, making them ideal for slender beam structures typical in lattice metamaterials. Fracture mechanics within these models is frequently represented using cohesive zone models (CZMs), where fracture propagation is governed by cohesive laws that dictate traction-separation relationships. The integration of Discontinuous Galerkin methods has enhanced the accuracy and flexibility in modeling fracture and discontinuities, critical for predicting energy dissipation and fracture patterns observed experimentally.
- **Contact formulations:** Contact mechanics significantly influences the accuracy of simulations involving lattice metamaterial impacts. Penalty-based contact formulations are extensively used due to their computational efficiency, enabling simulations of complex contact interactions typical in lattice metamaterials under impact loading. This approach simplifies the enforcement of non-penetration constraints, trading off some accuracy for speed, essential for large-scale computational simulations. Alternative methods, like the Lagrange multiplier method, provide more precise constraint enforcement but at a higher computational cost, often making penalty methods more practical for extensive parametric studies and real-world application scenarios [29].

2.5.1. Research gaps

In order to gain complete understanding and thus to fully unveil the prosimising prospects of lattice metamaterials all aspects of their behaviour and properties have to be examined, including their impact behaviour. Several works have shown the promising properties of lattice metamaterials and of the tools that has been used to understand them has been finite element modelling. Unfortunately, developing effective computational tools can be very expensive, consequently, developing a simplified model can

allow to gain crucial insights about what further developments are required. In this work a model that ommits variety of phenomena is compared to other models and experimental work, thus attempting to understand what are the key challenges in developing more advanced models and what are they key physical phenomena that have to be taken into account.

3
Methodology

This chapter describes the methodology used for the numerical simulations of the impact of a rigid body on a beam lattice. The chapter is structured as follows: Section 3.1 provides an overview of the methodology used in this work, Section 3.2 presents the governing equations of a geometrically exact Kirchoff beam Section 3.3 describes the cohesive zone model used for fracture in beams, Section 3.4 outlines the application of fracture to the computational framework, Section 3.5 describes the space-time discretization used in this work, Section 3.6 presents the penalty method used for contact modeling, Section 3.7 briefly describes the parallelization strategy used in this work and Section 3.8 provides an overview of the Summit framework used for the simulations anderson.

3.1. Overview

This thesis investigates the impact of a rigid body on a beam lattice structure using an explicit dynamic solver. In this section an overview of the methods used to simulate the impact is provided. The beam lattice structure is modeled in a finite element model using beam elements. Each of the struts consists of multiple beam elements the number of which can be adjusted with the struts being connected with rigid joints. The impactor is modelled using a rigid sphere with a predefined initial velocity, radius and mass density. The impactor is set to collide with the beam lattice structure immediately after the simulation starts and the simulation continues up to a predetermined time. This setup is visualized in Figure 3.1.
The beams in the lattice structure are modeled using geometrically exact torsion-free Kirchhoff beam. This type of beam element is well suited for slender beams and is capable of capturing large deformations [34]. Further, in order to be able to model energy absorption during impact it important to model fracture in the beams. This is achieved by employing a cohesive zone model that in this case neglected shear and torsional fracture modes and focused on tensile and bending fracture modes, while employing an unconventional traction-separation law that models cohesive laws with regards to stress resultants. Then to find the governing weak form discontinuous Galerkin method is used which allows to introduce fracture by introducing duplicate nodes at the end of each beam element.

The contact algorithm is implemented using a penalty method. Since the impactor is a rigid sphere checking for contact is done by simply comparing the distance between the center of the sphere and each of the nodes. If contact is detected a penalty force is applied to the node proportional to the penetration depth normal to the surface of the sphere. Finally, in order to make larger simulations feasible the code is parallelized by dividing the calculation to multiple processors.

3.2. Kirchoff beam formulation

In this section the Kirchoff beam formulation as derived by Meier [34] and summarized by Kota [35] is presented.

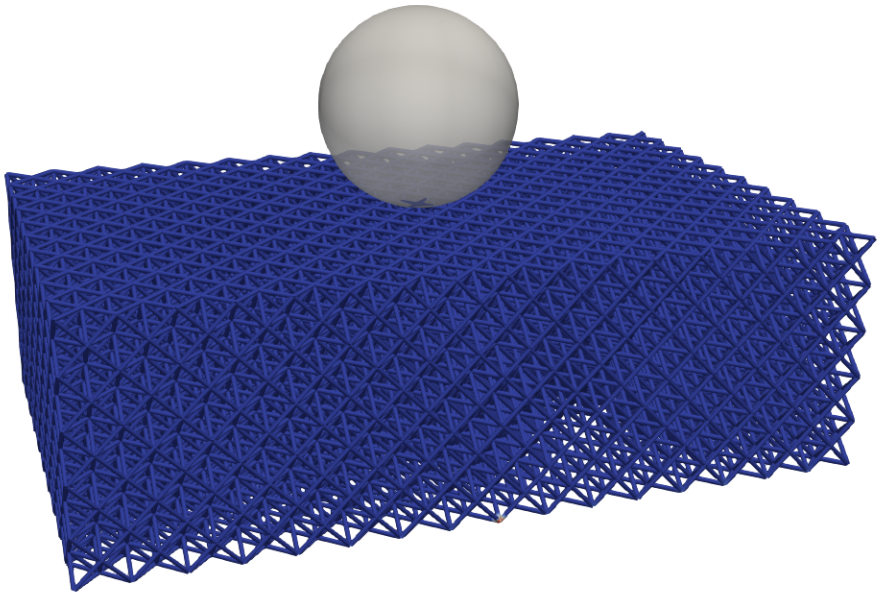

Figure 3.1: The impact simulation setup depicting the rigid impactor colliding with the beam lattice structure.

Kinematics
Following Simo [36], the configuration of the beam is described by the position of its centerline and the orientation of its cross-sections. The beam centerline or in other words the curve traced by the centroids of the cross-sections, is parameterized as $\boldsymbol{r}(s) \in \mathbb{R}^3$, where $s \in [0, L]$ represents the arc-length parameter. The orientation of the cross-sections is expressed using an orthonormal intrinsic frame $\{\boldsymbol{g}_1(s), \boldsymbol{g}_2(s), \boldsymbol{g}_3(s)\}$, as illustrated in Figure 3.2. By convention, $\boldsymbol{g}_1(s)$ is chosen to be orthogonal to the cross-section at s, while $\boldsymbol{g}_2(s)$ and $\boldsymbol{g}_3(s)$ are aligned with its principal axes of inertia. It is important to note that, in general, $\boldsymbol{g}_1(s)$ is not tangent to the centroidal curve $\boldsymbol{r}(s)$.

The deformed configuration of the beam can be expressed in terms of $\boldsymbol{r}$, $\boldsymbol{g_2}$, and $\boldsymbol{g_3}$ with ξ_2 and ξ_3 as coordinates on the beam cross-section in the reference configuration:

$$\boldsymbol{x}(s, \xi_2, \xi_3) = \boldsymbol{r}(s) + \xi_2 \, \boldsymbol{g_2}(s) + \xi_3 \, \boldsymbol{g_3}(s). \tag{3.1}$$

For simplicity, it is often assumed that the beam is initially straight in its reference configuration, allowing the intrinsic frame in this configuration to be chosen as a fixed orthonormal basis $\{\boldsymbol{E}_1, \boldsymbol{E}_2, \boldsymbol{E}_3\}$ of $\mathbb{R}^3$, although this assumption is not fundamental and can be relaxed, as discussed in [**simo1993analysis**]. Since the vector basis $\{\boldsymbol{g}_i(s)\}$ remains orthonormal at every cross-section s, there exists a rotation tensor $\boldsymbol{\Lambda}(s)$ such that:

$$\boldsymbol{g}_i(s) = \boldsymbol{\Lambda}(s)\boldsymbol{E}_i, \quad i = 1, 2, 3. \tag{3.2}$$

Kinematically admissible variations of $\boldsymbol{r}$ and $\boldsymbol{g}_i$ are denoted with $\boldsymbol{\delta r}$ and $\boldsymbol{\delta g}_i$. As a direct consequence of Equation 3.2 kinematically admissible variations of $\boldsymbol{g}_i$ can be written as:

$$\boldsymbol{\delta g}_i(s) = \boldsymbol{\delta \Lambda}(s)\boldsymbol{\Lambda}^T(s)\boldsymbol{g}_i(s). \tag{3.3}$$

Due to tensor $(\boldsymbol{\delta \Lambda})\,\boldsymbol{\Lambda}^T$ being skew-symmetric, Equation 3.3 can be rewritten with $\boldsymbol{\delta \theta}$ as the axial vector of $(\boldsymbol{\delta \Lambda})\,\boldsymbol{\Lambda}^T$ that is also referred to as the *spin vector*:

$$\boldsymbol{\delta g}_i(s) = \boldsymbol{\delta \theta}(s) \times \boldsymbol{g}_i(s), \tag{3.4}$$

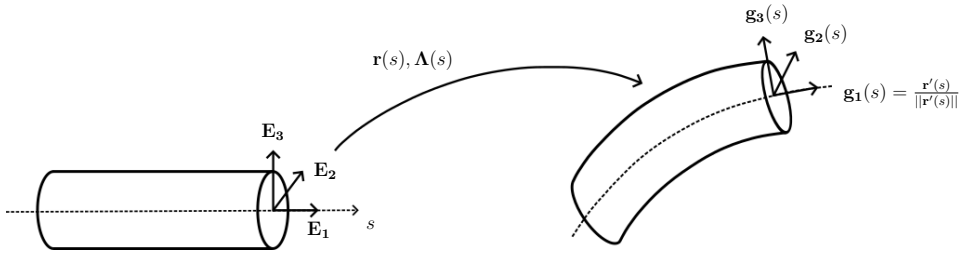

Figure 3.2: Kinematics of a geometrically exact Kirchhoff beam with circular cross-section. The beam configuration is characterized by the line of centroids $\boldsymbol{r}(s)$ and by the orthonormal *intrinsic* frame $\{\boldsymbol{g_1}(s), \boldsymbol{g_2}(s), \boldsymbol{g_3}(s)\}$. The Kirchhoff constraint enforces that $\boldsymbol{g_1}(s)$ be tangent to the line of centroids, or that $\boldsymbol{g_1}(s) = \frac{\boldsymbol{r}'(s)}{||\boldsymbol{r}'(s)||}$ [35].

Under the hypothesis of negligible shear strains, which is a well-accepted assumption in the case of slender beams [37], $\boldsymbol{\delta\theta}$ is not independent of $\boldsymbol{\delta r'}$. Furthermore, a relation between $\boldsymbol{\delta\theta}$ and $\boldsymbol{\delta r'}$ is found by kinematically enforcing that the beam centerline remain perpendicular to the cross-sections during the deformation (Kirchhoff constraint) as shown here:

$$\boldsymbol{g_1}(s) = \frac{\boldsymbol{r}'(s)}{||\boldsymbol{r}'(s)||}, \tag{3.5}$$

where the derivatives are with respect to the arc-length parameter. Combining Equation 3.5 and Equation 3.4, we obtain:

$$\boldsymbol{\delta\theta}(s) = \frac{\boldsymbol{r}'(s) \times \boldsymbol{\delta r}'(s)}{||\boldsymbol{r}'(s)||^2} + \frac{\boldsymbol{r}'(s)}{||\boldsymbol{r}'(s)||}\delta\alpha, \tag{3.6}$$

that yields the kinematically admissible variations of rotations $\boldsymbol{\delta\theta}$ in terms of the kinematically admissible variations of the centerline tangents $\boldsymbol{\delta r'}$ and the tangential component of the spin vector:

$$\delta\alpha(s) := \boldsymbol{\delta\theta}(s) \cdot \frac{\boldsymbol{r}'(s)}{||\boldsymbol{r}'(s)||}. \tag{3.7}$$

where $\delta\alpha$ represents the kinematically admissible variation of the total twist angle. In this work, we limit our attention to the simpler torsion-free formulation and, following [38], the degrees of freedom representing the torsional deformation modes are neglected, resulting in:

$$\boldsymbol{\delta\theta}(s) = \boldsymbol{\delta\theta}_\perp(s) := \frac{\boldsymbol{r}'(s) \times \boldsymbol{\delta r}'(s)}{||\boldsymbol{r}'(s)||^2}. \tag{3.8}$$

A comprehensive discussion on the conditions under which a torsion-free beam formulation is appropriate is available here [34] .

Balance of linear and angular momentum

Integrating the linear and angular momentum balance equations from the 3D continuum theory over the cross-section of the beam allows to then obtain the governing equations of the beam. For a detailed derivation view Simo [36] for a detailed derivation. The final momentum balance equations are presented here:

$$\boldsymbol{f}' + \tilde{\boldsymbol{f}} = \rho A \ddot{\boldsymbol{r}}, \tag{3.9}$$

$$\boldsymbol{m}' + \boldsymbol{r}' \times \boldsymbol{f} + \tilde{\boldsymbol{m}} = \boldsymbol{I_\rho}\dot{\boldsymbol{\omega}} + \boldsymbol{\omega} \times (\boldsymbol{I_\rho}\boldsymbol{\omega}). \tag{3.10}$$

In the equation above the prime derivative refers to arc-length and the dot derivatives refer to material time derivative. Symbols ρ, A, and $\boldsymbol{I_\rho}$ refer to mass density, area of cross-section, and spatial inertia tensor of the beam. $\boldsymbol{\omega}$ is the axial vector corresponding to the the skew-symmetric angular velocity tensor $\dot{\boldsymbol{\Lambda}}\boldsymbol{\Lambda}^T$, while $\boldsymbol{f}(s,t)$ and $\boldsymbol{m}(s,t)$ are the internal force and moment stress resultants expressed with $\boldsymbol{P}$ as the Piola-Kirchhoff stress tensor and $\tilde{\boldsymbol{f}}$ and $\tilde{\boldsymbol{m}}$ as the external distributed forces and moments per unit referential arc-length.

$$f = \int_A \boldsymbol{P}\boldsymbol{E_1}\,\mathrm{d}A, \boldsymbol{m} = \int_A (\boldsymbol{x}-\boldsymbol{r})\times\boldsymbol{P}\boldsymbol{E_1}\,\mathrm{d}A. \tag{3.11}$$

By using the notation as seen in Equation 3.12, forces f, $\tilde{f}$ can be decomposed into axial $f_{||}$, $\tilde{f}_{||}$ and shear $f_{\perp}$, $\tilde{f}_{\perp}$ forces. Similarly the moments $\boldsymbol{m}$, $\tilde{\boldsymbol{m}}$ can be split into bending $\boldsymbol{m}_{\perp}$, $\tilde{\boldsymbol{m}}_{\perp}$ and torsional $\boldsymbol{m}_{||}$, $\tilde{\boldsymbol{m}}_{||}$ moments.

$$\boldsymbol{a}_{||} := \left(\boldsymbol{a}\cdot\frac{\boldsymbol{r}'}{||\boldsymbol{r}'||}\right)\frac{\boldsymbol{r}'}{||\boldsymbol{r}'||}, \qquad \boldsymbol{a}_{\perp} := \boldsymbol{a}-\boldsymbol{a}_{||}. \tag{3.12}$$

Using the assumption that the right-hand side of Equation 3.10 or in other words the rotational inertia can be neglected [34], equation for internal shear forces as a function of the bending moments can be obtained by performing the cross product of Equation 3.10 with $\boldsymbol{r}'$:

$$f_{\perp} = \frac{\boldsymbol{r}'}{||\boldsymbol{r}'||^2}\times\left(\boldsymbol{m}'_{\perp}+\tilde{\boldsymbol{m}}_{\perp}\right) \tag{3.13}$$

Combining Equation 3.13 and Equation Equation 3.9 yields:

$$f'_{||} + \left[\frac{\boldsymbol{r}'}{||\boldsymbol{r}'||^2}\times\left(\boldsymbol{m}'_{\perp}+\tilde{\boldsymbol{m}}_{\perp}\right)\right]' + \tilde{f} = \rho A\ddot{\boldsymbol{r}}. \tag{3.14}$$

It should be noted that in this derivation Equation 3.14 is equivalent to the original system of governing equations Equation 3.9 and Equation 3.10. This is a consequence of the simplified torsion-free model meaning that Equation 3.13 is equivalent to Equation 3.10.

Constitutive equations
By assuming isotropic beams with circular cross-section and hyperelastic material behaviour constitutive equations can be used to relate axial strain ($\epsilon = ||\boldsymbol{r}'|| - 1$) and curvature $\boldsymbol{\kappa} = \frac{\boldsymbol{r}'\times\boldsymbol{r}''}{||\boldsymbol{r}'||^2}$ to axial forces and bending moments as [38]:

$$\boldsymbol{f}_{||} = EA\epsilon\frac{\boldsymbol{r}'}{||\boldsymbol{r}'||}, \qquad \boldsymbol{m}_{\perp} = EI\boldsymbol{\kappa}, \tag{3.15}$$

where E, A and I are the Young's modulus, cross-sectional area and moment of inertia of the beam, respectively.
An assumption is made with regards to the constitutive relations Equation 3.15 of small strains. However, it should be noted that the framework presented here can be still be extended to include additional material properties such as plasticity, viscoelasticity [39] or elasto-visco-plasticity [**weeger:2022**] to model fracture in various material types.

3.3. Cohesive zone method

Cohesive zone approach for fracture in beams
Beams exhibit several modes of fracture, including tension, shear, torsion, and bending as shown in Figure 3.3. In this work, the focus is on tensile and bending fracture modes in slender beams, while shear and torsional fracture modes are neglected.
To model fracture behaviour cohesive zone model is used. In this framework, cohesive zone models describe crack evolution using a traction-separation law, assuming that fracture processes take place within a finite-length region ahead of the crack tip, known as the cohesive zone. Rather than employing conventional traction-separation laws commonly used in cohesive zone models [40], here cohesive laws are defined in terms of stress resultants, as detailed in [24, 25]. Consistent with standard practice in cohesive zone modeling, it is assumed that cohesive forces and moments depend exclusively on the kinematic jumps near the crack tip.

First, cohesive boundaries at interfaces of adjacent elements of the beam are introduced, where discontinuities in the kinematic fields can occur. At these interfaces the axial $\Delta_{||}$ and bending $\boldsymbol{\Theta}$ kinematic

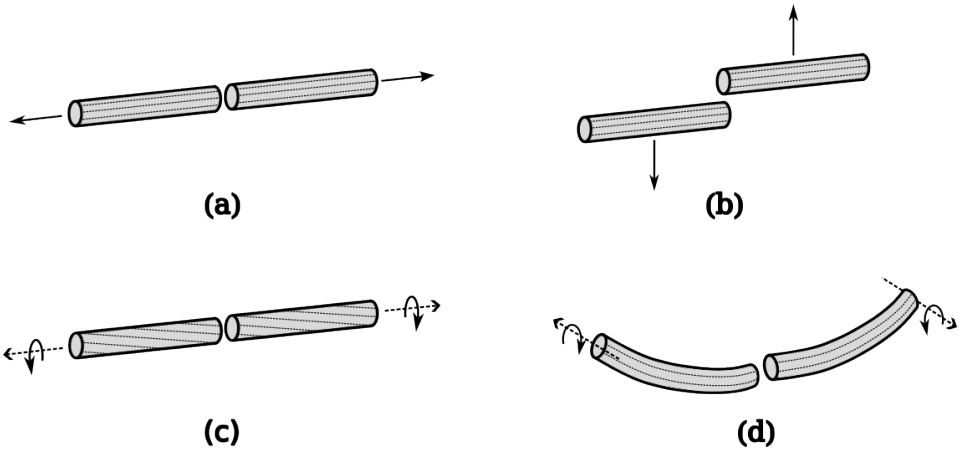

Figure 3.3: The fracture modes of beams: (a) tension, (b) shear, (c) torsion and (d) bending [35].

jumps are defined with $\hat{\boldsymbol{n}}_{\boldsymbol{coh}}$ as the unit normal to the cohesive boundary in the current configuration as:

$$\begin{aligned} \Delta_{||} &= [\![\boldsymbol{r}]\!] \cdot \hat{\boldsymbol{n}}_{\boldsymbol{coh}} \\ \boldsymbol{\Theta} &= [\![\boldsymbol{g_1}]\!], \end{aligned} \tag{3.16}$$

and

$$\hat{\boldsymbol{n}}_{\boldsymbol{coh}} = \frac{\langle \boldsymbol{g_1} \rangle}{||\langle \boldsymbol{g_1} \rangle||}. \tag{3.17}$$

where the bracket notation is used to represent the jump and average of the field $\bullet$ at any arbitrary point $s = a \in (0, L)$ as:

$$[\![\bullet]\!]\Big|_{s=a} := \lim_{s \to a^+} \bullet - \lim_{s \to a^-} \bullet \tag{3.18}$$

$$\langle \bullet \rangle\Big|_{s=a} := \frac{1}{2} \left(\lim_{s \to a^+} \bullet + \lim_{s \to a^-} \bullet \right) \tag{3.19}$$

It should be noted that the component normal to the cohesive boundary of $\boldsymbol{\Theta}$, is zero as $\boldsymbol{\Theta} \cdot \hat{\boldsymbol{n}}_{\boldsymbol{coh}} = 0$ holds by construction.

Scalar effective separation Δ is defined to enable mixed-mode fracture under tension and bending. Using variables R as the radius of the beam and α as a mode-mixity parameterit it is defined as:

$$\Delta = \sqrt{\{\Delta_{||}\}^2 + \left(\alpha R ||\boldsymbol{\Theta}||\right)^2}, \tag{3.20}$$

In the equation above, $\{\cdot\} = \max(\cdot\,, 0)$ denotes the Macaulay operator. Further, the following cohesive axial forces and cohesive bending moments resisting the opening of cracks in the beam are introduced:

$$\begin{aligned} \boldsymbol{f}_{\boldsymbol{coh},||} &= f_{coh}(\Delta, \boldsymbol{q}) \, \frac{\{\Delta_{||}\}}{\Delta} \, \hat{\boldsymbol{n}}_{\boldsymbol{coh}}, \\ \boldsymbol{m}_{\boldsymbol{coh},\perp} &= \alpha^2 \, f_{coh}(\Delta, \boldsymbol{q}) \, \frac{R^2}{\Delta} \, \boldsymbol{\Theta}, \end{aligned} \tag{3.21}$$

where effective cohesive force f_{coh} is defined as a scalar function of the effective separation Δ and a set of internal variables $\boldsymbol{q}$. The function $f_{coh}(\Delta, \boldsymbol{q})$ can be adjusted to represent different constitutive fracture behaviors, such as brittle, quasi-brittle, or ductile responses. In this formulation, cohesive axial forces and cohesive bending moments are assumed to decay linearly with Δ, as depicted in Figure 3.4.

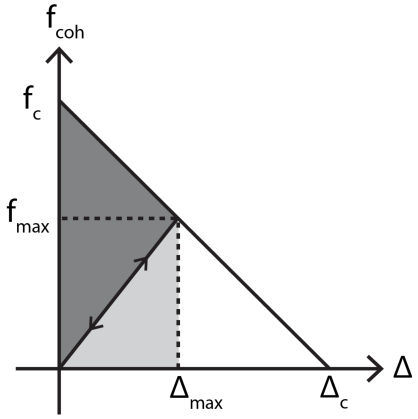

Figure 3.4: The force-separation cohesive law defines a linear reduction of the scalar effective cohesive force f_{coh} with the scalar effective separation Δ, decreasing from a critical value f_c to zero. Irreversibility is incorporated by introducing a history variable Δ_{max}, which tracks the maximum effective separation reached. During unloading, the response follows a path back to the origin, while reloading proceeds along the same unloading trajectory. The total area under the force-separation curve corresponds to the effective fracture energy of the material, whereas the black and grey regions at any given $\Delta = \Delta_{max}$ represent the dissipated and maximum recoverable energies at the cohesive boundary. Complete fracture occurs when $\Delta \geq \Delta_c$ [35].

To ensure irreversibility, a history internal variable Δ_{max} is introduced, following standard cohesive zone modeling practices.
During the loading stage the cohesive force is given as:

$$f_{coh}(\Delta, \Delta_{max}) = \left(1 - \frac{\Delta}{\Delta_c}\right) f_c \quad \text{for} \quad \Delta \geq \Delta_{max}, \tag{3.22}$$

with Δ_{max} ias the maximum effective separation in the entire loading history, $\Delta_c = 2G_c/\sigma_c$ as the effective separation at which complete decohesion occurs, and G_c as the effective fracture energy. Meanwhile in the unloading and reloading stage, the force is set as:

$$f_{coh}(\Delta, \Delta_{max}) = \frac{\Delta}{\Delta_{max}} f_{max} \quad \text{for} \quad \Delta < \Delta_{max}, \tag{3.23}$$

where f_{max} is the effective cohesive force at Δ_{max}.

The initiation of the cohesive laws happens at the inter-element boundaries of the beam once the fracture initiation criterion is met:

$$f_{eq}(\langle \boldsymbol{f} \rangle, \langle \boldsymbol{m}_\perp \rangle) \geq f_c, \tag{3.24}$$

where $f_c = \sigma_c A$ is the critical effective cohesive force expressed in terms of the material's cohesive strength σ_c, and f_{eq} is an equivalent force given by the scalar:

$$f_{eq}(\boldsymbol{f}, \boldsymbol{m}_\perp) = \sqrt{\{\boldsymbol{f} \cdot \hat{\boldsymbol{n}}_{coh}\}^2 + \left\| \frac{\boldsymbol{m}_\perp}{\alpha R} \right\|^2}. \tag{3.25}$$

3.4. Computational framework for fracture in geometrically exact slender beams

This subsection presents the derivation of the discontinuous Galerkin / cohesive zone model approach for fracture in geometrically exact slender beams. The derivation begins with the discontinuous Galerkin weak formulation of the beam governing equations outlined in Section 3.2. Subsequently, the weak formulation of the discontinuous Galerkin / cohesive zone model is introduced, followed by its spatial and temporal discretization.

Derivation of the discontinuous Galerkin weak form

The space discretization Ω_h of the straight, undeformed beam Ω consists of segments $\Omega_e = (s_0^e, s_1^e)$ for $e = 1, ..., E$, such that $\Omega_h = \bigcup_{e=1}^{E} \overline{\Omega}_e$, as illustrated schematically in Figure 3.5. The boundary of the beam is denoted as $\partial\Omega_h = \{0, L\}$, with the external normal n_e defined as $n_e = 1$ at $s = L$ and $n_e = -1$ at $s = 0$. Additionally, the Neumann portions of $\partial\Omega_h$, where forces $\bar{\boldsymbol{f}}$ and moments $\bar{\boldsymbol{m}}_\perp$ are applied, are designated as $\partial_{N_f}\Omega_h$ and $\partial_{N_m}\Omega_h$, respectively.

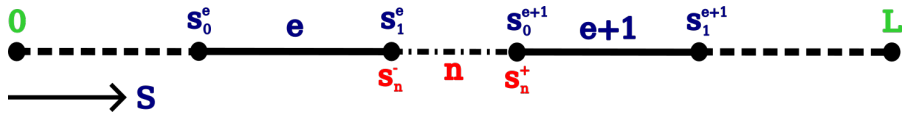

Figure 3.5: The discontinuous Galerkin discretization of the straight, undeformed beam with duplicated internal nodes enabling discontinuities at the element interfaces s_n for $n = 1, ..., E-1$ thus allowing fractures to be formed on the interfaces [35].

The derivation of the discontinuous Galerkin weak form of Equation 3.14 begins by multiplying it with $\boldsymbol{\delta r}$, integrating over the individual subdomains Ω_e for $e = 1, ..., E$, and applying integration by parts with the Neumann boundary condition applied $\bar{\boldsymbol{f}} = n_e \boldsymbol{f}$ on $\partial_{N_f}\Omega_h$ and notation $\bullet\big|_a$ is used in Equation 3.26 to denote $\bullet$ evaluated at $s = a$:

$$\begin{aligned} -\sum_{e=1}^{E}\int_{\Omega_e} \boldsymbol{f}_{\parallel}\cdot\boldsymbol{\delta r}'\,ds - \sum_{e=1}^{E}\int_{\Omega_e} \boldsymbol{f}_{\perp}\cdot\boldsymbol{\delta r}'\,ds - \sum_{n=1}^{E-1}[\![\boldsymbol{f}\cdot\boldsymbol{\delta r}]\!]\Big|_{s_n} + (\bar{\boldsymbol{f}}\cdot\boldsymbol{\delta r})\Big|_{\partial_{N_f}\Omega_h} \\ + \sum_{e=1}^{E}\int_{\Omega_e}\tilde{\boldsymbol{f}}\cdot\boldsymbol{\delta r}\,ds = \sum_{e=1}^{E}\int_{\Omega_e}\rho A\ddot{\boldsymbol{r}}\cdot\boldsymbol{\delta r}\,ds, \end{aligned} \tag{3.26}$$

By employing the identity $[\![\boldsymbol{a}\cdot\boldsymbol{b}]\!] = \langle\boldsymbol{a}\rangle\cdot[\![\boldsymbol{b}]\!] + [\![\boldsymbol{a}]\!]\cdot\langle\boldsymbol{b}\rangle$, the discontinuous jump term in Equation 3.26 can be rewritten as:

$$\sum_{n=1}^{E-1}[\![\boldsymbol{f}\cdot\boldsymbol{\delta r}]\!]\Big|_{s_n} = \sum_{n=1}^{E-1}\Big[\!\Big[\langle\boldsymbol{f}\rangle\cdot[\![\boldsymbol{\delta r}]\!]\Big]\!\Big]\Big|_{s_n} + \sum_{n=1}^{E-1}\Big[\!\Big[[\![\boldsymbol{f}]\!]\cdot\langle\boldsymbol{\delta r}\rangle\Big]\!\Big]\Big|_{s_n}. \tag{3.27}$$

Furthermore, applying vector identity $\boldsymbol{a}\cdot(\boldsymbol{b}\times\boldsymbol{c}) = \boldsymbol{c}\cdot(\boldsymbol{a}\times\boldsymbol{b})$, on Equation 3.13 enables rewriting of the second term of Equation 3.26 as:

$$\begin{aligned} -\sum_{e=1}^{E}\int_{\Omega_e}\boldsymbol{f}_{\perp}\cdot\boldsymbol{\delta r}'\,ds &= \sum_{e=1}^{E}\int_{\Omega_e}(\boldsymbol{m}_{\perp}'+\tilde{\boldsymbol{m}}_{\perp})\cdot\frac{\boldsymbol{r}'\times\boldsymbol{\delta r}'}{||\boldsymbol{r}'||^2}\,ds \\ &= \sum_{e=1}^{E}\int_{\Omega_e}(\boldsymbol{m}_{\perp}'+\tilde{\boldsymbol{m}}_{\perp})\cdot\boldsymbol{\delta\theta}_{\perp}\,ds. \end{aligned} \tag{3.28}$$

The kinematically admissible variation $\boldsymbol{\delta\theta}_\perp$ in Equation 3.8 naturally arises as the work conjugate of the bending moments. For clarity in the following derivation, the subscript in $\boldsymbol{\delta\theta}_\perp$ is omitted, and the notation $\boldsymbol{\delta\theta}$ is used instead. The right-hand side of Equation 3.28 can subsequently be integrated by parts and using again the identity $[\![\boldsymbol{a}\cdot\boldsymbol{b}]\!] = \langle\boldsymbol{a}\rangle\cdot[\![\boldsymbol{b}]\!] + [\![\boldsymbol{a}]\!]\cdot\langle\boldsymbol{b}\rangle$, resulting in:

$$\begin{aligned} \sum_{e=1}^{E}\int_{\Omega_e}(\boldsymbol{m}_{\perp}'+\tilde{\boldsymbol{m}}_{\perp})\cdot\boldsymbol{\delta\theta}\,ds &= \sum_{e=1}^{E}\int_{\Omega_e}\tilde{\boldsymbol{m}}_{\perp}\cdot\boldsymbol{\delta\theta}\,ds - \sum_{e=1}^{E}\int_{\Omega_e}\boldsymbol{m}_{\perp}\cdot\boldsymbol{\delta\theta}'\,ds \\ &- \sum_{n=1}^{E-1}\Big[\!\Big[\langle\boldsymbol{m}_{\perp}\rangle\cdot[\![\boldsymbol{\delta\theta}]\!]\Big]\!\Big]\Big|_{s_n} - \sum_{n=1}^{E-1}\Big[\!\Big[[\![\boldsymbol{m}_{\perp}]\!]\cdot\langle\boldsymbol{\delta\theta}\rangle\Big]\!\Big]\Big|_{s_n} + (\bar{\boldsymbol{m}}_{\perp}\cdot\boldsymbol{\delta\theta})\Big|_{\partial_{N_m}\Omega_h}, \end{aligned} \tag{3.29}$$

where the Neumann boundary condition $\bar{\boldsymbol{m}}_\perp = n_e\boldsymbol{m}_\perp$ is applied on $\partial_{N_m}\Omega_h$.

Then combining Equation 3.26, Equation 3.27, Equation 3.28, and Equation 3.29, yields:

$$\begin{aligned}
&\sum_{e=1}^{E}\int_{\Omega_e}\rho A\ddot{\boldsymbol{r}}\cdot\boldsymbol{\delta r}\,ds+\sum_{e=1}^{E}\int_{\Omega_e}\boldsymbol{f}_{\shortparallel}\cdot\boldsymbol{\delta r}'\,ds+\sum_{n=1}^{E-1}\Big[\langle\boldsymbol{f}\rangle\cdot[\![\boldsymbol{\delta r}]\!]\Big]\Big|_{s_n}+\sum_{n=1}^{E-1}\Big[[\![\boldsymbol{f}]\!]\cdot\langle\boldsymbol{\delta r}\rangle\Big]\Big|_{s_n}\\
&+\sum_{e=1}^{E}\int_{\Omega_e}\boldsymbol{m}_{\perp}\cdot\boldsymbol{\delta\theta}'\,ds+\sum_{n=1}^{E-1}\Big[\langle\boldsymbol{m}_{\perp}\rangle\cdot[\![\boldsymbol{\delta\theta}]\!]\Big]\Big|_{s_n}+\sum_{n=1}^{E-1}\Big[[\![\boldsymbol{m}_{\perp}]\!]\cdot\langle\boldsymbol{\delta\theta}\rangle\Big]\Big|_{s_n}\\
&=\sum_{e=1}^{E}\int_{\Omega_e}\tilde{\boldsymbol{f}}\cdot\boldsymbol{\delta r}\,ds+\big(\bar{\boldsymbol{f}}\cdot\boldsymbol{\delta r}\big)\Big|_{\partial_{N_f}\Omega_h}+\sum_{e=1}^{E}\int_{\Omega_e}\tilde{\boldsymbol{m}}_{\perp}\cdot\boldsymbol{\delta\theta}\,ds+\big(\bar{\boldsymbol{m}}_{\perp}\cdot\boldsymbol{\delta\theta}\big)\Big|_{\partial_{N_m}\Omega_h},
\end{aligned}\tag{3.30}$$

Since discontinuities in forces $\boldsymbol{f}$ and bending moments $\boldsymbol{m}_{\perp}$ do not require penalization for maintaining the consistency of the numerical scheme, the corresponding terms in Equation 3.30 can be omitted, as discussed in [41, 42]. However, to ensure numerical stability, inter-element compatibility must be enforced in a weak sense. This is achieved using the interior penalty method, following [41, 42]. Consequently, these terms are added to the left-hand side of Equation 3.30:

$$\sum_{n=1}^{E-1}\beta_p\Big[\Big\langle\frac{EA}{h}\Big\rangle[\![\boldsymbol{\delta r}]\!]\cdot[\![\boldsymbol{r}]\!]\Big]\Big|_{s_n}+\sum_{n=1}^{E-1}\beta_t\Big[\Big\langle\frac{EI}{h}\Big\rangle[\![\boldsymbol{\delta g_1}]\!]\cdot[\![\boldsymbol{g_1}]\!]\Big]\Big|_{s_n}.\tag{3.31}$$

As shown in Equation 3.5 it is kinematically enforced that $\boldsymbol{g_1}=\frac{\boldsymbol{r}'}{||\boldsymbol{r}'||}$. Variables $\beta_p>1$ and $\beta_t>1$ are position and tangent jump penalty parameters and h is the element size. Thus by additionally applying the constitutive relations Equation 3.15 stabilized discontinuous Galerkin weak form is found:

$$\begin{aligned}
&\int_{\Omega_h}\rho A\ddot{\boldsymbol{r}}\cdot\boldsymbol{\delta r}\,ds+\int_{\Omega_h}EA\,\varepsilon\,\delta\varepsilon\,ds+\sum_{n=1}^{E-1}\Big[\langle\boldsymbol{f}\rangle\cdot[\![\boldsymbol{\delta r}]\!]\Big]\Big|_{s_n}+\sum_{n=1}^{E-1}\beta_p\Big[\Big\langle\frac{EA}{h}\Big\rangle[\![\boldsymbol{r}]\!]\cdot[\![\boldsymbol{\delta r}]\!]\Big]\Big|_{s_n}\\
&\qquad+\int_{\Omega_h}EI\,\boldsymbol{\kappa}\cdot\boldsymbol{\delta\kappa}\,ds+\sum_{n=1}^{E-1}\Big[\langle\boldsymbol{m}_{\perp}\rangle\cdot[\![\boldsymbol{\delta\theta}]\!]\Big]\Big|_{s_n}+\sum_{n=1}^{E-1}\beta_t\Big[\Big\langle\frac{EI}{h}\Big\rangle[\![\boldsymbol{g_1}]\!]\cdot[\![\boldsymbol{\delta g_1}]\!]\Big]\Big|_{s_n}\\
&=\int_{\Omega_h}\tilde{\boldsymbol{f}}\cdot\boldsymbol{\delta r}\,ds+\big(\bar{\boldsymbol{f}}\cdot\boldsymbol{\delta r}\big)\Big|_{\partial_{N_f}\Omega_h}+\int_{\Omega_h}\tilde{\boldsymbol{m}}_{\perp}\cdot\boldsymbol{\delta\theta}\,ds+\big(\bar{\boldsymbol{m}}_{\perp}\cdot\boldsymbol{\delta\theta}\big)\Big|_{\partial_{N_m}\Omega_h},
\end{aligned}\tag{3.32}$$

The discontinuous Galerkin / cohesive zone model (DG/CZM) weak formulation

A key property of the discountinuous Galerkin model are the discontinuities of positions and tangents between the elements, as outlined in Section 3.4. Before fracture the compatibility of the solution across element boundaries is enabled by the variationally consistent interface. However, upon satisfaction of the fracture criterion Equation 3.24, the interface axial forces and bending moments in Equation 3.32 are replaced with the cohesive axial forces and the cohesive bending moments of Equation 3.21. While, negligible shear strains are assumed and thus shear modes of fracture are not modelled, simultaneously, the component of the interface force term perpendicular to the unit normal of the cohesive boundary in Equation 3.32 is still present until complete interface failure [42]. Two binary parameters α_n and γ_n are defined at each interface n. Before fracture initiation both they are set as $\alpha_n=1$ and $\gamma_n=1$ but after the fracture criterion Equation 3.24 is met alpha is set to $\alpha_n=0$ and similarly gamma is set as $\gamma_n=0$ upon complete decohesion ($\Delta\geq\Delta_c$). Consequently, these variables allow to mathematically distinguish pre-crack formation, pre-fracture and post-fracture behavior. Finally the discontinuous Galerkin / cohesive zone model weak form is given as:

$$
\begin{aligned}
&\int_{\Omega_h} \rho A \ddot{\boldsymbol{r}} \cdot \boldsymbol{\delta r}\, ds + \int_{\Omega_h} EA\, \varepsilon\, \delta\varepsilon\, ds + \sum_{n=1}^{E-1} \alpha_n \Big[\boldsymbol{f}_{DG,||} \cdot [\![\boldsymbol{\delta r}]\!] \Big]\Big|_{s_n} + \sum_{n=1}^{E-1} \gamma_n \Big[\boldsymbol{f}_{DG,\perp} \cdot [\![\boldsymbol{\delta r}]\!] \Big]\Big|_{s_n} \\
&\quad + \sum_{n=1}^{E-1} \alpha_n \left[\beta_p \left\langle \frac{EA}{h} \right\rangle \boldsymbol{c}_{DG,||} \cdot [\![\boldsymbol{\delta r}]\!] \right]\Bigg|_{s_n} + \sum_{n=1}^{E-1} \gamma_n \left[\beta_p \left\langle \frac{EA}{h} \right\rangle \boldsymbol{c}_{DG,\perp} \cdot [\![\boldsymbol{\delta r}]\!] \right]\Bigg|_{s_n} \\
&\quad + \int_{\Omega_h} EI\, \boldsymbol{\kappa} \cdot \boldsymbol{\delta\kappa}\, ds + \sum_{n=1}^{E-1} \alpha_n \Big[\langle \boldsymbol{m}_\perp \rangle \cdot [\![\boldsymbol{\delta\theta}]\!] \Big]\Big|_{s_n} + \sum_{n=1}^{E-1} \alpha_n \left[\beta_t \left\langle \frac{EI}{h} \right\rangle [\![\boldsymbol{g_1}]\!] \cdot [\![\boldsymbol{\delta g_1}]\!] \right]\Bigg|_{s_n} \\
&\quad + \sum_{n=1}^{E-1} (1-\alpha_n) \Big[\boldsymbol{f}_{\boldsymbol{coh},||} \cdot [\![\boldsymbol{\delta r}]\!] \Big]\Big|_{s_n} + \sum_{n=1}^{E-1} (1-\alpha_n) \Big[\boldsymbol{m}_{\boldsymbol{coh},\perp} \cdot [\![\boldsymbol{\delta g_1}]\!] \Big]\Big|_{s_n} \\
&= \int_{\Omega_h} \tilde{\boldsymbol{f}} \cdot \boldsymbol{\delta r}\, ds + \left(\bar{\boldsymbol{f}} \cdot \boldsymbol{\delta r} \right)\Big|_{\partial_{N_f}\Omega_h} + \int_{\Omega_h} \tilde{\boldsymbol{m}}_\perp \cdot \boldsymbol{\delta\theta}\, ds + \left(\bar{\boldsymbol{m}}_\perp \cdot \boldsymbol{\delta\theta} \right)\Big|_{\partial_{N_m}\Omega_h}
\end{aligned}
\tag{3.33}
$$

wherein variables are defined as:

$$
\begin{aligned}
\boldsymbol{f}_{DG,||} &= \left(\langle \boldsymbol{f} \rangle \cdot \hat{\boldsymbol{n}}_{\boldsymbol{coh}} \right) \hat{\boldsymbol{n}}_{\boldsymbol{coh}}, \\
\boldsymbol{f}_{DG,\perp} &= (\boldsymbol{I} - \hat{\boldsymbol{n}}_{\boldsymbol{coh}} \otimes \hat{\boldsymbol{n}}_{\boldsymbol{coh}}) \langle \boldsymbol{f} \rangle, \\
\boldsymbol{c}_{DG,||} &= \left([\![\boldsymbol{r}]\!] \cdot \hat{\boldsymbol{n}}_{\boldsymbol{coh}} \right) \hat{\boldsymbol{n}}_{\boldsymbol{coh}}, \\
\boldsymbol{c}_{DG,\perp} &= (\boldsymbol{I} - \hat{\boldsymbol{n}}_{\boldsymbol{coh}} \otimes \hat{\boldsymbol{n}}_{\boldsymbol{coh}}) [\![\boldsymbol{r}]\!] .
\end{aligned}
$$

3.5. Discretization in space and time

In order for the weak form (Equation 3.33) to be solved numerically, it must be discretized in space and time.

The spatial discretization of $\boldsymbol{r}$ is performed using third-order Hermite polynomials, which have been shown to achieve a convergence order of four in continuous Galerkin settings [22]. The choice of Hermite polynomials over Lagrange polynomials is motivated by the advantage that the arc-length derivative $\boldsymbol{r'}$ at each node is directly available as a primary degree of freedom associated with that node. This property simplifies the computation of terms at element interfaces in Equation 3.32. Consequently, $\boldsymbol{r}$ is discretized as follows:

$$
\boldsymbol{r}(\xi) \approx \sum_{b=1}^{2} N_p^b(\xi) \boldsymbol{p}^b + \frac{L}{2} \sum_{b=1}^{2} N_t^b(\xi) \boldsymbol{t}^b := \sum_{a=1}^{4} N_a(\xi) \boldsymbol{x_a}, \tag{3.34}
$$

where $\boldsymbol{p}^b$ and $\boldsymbol{t}^b$ denote the position and tangent degrees of freedom at the element nodes $b = 1, 2$, respectively. The variable $\xi \in [-1, 1]$ is the parametric coordinate in the reference element, which is mapped to the arc-length coordinate $s \in [0, L]$ via the transformation $s = \frac{L}{2}(1 + \xi)$. The functions N_p^b and N_t^b represent the following shape functions:

$$
\begin{aligned}
N_p^1(\xi) &= \frac{1}{4}(2+\xi)(1-\xi)^2\,; \;\; N_p^2(\xi) = \frac{1}{4}(2-\xi)(1+\xi)^2, \\
N_t^1(\xi) &= \frac{1}{4}(1+\xi)(1-\xi)^2\,; \;\; N_t^2(\xi) = -\frac{1}{4}(1-\xi)(1+\xi)^2.
\end{aligned}
\tag{3.35}
$$

This space discretization results in a semi-discrete system of equations:

$$
\boldsymbol{M_{ab}} \ddot{\boldsymbol{x}}_{\boldsymbol{b}} + \boldsymbol{f_a^{int}} + \boldsymbol{f_{a^\pm}^{jump}} = \boldsymbol{f_a^{ext}}, \tag{3.36}
$$

where the inertial term $\boldsymbol{M}_{ab}\, \ddot{\boldsymbol{x}}_b$, the internal (bulk) force $\boldsymbol{f}_a^{\text{int}}$, the internal (interface) force $\boldsymbol{f}_{a^\pm}^{\text{jump}}$, and the external force $\boldsymbol{f}_a^{\text{ext}}$ are detailed below:

$$\boldsymbol{M_{ab}}\ddot{\boldsymbol{x}}_{\boldsymbol{b}} = \left[\int_{-1}^{1} N_a \rho A N_b \frac{L}{2}\, d\xi\right]\ddot{\boldsymbol{x}}_{\boldsymbol{b}},$$

$$\boldsymbol{f_a^{int}} = \int_{-1}^{1} \left[N_a'(EA\boldsymbol{t_1} + EI\boldsymbol{t_2}) + N_a'' EI \boldsymbol{t_3}\right]\frac{L}{2}\, d\xi,$$

$$\boldsymbol{f_{a^{\pm}}^{jump}} = \pm \sum_{n=1}^{E-1} \alpha_n \left[\left[N_a \boldsymbol{f_{DG,||}}\right] + \left[N_a'\left[\langle \boldsymbol{m_\perp}\rangle \times \boldsymbol{t_4}\right]\right] + \beta_p \left\langle \frac{EA}{h}\right\rangle \left[N_a \boldsymbol{c_{DG,||}}\right] + \beta_t \left\langle \frac{EI}{h}\right\rangle \left[N_a'\, \boldsymbol{t_5}\right]\right]\Bigg|_{s_n} \pm \sum_{n=1}^{E-1} \gamma_n \left[\left[N_a \boldsymbol{f_{DG,\perp}}\right] + \beta_p \left\langle \frac{EA}{h}\right\rangle \left[N_a \boldsymbol{c_{DG,\perp}}\right]\right]\Bigg|_{s_n} \pm \sum_{n=1}^{E-1} (1-\alpha_n)\left[\left[N_a \boldsymbol{f_{coh,||}}\right] + \left[N_a' \boldsymbol{G_1 m_{coh,\perp}}\right]\right]\Bigg|_{s_n},$$

$$\boldsymbol{f_a^{ext}} = \int_{-1}^{1} \left[N_a \tilde{\boldsymbol{f}} + N_a'(\tilde{\boldsymbol{m}}_\perp \times \boldsymbol{t_4})\right]\frac{L}{2}\, d\xi + \left[N_a \bar{\boldsymbol{f}}\,\right]\big|_{\partial_{N_f}\Omega_h} + \left[N_a'(\bar{\boldsymbol{m}}_\perp \times \boldsymbol{t_4})\right]\big|_{\partial_{N_m}\Omega_h},$$

where

$$\boldsymbol{t_1} = \frac{\boldsymbol{r'}}{||\boldsymbol{r'}||}\left(||\boldsymbol{r'}|| - 1\right),$$

$$\boldsymbol{t_2} = \frac{2\boldsymbol{r'}\left(\boldsymbol{r'}\cdot\boldsymbol{r''}\right)^2}{||\boldsymbol{r'}||^6} - \left[\frac{\boldsymbol{r'}\left(\boldsymbol{r''}\cdot\boldsymbol{r''}\right) + \boldsymbol{r''}\left(\boldsymbol{r'}\cdot\boldsymbol{r''}\right)}{||\boldsymbol{r'}||^4}\right],$$

$$\boldsymbol{t_3} = \frac{\boldsymbol{r''}}{||\boldsymbol{r'}||^2} - \frac{\boldsymbol{r'}\left(\boldsymbol{r'}\cdot\boldsymbol{r''}\right)}{||\boldsymbol{r'}||^4},$$

$$\boldsymbol{t_4} = \frac{\boldsymbol{r'}}{||\boldsymbol{r'}||^2},$$

$$\boldsymbol{G_1} = \frac{\boldsymbol{I}}{||\boldsymbol{r'}||} - \frac{(\boldsymbol{r'}\otimes\boldsymbol{r'})}{||\boldsymbol{r'}||^3},$$

$$\boldsymbol{t_5} = \boldsymbol{G_1}\left[\!\left[\boldsymbol{g_1}\right]\!\right].$$

Due to the pronounced nonlinearities associated with fracture, an explicit time discretization is adopted for simplicity. In particular, Equation 3.36 is discretized in time using the second-order explicit Newmark scheme. To avoid the computational cost of solving a linear system for the accelerations, a specialized mass lumping technique is employed [**hughes2012finite**]. Since explicit time integration schemes are conditionally stable, the stable time step Δt_c can be determined based on the Courant–Friedrichs–Lewy (CFL) condition:

$$\Delta t_c = \frac{2}{\omega_{max}}, \tag{3.37}$$

where $\omega_{max} = \max_{i=1}^{N}(||\lambda_i||)$ is the maximum natural frequency of the system.
In the simulations, the stable time step Δt_c is used once at the beginning of the calculation and held constant throughout, i.e., $\Delta t = \Delta t_c$. The value of Δt_c would be determined by solving the following linearized eigenvalue problem:

$$\left(\boldsymbol{K}_{ab}^{\text{int}} + \boldsymbol{K}_{ab^{\pm}}^{\text{jump,DG}} - \lambda^2\, \boldsymbol{M}_{ab}^{\text{lump}}\right)\boldsymbol{\Phi} = \boldsymbol{0}, \tag{3.38}$$

where λ and $\boldsymbol{\Phi}$ denote the eigenvalue and eigenvector pair, respectively. Here, $\boldsymbol{M}_{ab}^{\text{lump}}$ is the lumped mass matrix, and $\boldsymbol{K}_{ab}^{\text{int}}$ and $\boldsymbol{K}_{ab^{\pm}}^{\text{jump,DG}}$ are the stiffness matrices.

3.6. Penalty method for rigid contact with truss lattices

Based on the formulation of contact as done by Wriggers [29] as described in Subsection 2.4.3 an implementation of the penalty method for rigid contact is described in this section. As shown in Equation 2.41 (Subsection 2.4.3) the contact force for a body and a rigid body can be expressed as:

$$F_c = \epsilon c(u), \quad \text{for } c(u) > 0, \tag{3.39}$$

where R_N is the contact force, ϵ is the penalty parameter, and $c(u)$ is the penetration. Since the contact force is calculated at each of the nodes nodes of the lattice can be indexed with i and then the expression for the contact force in each of the nodes can be expressed as:

$$F_{ci} = \epsilon c(u)_i, \quad \text{for } c(u)_i > 0. \tag{3.40}$$

The setup presented as presented in Subsection 2.4.3 can be modified to include a spherical rigid contact surface and a lattice structure as shown in Figure 3.6. For this setup Equation 3.40 can be used to account for the spherical 3 dimensional geometry of the rigid body by expressing it in vector form:

$$\boldsymbol{F_{ci}} = \epsilon \boldsymbol{c(u_i)}, \quad \text{for } ||\boldsymbol{d(u_i)}|| < R, \tag{3.41}$$

where R is the radius of the impactor and $\boldsymbol{d(u_i)}$ is a distance vector. The distance vector $\boldsymbol{d(u_i)}$ is defined as the difference between the center of the rigid body ($\boldsymbol{u_{impactor}}$) and the node of the lattice structure ($\boldsymbol{u_i}$):

$$\boldsymbol{d(u_i)} = \boldsymbol{u_i} - \boldsymbol{u_{impactor}}. \tag{3.42}$$

The value of the penetration $\boldsymbol{c(u_i)}$ can be found as:

$$\boldsymbol{c(u)_i} = \boldsymbol{d(u_i)} - \boldsymbol{R_i}, \tag{3.43}$$

where $\boldsymbol{R_i}$ is the radius vector that is a vector of length equal to the radius that is parallel to the distance vector $\boldsymbol{d(u_i)}$ and thus can be expressed as:

$$\boldsymbol{R_i} = R \cdot \frac{\boldsymbol{d(u_i)}}{||\boldsymbol{d(u_i)}||}. \tag{3.44}$$

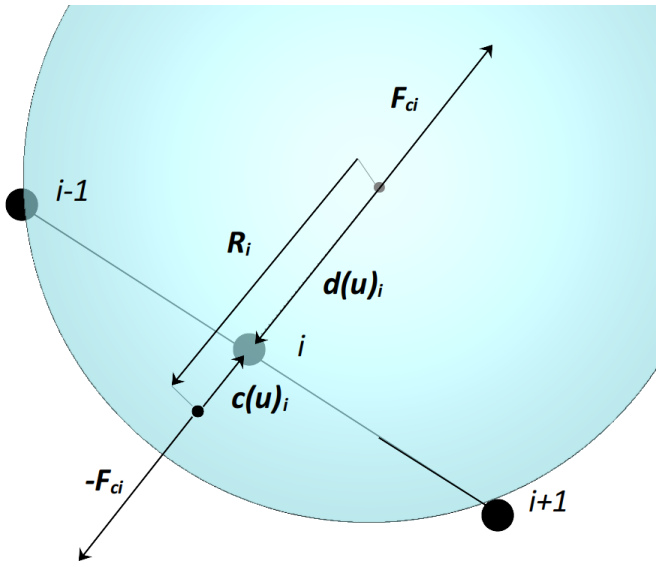

Figure 3.6: Implementation of the penalty contact method on a simple lattice.

Once the contact force of each node $-\boldsymbol{F_{ci}}$ has been calculated it can compiled and be added to the external force vector $\boldsymbol{f^{ext}}$ of the lattice structure. Similarly, to find the force exerted onto the rigid

impactor the contact force contributions of all of the nodes of the lattice structure are summed together and applied as an external force to the rigid body:

$$\boldsymbol{F}_c^{impactor} = \sum_{i=1}^{N} \boldsymbol{F}_{ci}. \tag{3.45}$$

3.7. Parallelization

In order to ensure that it is feasible to perform the computation on the lattice mesh consisting of about 65 thousand nodes the computation has to be parallelized. The parallelization is done by subdividing the lattice mesh into subdomains as has been illustrated in Figure 3.7. The partitions are performed by METIS [43] program that uses graph partitioning algorithms, such as, multilevel recursive-bisection, multilevel k-way, and multi-constraint partitioning schemes.

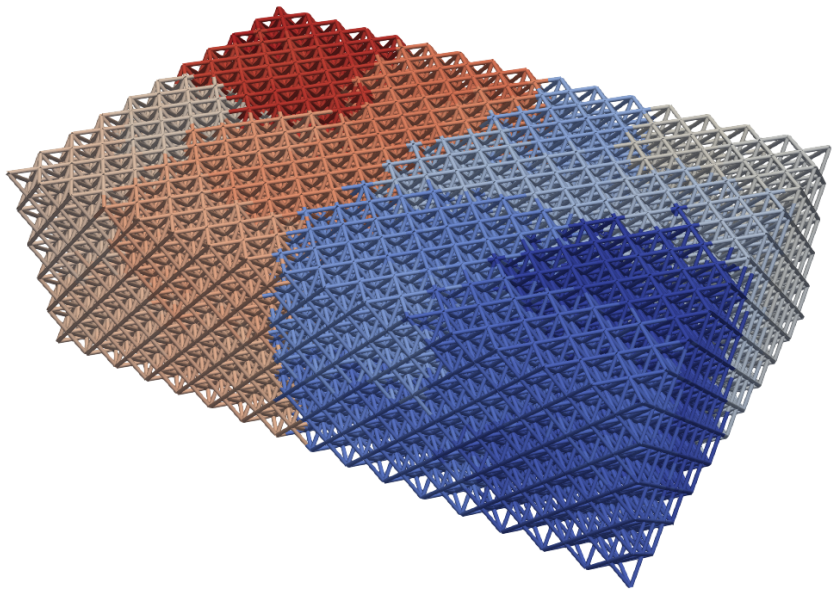

Figure 3.7: The division of the truss lattice into subdomains for parallelization.

The parallelized implementation of the code allows to distribute the computation among multiple processing nodes which in this case is done by using the Message Passing Interface (MPI). The computation follow a scheme where the relevant calculations including the linear matrix operations, cohesive forces and contact forces are performed in parallel for each of the mesh subdomains for every time step. To ensure that the results remain synchronized for all of the subdomains the results are communicated across the subdomain interfaces for the discontinuous Galerkin formulation. On the other hand, the contact formulation requires no additional implementation efforts for parallelization since the contact forces are calculated independently for each of the nodes of the lattice structure.

3.8. *Summit* framework

The work performed in this study was implemented within the *Summit* finite element framework, a high-performance computational platform originally developed in C++ at the Massachusetts Institute of Technology. It was subsequently extended by Dr. Bianca Giovanardi and her research group at TU Delft to support advanced simulations in computational mechanics. The modular architecture of *Summit* has enabled a wide range of applications, including the use of the discontinuous Galerkin method for modeling nonlinear solid mechanics [44], complex fluid–structure interactions [45], and scalable parallel

computation across distributed systems [46].

The versatility and extensibility of *Summit* stem from its object-oriented design in C++, which is particularly well-suited for large-scale scientific software development. Object-oriented programming (Object oriented programming (OOP)) promotes modularity through encapsulated classes and hierarchical inheritance, enabling structured code that is easier to maintain, extend, and debug across collaborative research teams. C++ further empowers *Summit* with fine-grained memory control, high execution speed, and compatibility with multithreading and GPU offloading—key requirements in computationally intensive finite element simulations. Its cross-platform portability also ensures that simulations developed on local machines can be efficiently deployed to HPC clusters or cloud-based environments with minimal modification.

Figure 3.8 provides a schematic of the framework within the context of this work. The work can be broken down into three main attributes: input, *Summit* and Output. The input contain information about the problem, such as the material properties and choice of material model or element type, the definition of the geometry as a mesh, system parameters including boundary conditions, time step size and others. The *Summit* framework includes the elements, which mathematically define the specific finite element type used; the system model, which defines the physical behavior of the system; the weak form, which implements the mechanics and constructs the variational formulation of the governing equations and the solver, which is responsible for the numerical solution strategy employed in the simulation. Similarly to any software project, *Summit* also requires other software to function which in the flowchart below is shown in the modules/libraries section. Finally, the output is the unprocessed data resulting from the execution of the application. The output can be further processed to obtain a visual representation of the simulation (in this project using *Paraview*) or other results that can be used to analyze the simulation.

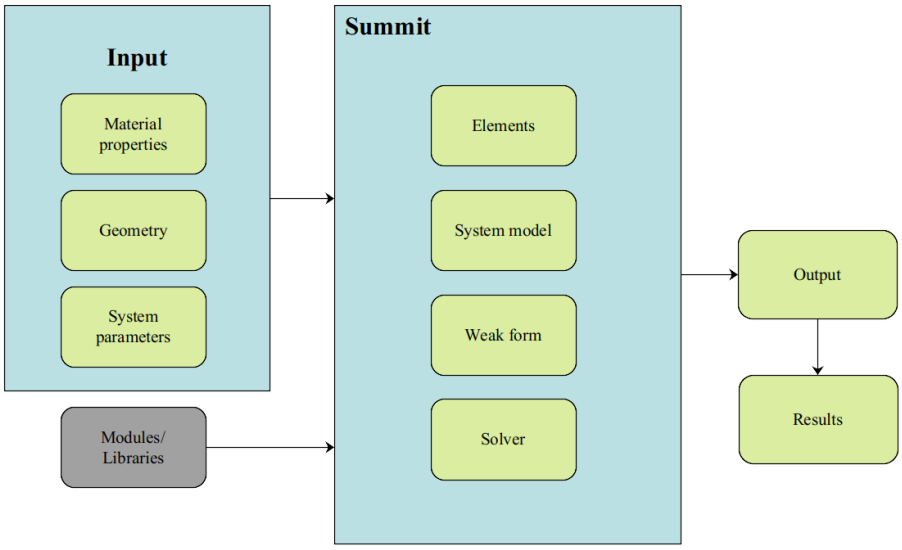

Figure 3.8: Overview of the *Summit* framework withing in the context of this work.

4

Results and Discussions

In this chapter the results of the simulations are presented and discussed. The chapter is divided into two main sections. The first section describes the simulation setup and the parameters used in the simulations. The second section presents visualization of the simulations including the various impact modes, discusses the impact of a rigid impactor and contains the results of the simulations including graphs containing information about the movement and energy of the impactor.

4.1. Simulation setup

In this section the parameters of the simulations are presented. This includes general information about the lattice and the simulation, as well as the Lattice types. In total 4 Lattice types were simulated with 2 different Lattice types. The properties of the lattice for each of the Lattice types are summarized in Table 4.1. For each of the Lattice types an rigid impactor with radius of $0.01m$ was used that impacted the lattice at velocities ranging from $50m/s$ to $350m/s$. Material properties of the lattice remained constant for all of the Lattice types while the contact penalty parameter had to be changed in some cases to accommodate the differing effective stiffness of the various lattices. The remaining simulation parameters are shown in Appendix A.

It should be noted that the relative densities of the lattices are much lower than those typically used in literature (e.g. in Portela and Butruille [1, 2, 7] the relative density of the lattices ranges from 14% to 33%). This discrepancy is due to the beam element used that requires relatively high aspect ratio of the beams.

	Lattice type 1	**Lattice type 2**	**Lattice type 3**	**Lattice type 4**
Lattice type	Octet	Octet	Octet	Bitruncated octahedron
Beam Radius	1.0e-4 m	0.5e-4 m	2.0e-4 m	1.0e-4 m
Relative density	0.1155%	0.0289%	0.4620%	0.0631%

Table 4.1: Lattice properties of the 4 Lattice types used in the simulation. The two properties that were changed were the Lattice type and strut radius. Additionally, relative density is calculated and provided in the table.

Figure 4.1 shows an example of an impactor during an impact with the octet lattice. These visualization are used to verify the simulation setup and to evaluate the results, i.e. to see whether the impactor penetrates the lattice or bounces back.

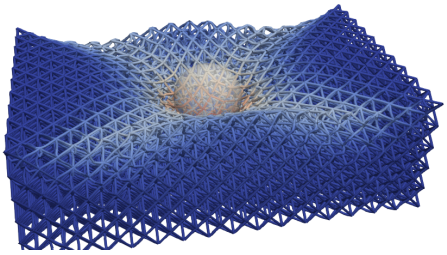

Figure 4.1: Visualized example of an impactor during an impact with octet lattice. The color of the lattice indicates the deformation of the lattice with red being the most deformed and blue being the least deformed.

4.2. Impact of a rigid impactor into a truss based lattice

In this section the results of simulating an impact of a truss based lattice are presented. The results consist of 2 parts: qualitative impact behavior and energy dissipation behavior. The qualitative impact behavior is presented in terms of movement or the kinematic behavior of the impactor. This is done such that the movement of the impactor can be compared to what is found in the literature and it can be determined under what conditions the impactor shows bounce-back, capture and penetration behavior. The energy dissipation behavior presents various energy dissipation properties of the impactor and thus the lattice. The energy dissipation is discussed with regards to the various impact velocities and Lattice types used.

4.2.1. Qualitative impact behavior

During literature review (Section 2.1) it was found that the impactor can exhibit three different behaviors when impacting a lattice structure: bounce-back, capture and penetration. This subsection aims to show whether this behavior can be captured in the simulations performed in this project.

The types of qualitative impact behavior of the impactor is visualized in Figure 4.3, Figure 4.4 and Figure 4.5. Additionally, Figure 4.2 shows the starting setup of the simulation.

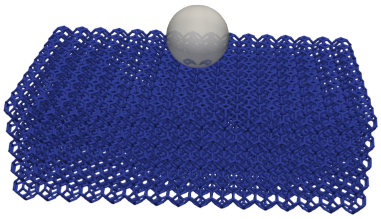

Figure 4.2: Starting setup for all of the Lattice types with the impactor right before contact with the lattice.

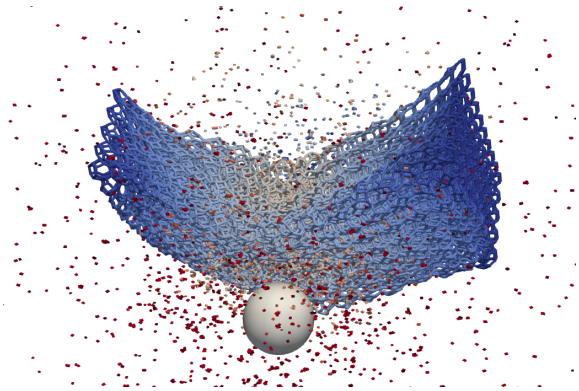

Figure 4.3: Visualized example of penetrating behavior. The figure shows a bitruncated octahedron lattice and impactor after 300 m/s impact. The lattice is heavily deformed and debris has been dispersed in the surrounding environment. The color of the lattice indicates the deformation of the lattice with red being the most deformed and blue being the least deformed.

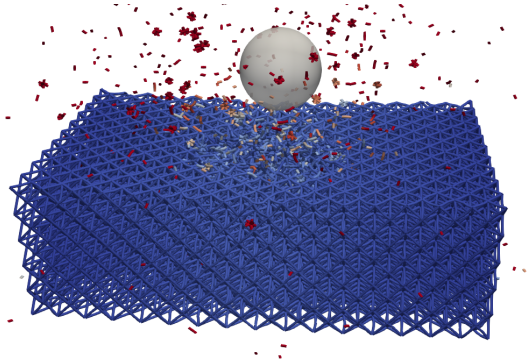

Figure 4.4: Visualized example of bounce-back behavior. The figure shows an octet lattice and impactor after 150 m/s impact. The lattice has localized damage and some debris has been dispersed in the surrounding environment. The color of the lattice indicates the deformation of the lattice with red being the most deformed and blue being the least deformed.

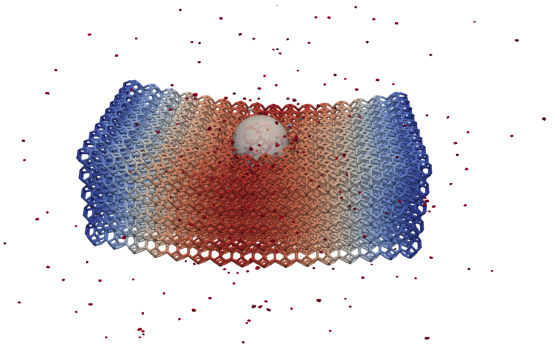

Figure 4.5: Visualized example of capture behavior. The figure shows an octet lattice and impactor after 100 m/s impact. The lattice has localized damage and some debris has been dispersed in the surrounding environment. The impactor velocity is almost zero and thus it can be considered captured by the lattice. The color of the lattice indicates the deformation of the lattice with red being the most deformed and blue being the least deformed.

Figure 4.6, Figure 4.7, Figure 4.8 and Figure 4.9 show the kinematic behavior of the impactor at 7 different velocities for Lattice type 1, Lattice type 2, Lattice type 3 and Lattice type 4, respectively. To generate the plots corresponding to a Lattice type all of the simulation parameters were kept constant except for the initial velocity of the impactor. The plots show the position and velocity of the impactor as a function of time for 7 velocities with each line representing a profile of a single initial velocity. All four figures contain 2 subplots with subplot **A** showing the position of the impactor and subplot **B** showing the velocity the impactor. The position plots start at a non-zero value that corresponds to the radius of the impactor. Both position and velocity are measured along z axis which is the axis along which the impactor is moving. The plots allow to illustrate key behavior of the impactor such as: bounce-back, which corresponds to positive slope of the position plot and negative velocity in the velocity plot; capture, which corresponds to a horizontal line of the position plot and zero velocity; and penetration, which corresponds to a negative slope of the position plot and positive velocity.

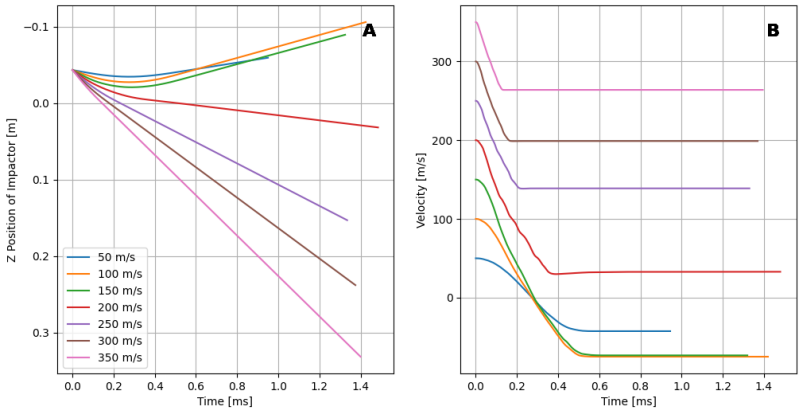

Figure 4.6: Kinematic behavior of the impactor as functions of time at 7 different initial velocities for Lattice type 1. Plot **A** includes impactor position along z axis which is the axis of impact. The position for all velocities starts at non-zero value since the position of the impactor at the start offset by the radius of the impactor such that the impactor is in contact with the outer surface of the lattice. The plots illustrate the fact that depending on the impact velocity the impactor can exhibit different behavior - bounce back for the 3 slower impactors (which is seen as the the plots having positive slope), substantial slow down for the $200m/s$ impactor and penetration for the remaining faster impactors. The velocity plots (plot **B**) show the value of velocity of the impactor along impact axis. The plot also demonstrates that the lower impact velocity impactors exhibit a bounce-back behavior that is illustrated as the velocity becoming negative.

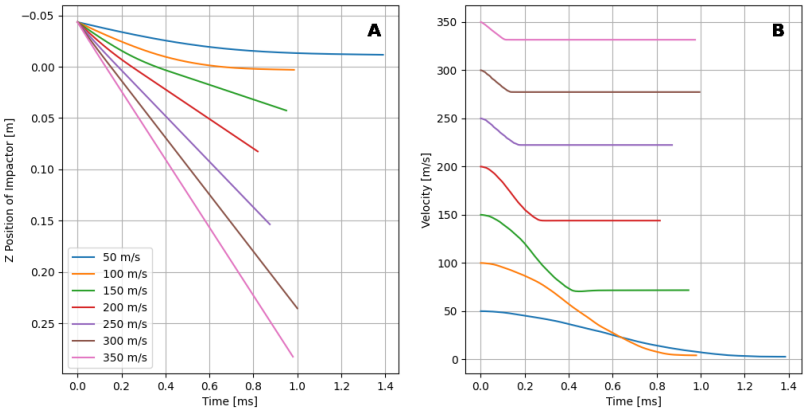

Figure 4.7: Kinematic behavior of the impactor as functions of time at 7 different initial velocities for Lattice type 2. Plot **A** includes impactor position along z axis which is the axis of impact. Plot **B** shows the velocity of the impactor along z axis. The position for all velocities starts at non-zero value since the position of the impactor at the start offset by the radius of the impactor such that the impactor is in contact with the outer surface of the lattice. The plots illustrate the fact that depending on the impact velocity the impactor can exhibit different behavior - impactor capture behavior for the two slowest impactors, penetration for the faster impactors however no bounce-back behavior is observed. Capture is shown as the position plot **A** being horizontal and the velocity plot **B** reaching zero.

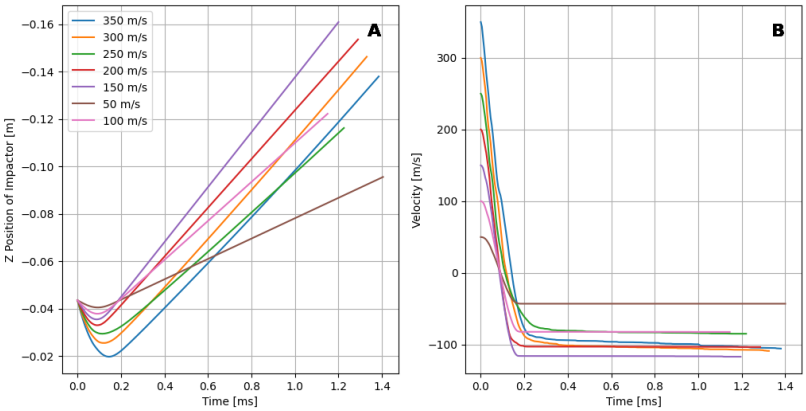

Figure 4.8: Kinematic behavior of the impactor as functions of time at 7 different initial velocities for Lattice type 3. Plot **A** includes impactor position along z axis which is the axis of impact. Plot **B** shows the velocity of the impactor along z axis. The position for all velocities starts at non-zero value since the position of the impactor at the start offset by the radius of the impactor such that the impactor is in contact with the outer surface of the lattice. This figure shows bounce-back of the impactor from the lattice which is seen as a minimum point in plot **A** and as negative values in plot **B**. No other impact modes could be identified for this setup, likely due to the increased thickness of the lattice.

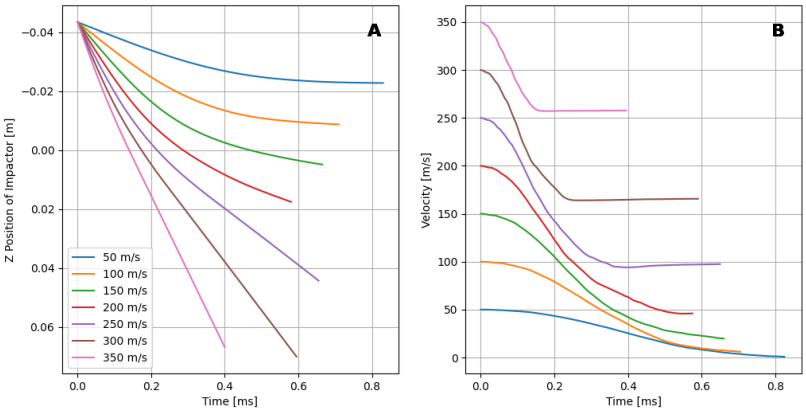

Figure 4.9: Kinematic behavior of the impactor as functions of time at 7 different initial velocities for Lattice type 3. Plot **A** includes impactor position along z axis which is the axis of impact. Plot **B** shows the velocity of the impactor along z axis. The position for all velocities starts at non-zero value since the position of the impactor at the start offset by the radius of the impactor such that the impactor is in contact with the outer surface of the lattice. The plots illustrate the fact that depending on the impact velocity the impactor can exhibit different behavior - impactor capture behavior for the slowest impactor, penetration for the faster impactors however no bounce-back behavior is observed. Capture is shown as the position plot **A** being horizontal and the velocity plot **B** reaching zero.

By comparing Figure 4.6, Figure 4.7, Figure 4.8 and Figure 4.9 to the experiments performed by Portela [1] as shown in Figure 2.2, it can be seen that the impactor exhibits [1] similar bounce-capture-penetrate behavior. While the scale and the setups are different the trend that impactor bounces back at lower velocities, is captured at higher velocities and then penetrates the metamaterial lattice at even higher velocities is present in the simulations. Admittedly, all 3 behaviors could not be identified in a single Lattice type due to the limited number of simulations used and limited number of simulation setup variables changed. But by examining the current results, it can be reasonably expected, that with sufficiently fine attempted impact velocity resolution for all Lattice types modelled here, impactor could be setup (with appropriate velocity, size and density), such that all 3 qualitative behaviors are present.

Additionally, a qualitative trend can be identified wherein increasing the radius of the struts in the lattice is similar to reducing the impact velocity, with regards to what impact modes are present. This is expected behaviour and further verifies the insights provided by these simulations. This trend can be identified in two ways. Firstly, by examining and comparing the kinematic behavior plots of the 3 Lattice types with octet lattice - larger struts result in more bounce-back behaviour and smaller struts result in more penetration. Secondly, by examining the initial to final velocity plot Figure 4.14. Here it can be seen that generally the thicker lattices approach the full diagonal line indicating perfectly elastic impact but the thinner lattices approach the dashed line indicating an impact were the lattice has reduced impact absorption capabilities. Similar findings are presented by Portela [1] - there it found that thinner struts lead to penetration and bounce-back but thicker struts lead to capture and bounce-back.

4.2.2. Energy dissipation behavior

Since energy dissipation is a key property of a structure under impact, this subsection focuses on the energy dissipation behavior of the impactor and the lattice. These results can be used to compare to the findings of other research work as discussed in literature review (Section 2.1).

Figure 4.10, Figure 4.11, Figure 4.12 and Figure 4.13 display the energy of the impactor as a function of time for each of the Lattice types. Evolution of impactor kinetic energy through time can be combined with measurements of other energy components, such as kinetic and potential energy of the lattice and energy dissipated by fracture to gain insight into the energy dissipation mechanisms of the lattice.

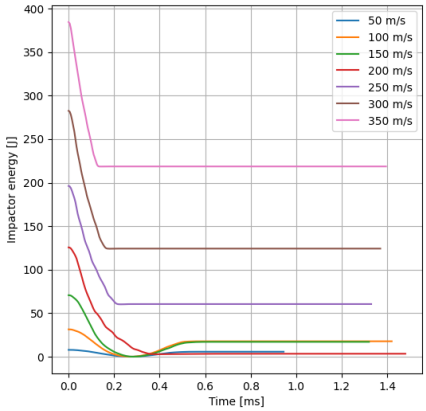

Figure 4.10: Energy of the impactor as a function of time at 7 different initial velocities for Lattice type 1. The plots illustrate the bounce-back behavior of the lattice at lower impact velocities as an increase in the energy value of the impactor after a dip in energy values. For higher velocities impactor regains no energy as the impact shows either penetration or capture.

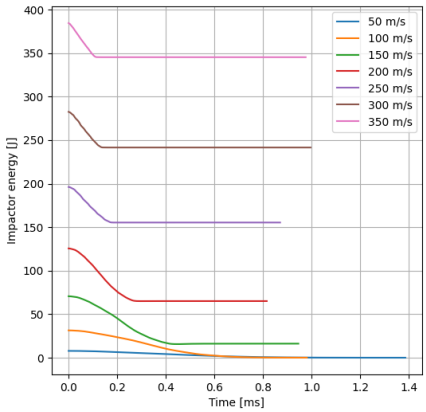

Figure 4.11: Energy of the impactor as a function of time at 7 different initial velocities for Lattice type 2. All of the impactor energy curves show a similar pattern of energy loss as the impactor penetrates the lattice. Furthermore, the 2 slowest impactors show a capture behavior of the impactor as the energy of the impactor as can be seen on the plots approaches zero.

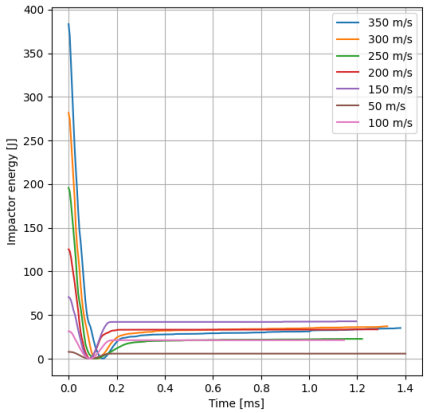

Figure 4.12: Energy of the impactor as a function of time at 7 different initial velocities for Lattice type 3. For this Lattice type all of the impacts show bounce-back behavior and the magnitude of energy loss is illustrated in this plot as the difference between starting energy and the energy at the end of the impact.

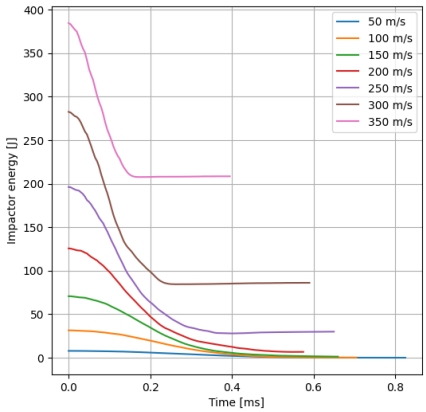

Figure 4.13: Energy of the impactor as a function of time at 7 different initial velocities for Lattice type 4. All of the impactor energy curves show a similar pattern of energy loss as the impactor penetrates the lattice.

Figure 4.14 shows the velocity of the impactor at the end of the impact as a function of the initial velocity. Furthermore, a diagonal line is displayed to show a perfectly elastic behavior of the impactor where the final velocity is equal to negative of the initial velocity and a dashed line is drawn to show impact during which the impactor maintains its velocity. The dispersal of the points shows the non-linear behavior of the impactor at lower velocities including a minimum point at initial velocity of $200 m/s$. For higher velocities the impactor exhibits a linear behavior with a slope of approximately equal to 1.

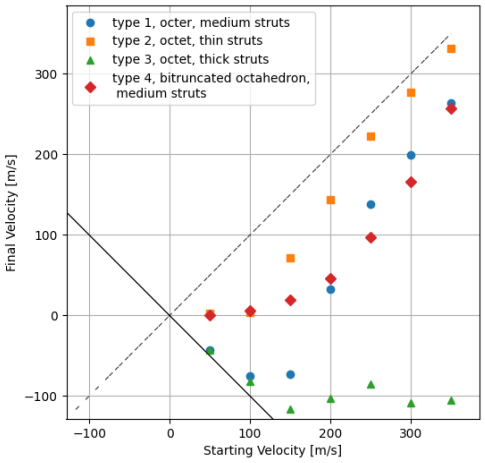

Figure 4.14: Comparison of final velocities of the impactor at 7 different velocities for the 4 lattice types. The plot shows the final velocity of the impactor as a function of initial velocity. A diagonal line shows perfectly elastic behavior with the final velocity being equal to the initial velocity and dashed line shows conditions when initial velocity is equal to final velocity. The four Lattice types show distinct behavior. At lower velocities the plots show show any trends less clearly for all of the Lattice types. As the velocities increase all of the plots show more linear trends with Lattice types 1, 2 and 4 approaching the dashed line for higher impact velocities. This effect can be described by the fact that the energy of the impactor increases with higher velocity at a much greater rate than the ability of the lattice to dissipate the energy. Lattice type 3 roughly follows the full diagonal line that describes elastic impact for lower velocities but for higher velocities the impactor bounces back at roughly the same velocity. Furthermore, it can be seen in the plot that Lattice type 2 is closer to the dashed line than Lattice types 1 and 3 thus indicating lower ability to absorb energy of Lattice type 2.

The velocity loss plot in Figure 4.14 shows that the impact might be approaching perfectly elastic behavior at lower velocities as all of the Lattice types show a curve at lower velocities that to varying extents approaches the diagonal line indicating perfectly elastic behavior. For increasing velocities most plots (all except Lattice type 3 which corresponds to the thickest struts) start to move towards the dashed line that indicates an impact where no energy is dissipated or transferred to the lattice and the impactor penetrates the lattice. This trend agrees well with the energy findings in Figure 4.15 subplot **A** where it can be the absolute energy loss of the impactor shows a plateau. Lattice type 3 shows distinct behavior where it does not approach the dashed line but instead shows constant bounce-back behavior at higher velocities. To find the cause of this effect it should be examined deeper by performing simulations with other impact velocities, impactor sizes and densities.

In Figure 4.15 two subplots are shown. In subplot **A** the absolute kinetic energy loss (difference between starting and final energy) of the impactor is presented as a function of initial velocity for both Lattice types. In subplot **B** the relative energy loss (energy loss relative to starting energy) of the impactor is shown as a function of initial velocity as a function of initial velocity. In subplot **C** the energy loss of the impactor normalized by the relative density of the lattice is shown. The plots show that the energy loss of the impactor increases with increasing initial velocity for lower velocities for all Lattice types. For higher velocities the absolute energy loss keeps increasing until it reaches a plateau at various points for types 1, 2 and 4. Lattice type 3 does not have this plateau but it is expected that it would probably appear at some higher velocity. Regarding relative energy loss as shown in subplot **B**, Lattice type 1 shows a maximum, Lattice types 2 and 4 show relative energy loss decreasing for higher impact velocities while Lattice type 3 shows increasing trend. This likely indicates that all Lattice types might have a maximum but at different velocities that were not examined in this simulation setup. This maximum corresponds to the impactor capture behavior. **C** shows the same trends as subplot **A** but normalized by the relative density of the lattice. This allows to compare the energy absorption properties of the different Lattice types for various velocities. It shows that there no clear trends visible.

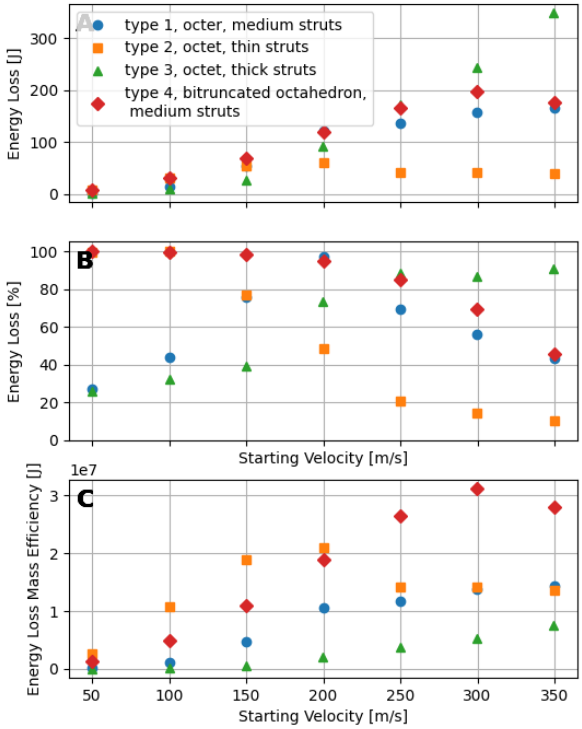

Figure 4.15: Comparison of energy loss of the impactor at 7 different velocities for various Lattice types. Plot **A** shows the energy loss of the impactor as a function of initial velocity. It can be seen that with increasing initial velocity the amount of energy loss is increased. Plot **B** shows the energy loss relative to initial energy as a function of initial velocity. This plot illustrates that there exists an energy loss maximum at medium velocities. Plot **C** shows the energy loss in Joules normalized by the relative densities of each of the lattices.

In Portela [1] (Figure 2.1) it was found that the energy absorbed by the lattice during impact scales roughly linearly with the initial velocity of the impactor. Similar behavior was present for lower impact velocities for all of the Lattice types as illustrated in subplot **A** of Figure 4.15. However, for higher velocities this behavior is no longer visible. Instead the energy absorption seems to plateau or even drop. This trend was not present in Portela [1] for metamaterials for the velocity range used there (about 200 m/s to 800 m/s) but it was present for other materials, such as aluminum. Admittedly, the simulation setup differs significantly regarding impact velocities, material scale, material properties and metamaterial relative densities, so it can be expected that the behavior will differ. It should also be noted that the lattice material with the thinnest struts (lattice type 2) show the plateau at the lowest impact velocities. This can be explained by the fact that the thinnest material has the least amount of material to dissipate the energy through elastic, fracture and kinetic means. Additionally, the thickest material (Lattice type 3) does not show this plateau at all and this can be explained by the reverse of the effect present in Lattice type 2. A possible explanation of the plateau behavior in subplot **A** of Figure 4.15 could be that the increased forces that are caused by the increased velocity are not scaling properly due to the nature of penalty contact model used in the simulations. This could cause the lattice to fail at lower velocities than it would otherwise and the earlier failure could limit the ability of the lattice to absorb energy from the impactor. Additionally, this possible effect of non-physically large force could be exaggerated by the incomplete fracture and beam model and the lack of plasticity.

Lastly with regards to subplot **A** of Figure 4.15, it is noteworthy that while Lattice types 1 and 4 have the same strut radiuses, they have substantially differing relative densities and yet they show similar behavior on the energy absorption plot. This could be explained by the different properties and failure modes of octet and bitruncated octahedron lattices.

Subplots **B** and **C** of Figure 4.15 show that energy loss relative to the starting energy of the impactor and relative to the density of the lattice, respectively. In subplot **B** a general trend can be seen where the Lattice types have a maximum that corresponds to the capture behavior of the impactor (or in the case of Lattice types 1 and 3 the closest point to capture). This plot allows to see at what starting velocities each of the Lattice types exhibit capture behavior which also correlates to the maximum energy loss and thus to the maximum energy absorption efficiency of the lattice. Subplot **C** contains a rescaled version of subplot **A** but due to the it is difficult to see any clear trends due to the different relative densities of the lattices.

In conclusion, 3 different behaviors of the impactor can be observed. The alignment with behavior seen in literature is not perfect but the general trends are similar for some parts of some of the Lattice types Importantly, the velocity range for each of the impact regimes depends on the lattice density and most likely also on other impact parameters such as impactor density and size which were not examined here.

5
Conclusion

5.1. Summary of findings

This thesis has presented a computational analysis of the fracture and impact dynamics of lattice-based metamaterials modeled using geometrically exact Kirchhoff-Love beams combined with a cohesive zone fracture model. The primary aim was to simulate the complex physical processes during dynamic loading events, particularly focusing on the energy dissipation mechanisms inherent in lattice metamaterials under impact conditions.

The computational model successfully reproduced key impact phenomena observed experimentally, including elastic and non-elastic collision behaviors, penetration, bounce-back, and particle capture, across various impact velocities. Generally, consistent with findings from Portela [1] and Butruille [2], including the effect of the radius of the lattice struts and impact velocity on the impact mode. A key difference from experimental results found in literature being the lack of linear scaling of energy absorption with increasing impact velocities. Using these results and analyzing what results align with the literature, it was possible to draw conclusions about the energy dissipation mechanisms in lattice metamaterials and are the key physical phenomena that need to be modelled to create a sufficiently advanced lattice metamaterial impact simulation.

5.2. Recommendations for future work

The results that were obtained nevertheless leave room for improvement and further research. There are aspects of the model, such as convergence analysis and energy components, that would have to be examined to gain a better answer to the research question that was set out. Furthermore, there are additional considerations that could be taken into account to expand the scope even further. The following list summarizes the most important aspects that could be improved or added to the model in future work:

- **Plasticity Modeling:** Incorporating a plasticity model could provide deeper insights into permanent deformation and energy absorption of the lattice, further enhancing the predictive capabilities of the simulation, especially at the lower velocities that are considered in this thesis.
- **Proper Scaling of the Model:** The work in this thesis unlike the research presented in the literature review is not performed in micro-scale. Additionally, the relative density of the lattice is also unrealistically small. Rescaling the model to a smaller scale and higher relative density would allow for a more accurate representation of the material properties and behavior of the lattice structures, particularly in terms of fracture mechanics and energy dissipation.
- **Beam Contact Refinement:** Integration of beam-to-beam contact formulation can significantly improve accuracy, particularly in capturing realistic interactions within dense lattice architectures where the contact stiffening effects are pronounced.

- **Convergence Analysis:** Conducting systematic convergence analyses regarding the number of elements, cohesive zone parameters, and contact penalty factors would improve numerical robustness and ensure computational accuracy and efficiency.
- **Energy Component Analysis:** A detailed decomposition of the energy components present in the simulation performed for this thesis, including kinetic, potential, and fracture energies, would refine our understanding of energy dissipation pathways and optimize lattice designs.
- **Boundary Condition Interference:** Addressing boundary interference effects by increasing the size of the model and ensuring that boundary conditions do not interfere with the wave propagation within the lattice structure would eliminate a possible source of error. This would be achieved by ensuring that the model is sufficiently large to accommodate wave propagation without interference from boundaries at the cost of increased computational resources.
- **Beam Formulation and Type:** Exploring alternative beam theories, like Timoshenko beams, may help overcome limitations associated with shear deformation effects, particularly relevant for shorter beams that are often present in lattice metamaterials. Overcoming the shortcomings of the current beam model would also aid with the unrealistic relative density of the lattice that is used in this thesis.
- **Strain Rate Effects:** Explicitly incorporating strain-rate dependency in material constitutive models would allow accurate prediction of lattice responses under realistic impact velocities, aligning computational results closely with experimental observations and allowing to explore higher impact velocities.

References

[1] C. M. Portela, B. W. Edwards, D. Veysset, Y. Sun, K. A. Nelson, D. M. Kochmann, and J. R. Greer. "Supersonic impact resilience of nanoarchitected carbon". *Nature Materials 2021 20:11* 20.11 (June 2021), pp. 1491–1497. DOI: 10.1038/s41563-021-01033-z.

[2] T. Butruille, J. C. Crone, and C. M. Portela. "Decoupling particle-impact dissipation mechanisms in 3D architected materials". *Proceedings of the National Academy of Sciences* 121.6 (2024), e2313962121. DOI: 10.1073/pnas.2313962121. eprint: https://www.pnas.org/doi/pdf/10.1073/pnas.2313962121.

[3] C. Fei Guo, T. Sun, F. Cao, Q. Liu, and Z. Ren. "Metallic nanostructures for light trapping in energy-harvesting devices". *Light: Science & Applications* 3 (2014). DOI: https://doi.org/10.1038/lsa.2014.42.

[4] Q. Lv, Z. Peng, H. Pei, X. Zhang, Y. Chen, H. Zhang, X. Zhu, and S. Wu. "3D Printing of Periodic Porous Metamaterials for Tunable Electromagnetic Shielding Across Broad Frequencies". *Nano-Micro Letters* (2024). DOI: https://doi.org/10.1007/s40820-024-01502-5.

[5] X. Zheng, H. Lee, T. H. Weisgraber, M. Shusteff, J. DeOtte, E. B. Duoss, J. D. Kuntz, M. M. Biener, Q. Ge, J. A. Jackson, S. O. Kucheyev, N. X. Fang, and C. M. Spadaccini. "Ultralight, ultrastiff mechanical metamaterials". *Science* 344.6190 (2014), pp. 1373–1377. DOI: 10.1126/science.1252291. eprint: https://www.science.org/doi/pdf/10.1126/science.1252291.

[6] "Approaching theoretical strength in glassy carbon nanolattices". *Nature Materials* ().

[7] C. M. Portela, A. Vidyasagar, S. Krödel, T. Weissenbach, D. W. Yee, J. R. Greer, and D. M. Kochmann. "Extreme mechanical resilience of self-assembled nanolabyrinthine materials". *Proceedings of the National Academy of Sciences* 117.11 (2020).

[8] C. Crook, J. Bauer, A. G. Izard, C. S. de Oliveira, J. M. de Souza e Silva, J. B. Berger, and L. Valdevit. "Plate-nanolattices at the theoretical limit of stiffness and strength". *Nature Communications* (2020). DOI: https://doi.org/10.1038/s41467-020-15434-2.

[9] A. Vyatskikh, S. Delalande, A. Kudo, X. Zhang, C. M. Portela, and J. R. Greer. "Additive manufacturing of 3D nano-architected metals". *Nature Communications* 9 (2018). DOI: https://doi.org/10.1038/s41467-018-03071-9.

[10] J. Harris, R. Winter, and G. McShane. "Impact response of additively manufactured metallic hybrid lattice materials". *International Journal of Impact Engineering* 104 (2017), pp. 177–191. DOI: https://doi.org/10.1016/j.ijimpeng.2017.02.007.

[11] T. Tancogne-Dejean, X. Li, M. Diamantopoulou, C. Roth, and D. Mohr. "High Strain Rate Response of Additively-Manufactured Plate-Lattices: Experiments and Modeling". *Journal of Dynamic Behavior of Materials* 5 (Aug. 2019). DOI: 10.1007/s40870-019-00219-6.

[12] E. S. D. Office. *ESA'S ANNUAL SPACE ENVIRONMENT REPORT*. Technical Report. ESA ESOC, 2024.

[13] R. Voillat, F. Gallien, A. Mortensen, and V. Gass. "Hypervelocity impact testing on stochastic and structured open porosity cast Al-Si cellular structures for space applications". *International Journal of Impact Engineering* 120 (Oct. 2018). DOI: 10.1016/j.ijimpeng.2018.05.002.

[14] J.-H. Lee, P. E. Loya, J. Lou, and E. L. Thomas. "Dynamic mechanical behavior of multilayer graphene via supersonic projectile penetration". *Science* 346.6213 (2014), pp. 1092–1096. DOI: 10.1126/science.1258544. eprint: https://www.science.org/doi/pdf/10.1126/science.1258544.

[15] J. Hyon, O. Lawal, O. Fried, R. Thevamaran, S. Yazdi, M. Zhou, D. Veysset, S. E. Kooi, Y. Jiao, M.-S. Hsiao, J. Streit, R. A. Vaia, and E. L. Thomas. "Extreme Energy Absorption in Glassy Polymer Thin Films by Supersonic Micro-projectile Impact". *Materials Today* 21.8 (2018), pp. 817–824. DOI: https://doi.org/10.1016/j.mattod.2018.07.014.

[16] V. Deshpande and N. Fleck. "High strain rate compressive behaviour of aluminium alloy foams". *International Journal of Impact Engineering* 24.3 (2000), pp. 277–298. DOI: https://doi.org/10.1016/S0734-743X(99)00153-0.

[17] H. A. Signetti S. "Transition regime between high-velocity and hypervelocity impact in metals – A review of the relevant phenomena for material modeling in ballistic impact studies". *International Journal of Impact Engineering* 167 (Sept. 2022). DOI: 10.1016/j.ijimpeng.2022.104213.

[18] A. Piekutowski. "Formation and description of debris clouds produced by hypervelocity impacts". *NASA Contractor Report* (Feb. 1996).

[19] J. Zukas. *Introduction to Hydrocodes*. Baltimore, USA: Computational Mechanics Association, 2004.

[20] C. E. Anderson and S. R. Bodner. "Ballistic impact: The status of analytical and numerical modeling". *International Journal of Impact Engineering* 7.1 (1988), pp. 9–35. DOI: https://doi.org/10.1016/0734-743X(88)90010-3.

[21] M. A. Crisfield and G. Jelenic. "Objectivity of strain measures in the geometrically exact three-dimensional beam theory and its finite-element implementation". *Proceedings of the Royal Society A: Mathematical, Physical and Engineering Sciences* 455 (1983 1999), pp. 1125–1147. DOI: 10.1098/rspa.1999.0352.

[22] C. Meier, A. Popp, and W. Wall. "Geometrically exact finite element formulations for slender beams: Kirchhoff-Love theory versus Simo-Reissner theory". *Archives of Computational Methods in Engineering* 26 (2019), pp. 163–243. DOI: 10.1007/s11831-017-9232-5.

[23] M. Elices, G. Guinea, J. Gómez, and J. Planas. "The cohesive zone model: advantages, limitations and challenges". *Engineering Fracture Mechanics* 69.2 (2002), pp. 137–163. DOI: https://doi.org/10.1016/S0013-7944(01)00083-2.

[24] B. L. Talamini and R. Radovitzky. "A parallel discontinuous Galerkin/cohesive-zone computational framework for the simulation of fracture in shear-flexible shells". *Computer Methods in Applied Mechanics and Engineering* 317 (2017), pp. 480–506.

[25] P. Zavattieri. "Modeling of crack propagation in thin-walled structures using a cohesive model for shell elements". 73 (2006), pp. 948–958. DOI: 10.1115/1.2173286.

[26] D. A. Di Pietro and A. Ern. *Mathematical aspects of discontinuous Galerkin methods*. eng. 1st ed. 2012. Mathematiques & applications, 69. Springer, 2012.

[27] L. R. Scott. *Numerical Analysis*. Princeton, New Jersey: Princeton University Press, 2011.

[28] B. Gustafsson. *High Order Difference Methods for Time Dependent PDE*. Vol. 38. Jan. 2008. DOI: 10.1007/978-3-540-74993-6.

[29] P. Wriggers. *Computational Contact Mechanics*. Berlin: Springer, 2006.

[30] A. Signorini. *Sopra alcune questioni di statica dei sistemi continui*. 1933.

[31] A. Signorini. "Questioni di elasticita' non linearizzata (signorini)". 1960.

[32] N.J. Carpenter, R.L. Taylor, and M.G. Katona. "Lagrange constraints for transient finite-element surface-contact". *International Journal for Numerical Methods in Engineering* 32 (1991), pp. 103–128.

[33] F. Cirak and M. West. "Decomposition contact response (DCR) for explicit finite element dynamics". *International Journal for Numerical Methods in Engineering* 64 (2005), pp. 1078–1110. DOI: 10.1002/nme.1400.

[34] C. Meier, A. Popp, and W. Wall. "A finite element approach for the line-to-line contact interaction of thin beams with arbitrary orientation". 308 (2016), pp. 377–413. DOI: 10.1016/j.cma.2016.05.012.

[35] S. K. Kota, S. Kumar, and B. Giovanardi. "A discontinuous Galerkin / cohesive zone model approach for the computational modeling of fracture in geometrically exact slender beams". *Computational Mechanics* (Dec. 2024). DOI: 10.1007/s00466-024-02521-0.

[36] J. Simo. "A finite strain beam formulation. The three-dimensional dynamic problem. Part I". 49.1 (1985), pp. 55–70. DOI: https:/s/doi.org/10.1016/0045-7825(85)90050-7.

[37] C. Meier, A. Popp, and W. A. Wall. "An objective 3D large deformation finite element formulation for geometrically exact curved Kirchhoff rods". *Computer Methods in Applied Mechanics and Engineering* 278 (2014), pp. 445–478.

[38] C. Meier, A. Popp, and W. A. Wall. "A locking-free finite element formulation and reduced models for geometrically exact Kirchhoff rods". *Computer Methods in Applied Mechanics and Engineering* 290 (2015), pp. 314–341. DOI: 10.1016/j.cma.2015.02.029.

[39] R. A. Schapery. "A theory of viscoelastic crack growth: revisited". *International Journal of Fracture* (2022).

[40] G. Camacho and M. Ortiz. "Computational modeling of impact damage in brittle materials". *International Journal of Solids and Structures* 33.20–22 (1996), pp. 2899–2983. DOI: 10.1016/0020-7683(95)00255-3.

[41] L. Noels and R. Radovitzky. "A general discontinuous Galerkin method for finite hyperelasticity. Formulation and numerical applications". *International Journal for Numerical Methods in Engineering* 68.1 (2006), pp. 64–97. DOI: 10.1002/nme.1699.

[42] G. Becker and L. Noels. "A fracture framework for Euler–Bernoulli beams based on a full discontinuous Galerkin formulation/extrinsic cohesive law combination". 85 (2011), pp. 1227–1251. DOI: 10.1002/nme.3008.

[43] G. Karypis and V. Kumar. *MeTis: Unstructured Graph Partitioning and Sparse Matrix Ordering System, Version 4.0*. http://www.cs.umn.edu/~metis. University of Minnesota, Minneapolis, MN, 2009.

[44] L. Noels and R. Radovitzky. "Alternative approaches for the derivation of discontinuous Galerkin methods for nonlinear mechanics". 74 (2007), pp. 1031–1045. DOI: 10.1115/1.2712228.

[45] A. Koshakji, G. Chomette, J. Turner, J. Jablonski, A. Haynes, D. Carlucci, B. Giovanardi, and R. Radovitzky. "A robust computational framework for simulating the dynamics of large assemblies of highly-flexible fibers immersed in viscous flow" (*submitted*).

[46] B. Giovanardi, S. Serebrinsky, and R. Radovitzky. "A fully-coupled computational framework for large-scale simulation of fluid-driven fracture propagation on parallel computers" (2020).

A

Appendix A

A.1. Information about the setup of the impact simulations

		Value	Unit
Impactor	Impactor Radius	$10e-3$	m
	Impactor Density	$1.5e3$	kg/m^3
General setup	Time Step	$1.0e-9$	s
	Contact Penalty Parameter	10.0 and 100.0	N/m
	Discontinous Galerkin Parameter	10.0	–
Lattice	Lattice Size	$53.6 \times 33.5 \times 43.5$	mm
	Material Density	$1.5e3$	kg/m^3
	Young's Modulus	$22.5e9$	Pa
	Failure Strenght	$.5e9$	Pa
	Fracture Energy	45.0	Nm^{-1}
	Mix Parameter α	1.0	–

Table A.1: Parameters describing the setup of the impact simulations. Contact penalty parameter was 10 for lattice types 1, 2 and 4 but it was increased to 100 for lattice type 3 due to its substantial higher stiffness.